Theses and Dissertations

2007

Static and seismic analysis of a single-tower cable-stayed bridge with concrete box girder

Boer Li
Lehigh University

Follow this and additional works at: http://preserve.lehigh.edu/etd

Li, Boer

Static and Seismic Analysis of a Single-Tower Cable-Stayed Bridge with Concrete Box…

September 2007

STATIC AND SEISMIC ANALYSIS OF A SINGLE-TOWER CABLE-STAYED BRIDGE WITH CONCRETE BOX GIRDER

by

Boer Li

A Thesis

Presented to the Graduate and Research Committee

of Lehigh University

in Candidacy for the Degree of

Master of Science

in

Department of Civil and Environmental Engineering

Lehigh University

August 2007

This thesis is accepted and approved in partial fulfillment of the requirements for the Master of Science.

08/06/2007

Date

_____

Dr. Yunfeng Zhang, Thesis Advisor

_____

Dr. Stephen P. Pessiki, Chairperson of Department

ACKNOWLEDGEMENTS

TABLE OF CONTENTS

LIST OF TABLES

LIST OF FIGURES

ABSTRACT

This thesis deals with the static and seismic response analysis of a prestressed concrete single tower cable-stayed bridge - the Zhao-Bao-Shan (ZBS) Bridge located in Ningbo, China. The ZBS Bridge had a severe engineering accident on September 24, 1998 and after retrofit measures it was opened to traffic on June 8, 2001. In order to perform the analysis of the retrofitted ZBS Bridge, two three-dimensional finite element models are established using *SAP2000*. Both finite element models were calibrated with ambient vibration test data.

In the static analysis, various thermal differential loading cases were considered in this study. The finite element model for static analysis employs the use of shell element to model the concrete bridge deck while frame element were used for modeling the structural members of the ZBS bridge. The analysis results were found to be in good agreement with experimental survey data in terms of deck displacement, tower displacement, and deck deformation and at selected locations.

Six real earthquake ground motion records were selected and scaled to match the maximum considered earthquake in the bridge site, where the design seismic intensity level was raised by one degree in 2002. Nonlinear time history analysis was carried out to study the seismic response behavior of the ZBS Bridge. A spine-model was used for bridge deck, which is much more computationally efficient than the shell

1

element model. It is found that the main structural elements of the ZBS Bridge are still within its elastic range while potential deseating problem for bridge deck might occur under the selected earthquake ground motions.

Chapter 1

Introduction

In this chapter, an overview of the history and development of cable-stayed bridges in the world as well as in the USA is first given with the intent to offer the background information for cable-stayed bridges. The research motivation and scope of this thesis on modeling and analysis of the Zhao-Bao-Shan Bridge, which is a prestressed concrete cable-stayed bridge located on the east coast of China, are presented next.

1.1 Overview of Cable-stayed Bridge

1.1.1 Conceptual Description of Cable-Stayed Bridge

Cable-stayed bridges have become one of the most widely used bridge forms in the past three decades. Modern cable-stayed bridges present a three-dimensional structural system that consists of girders, deck and supporting members such that towers in compression and stay cables in tension. Schematics of a typical cable-stayed bridge as well as its main structural components are shown in Figure 1.1. As shown in the figure, a typical cable-stayed bridge is a continuous girder with one or more towers erected above piers in the middle of the span. From these towers, cables stretch down diagonally (usually to both sides) and support the girder. Because the only part of the structure that extends above the road is the towers and cables, cable stayed bridges have a simple and elegant look.

1.1.2 Types of Cable-Stayed Bridge

Cable-stayed bridges can be distinguished by the number of spans, number of towers, girder type, number of cables, etc. There are many variations in the number and type of towers, as well as the number and arrangement of cables. Therefore, cable-stayed bridges can also be categorized according to the construction material used for major structural components, configurations of stay cables and tower. For example, different types of construction materials used for the main components like girders in cable-stayed bridges: steel, concrete, and hybrid cable-stayed bridge.

According to the various longitudinal cable arrangements, cable-stayed bridges could be divided into the following four basic systems shown in Figure 1.2. With respect to the positions of cable planes in space, there are four systems, as shown in Figure 1.3, developed from two basic arrangements of cables: two-plane systems and single-plane systems. In Figure 1.3, the space positions of cables are: (a) Two vertical planes system, (b) Two inclined planes system, (c) Single plane system, (d) Asymmetrical plane system.

Cable stayed bridges can also be classified according to various bridge towers types: (a) Trapezoidal portal frames, (b) Twin towers, (c) A-frames and (d) Single towers. Figure 1.4 shows some types of bridge towers shapes.

1.1.3 Historical Development of Cable-Stayed Bridge

The idea of using cables to support bridge spans is by no means new, and the basic form and concept of cable-stayed bridges have been recorded for centuries. In 1617, Faustus Verantius designed a bridge system having a timber deck supported by

4

inclined eyebars. In 1823, the famous French engineer Navier developed bridge systems stiffened by inclined chains.

The other type of stay arrangement, with parallel stays, was suggested by Hatley dating back to 1840. In 1868, the Franz Joseph Bridge over the Moldau River at Prague, Czech was built, using a new form of suspension introduced in the bridge.

Although cable-stayed bridges have been around for the last couple of centuries, they have become more prevalent in the last 50 years. Over the past decades, rapid development has been made on modern cable-stayed bridges, with application of high-strength materials and new methods of construction, development of electronic computers and progress in structural analysis.

The first modern cable-stayed bridge was the Strömsund Bridge designed by Franz Dischinger. The Strömsund Bridge, built in 1955 in Sweden, is a reinforced concrete bridge with a main span of 182.6 m. The Strömsund Bridge consists of two portal towers and two vertical planes of double radial stays as shown in Figure 1.5.

The Ganter Bridge crossing an Alpine valley is located near the Simplon Pass in Switzerland, as shown in Figure 1.6. Built in 1980, the Ganter Bridge is an interesting example of cable-stayed bridge, though the cables are inside a thin concrete shell. The overall layout of the bridge is S-shaped in plan, the 174 m main span is straight, but the side spans, including the back-stay cables, have 200-m radius curves. The taller pier is 50 m high.

Cable-stayed bridges are very price competitive in the 150 - 600 m span lengths range. Modern cable-stayed bridges, with increasing main span length and more shallow and slender girders, are adding more challenges to the structural design and

analysis for bridge engineers. Table 1.1 provides a list of cable-stayed bridges with the longest main span throughout the world.

The Tatara Bridge is the world's longest cable-stayed bridge as of Year 2006, as shown in Figure 1.7. The Tatara Bridge was opened to traffic in 1999, connecting the islands of Honshu and Shikoku, across the Seto Inland Sea in Japan. It is a steel-girder cable-stayed bridge. The bridge measures 1480 m in total length and has an 890-m long main span. The cables of the bridge are placed to make a fan shape and the steel towers of the bridge are 220 meters high and shaped like an inverted Y. The main towers have a cross-shaped section with corners cut for enhanced wind stability and more attractive architectural appearance.

Sutong Bridge is located at lower Yangtze River linking Nantong City and Suzhou City in China. This steel-girder cable-stayed bridge is still under construction presently and is scheduled to open to traffic in 2008. After completion, the bridge's main span, which is 1088-m long, will exceed that of the Tatara Bridge by 198 meters. It is anticipated that the Sutong Bridge will keep the record of the world's longest stayed-cable bridge for a considerable period of time. The Sutong Bridge is comprised of twin A-shape towers, stay cables in semi-fan arrangement, and a steel deck, as shown in Figure 1.8.

In the United States, there has been a substantial increase in the number and the rate of construction of cable-stayed bridge in the past two decades. Table 1.2 lists the cable-stayed bridges with ten longest main span lengths in the United States. The oldest cable-stayed bridge in the United States is the Sitka Harbor Bridge built in 1970 near Juneau, Alaska. From 1996 to 2005, 17 cable-stayed bridges were built in

6

the United States. Figure 1.9 shows the number of cable-stayed bridges built in the United States from 1955 to 2005 in 10-year increments (Tabatabai 2005).

The Arthur Ravenel Jr. Bridge crossing the Cooper River, shown in Figure 1.10, is presently the longest cable-stayed bridge in the United States, with a 471-m long main span. It is also the longest bridge of its kind in the North America. The Arthur Ravenel Jr. Bridge has a cable-stayed design with semi fan cable arrangement and two diamond-shaped towers, each with a height of 175 m. The span was designed to endure wind gusts in excess of 300 mph (133 m/s), far stronger than those of the state's worst hurricane, Hugo (1989) and withstand a magnitude 7.4 earthquake on the Richter scale without total failure.

Another interesting example of cable-stayed bridge is the Ruck-A-Chucky Bridge as shown in Figure 1.11. This bridge is considered to be *the most famous bridge never built*. The would-be bridge location is ten miles upstream of the Auburn Dam in California. The bridge design has a U-shaped curved flat deck, supported by numerous cables anchored on the sloping hillsides on each side of the gorge. There are no towers and no supporting piers below the roadway. The bridge is designed to consist of two components: the cable stays acting in tension and the curved girder carrying the traffic and absorbing the axial compression produced by the cables. The conception and design of this bridge represents an achievement in modern bridge engineering whereby technology in its many respects is rationally and inter-disciplinarily applied to transform an environmental obstacle into an asset, thus arriving at an economical as well as an aesthetic solution.

1.1.4 Advantages of Cable-Stayed Bridge

The rapid development of cable-stayed bridge can be partially attributed to its many outstanding characteristics and advantages. Cable-stayed bridge designs are used for intermediate-length spans and fill the gap that exists between the girder type and suspension type bridges. Compared with suspension bridge, cable-stayed bridge has the advantages of ease of construction, lower cost since anchorages are not required and small size of substructures; furthermore, there are no massive cables, as with suspension bridges, which making cable repair or replacement much easier in cable-stayed bridges. The general trend suggests that cable-stayed bridges with longer span length are becoming possible and economically more advantageous than suspension bridges.

1.1.5. Seismic Performance of Cable-Stayed Bridge

Earthquakes can have a very serious effect on a bridge. It can cause damage to structural elements, cause vibrations through the bridge, or even lead to a bridge collapse. Understanding the seismic response behavior of cable-stayed bridges is thus important to ensure structural safety and improve future design. Most cable-stayed bridges have a number of long-period modes due to the flexibility of their cable-superstructure system. However, in a seismic environment, since the largest earthquake spectral accelerations typically occur at relatively short periods, cable-stayed bridges with fundamental periods starting from 2.0 seconds tend to have a degree of natural seismic isolation. Thus, a rather favorable combination of structural dynamics and ground motion characteristics often exists for these types of bridges

8

(Wesolowsky and Wilson 2003). In the United States, two long-span cable-stayed bridges – the Bill Emersion Bridge in Missouri and the Arthur Ravenel Jr. Bridge in South Carolina are located in seismic active region. The Bill Emerson Bridge, a new Mississippi River crossing in service since December 2003, is located approximately 80 km due north of New Madrid, Missouri. The New Madrid area, where the great earthquakes of 1811 and 1812 occurred, is an active seismic region requiring earthquake hazard mitigation programs. Design of the bridge accounted for the possibility of a strong earthquake (magnitude 7.5 or greater) during the design life of the bridge, and as a result was based on design response spectrum anchored to a zero-period acceleration (ZPA) of 0.36 g with a 10% probability of being exceeded in 250 years (Woodward-Clyde 1994). A state-of-the-art seismic monitoring system with 84 accelerometers was installed to this 1,206-m-long (3,956 ft) Bill Emerson Memorial Bridge in 2003 (Celebi 2006).

1.2 Research Motivation

This research is focused on modeling and analysis of a single-tower prestressed concrete cable-stayed bridge in China – the Zhao-Bao-Shan (ZBS) Bridge under static (gravity and thermal differentials) and earthquake loading. The ZBS Bridge is selected for this study because of the following reasons: (i) The ZBS Bridge has a very unique configuration – single-tower with asymmetric main and side spans, which warrants a detailed study of its structural behavior under various loading conditions such as thermal differential and earthquakes; Although cable-stayed bridge has become more and more popular in the US, thus far there is no bridge of this kind

9

in the Unite States. The current analysis will provide valuable information on the structural behavior of the ZBS Bridge, and also help with the future application of this kind of cable-stayed bridges in the Unite States. (ii) The ZBS Bridge had a severe engineering accident during the construction (see Section 2.8 for details): concrete crushed at the lower flange of its prestressed reinforced concrete (RC) bridge box girder; after the accident and subsequent retrofit, structural properties of the bridge are supposedly different from the original design. Modeling of the bridge after retrofit is necessary to reflect the true behaviors of the bridge at present and predict its behavior under future loading such as heavy trucks and earthquakes. (iii) Last but not least, the region - Ningbo City in China, where the ZBS Bridge is located, has moderate earthquake activity. According to the Chinese seismic design code, the peak ground acceleration specified for this region classified as a Degree VII for seismic intensity level is equal to 2.25 m/sec^2. It is worth noting that in Year 2002, the seismic design intensity level in the local area of the ZBS bridge site was adjusted from Degree VI to VII. Since its construction was completed in 2001, the ZBS Bridge was thus designed for a seismic intensity level lower than that specified in the current seismic design code. In order to assure the safety of ZBS bridge under earthquakes loading, nonlinear time history analysis is thus necessary to provide an important basis for the estimated seismic response of the ZBS bridge, especially after the engineering accident in 1998 and subsequent retrofit actions taken on the bridge.

1.3 Scope of Thesis

1.3.1 Research Scope

This thesis presents the results of modeling and analysis of a single-towered RC cable-stayed bridge – the ZBS Bridge located on the east coast of China. Two versions of three-dimensional finite element models were established for the ZBS Bridge using the *SAP2000* software. The first one is a sophisticated finite element model based on the use of shell elements for the concrete bridge box girder and was used for static analysis of the ZBS bridge. The other one is based on beam elements and was used for nonlinear time history analysis of the ZBS Bridge under earthquakes. Both static analysis and dynamic analysis of the ZBS Bridge were performed in this study. Modeling details as well as the results from the static analysis and dynamic analysis are discussed in this thesis.

1.3.2 Organization of Thesis

There are six chapters in this thesis. Chapter 1 provides an introduction to the history and development of cable-stayed bridges as well as the research motivation and scope of this thesis. Chapter 2 gives a description of the ZBS Bridge. In Chapter 3 both the modeling details as well as the static analysis results for the ZBS Bridge are discussed. Chapter 4 presents the finite element model for dynamic analysis of the ZBS Bridge. Chapter 5 discusses the results from nonlinear time history analysis of the ZBS Bridge under earthquakes. Lastly, Chapter 6 provides a summary and suggests possible work for future research.

Table 1.1 Ten longest cable-stayed bridges in the world

No.	Bridge name	Main span (m)	Location	Country	Year
1	Sutong	1088	Suzhou-Nantong	China	2009
2	Stonecutters	1018	Hong Kong	China	2008
3	Tatara	890	Hiroshima	Japan	1999
4	Pont de Normandie	856	Le Havre	France	1995
5	Incheon-2	800	Incheon-Songdo	South Korea	2009
6	Nanjing-3	648	Nanjing	China	2005
7	Nanjing-2	628	Nanjing	China	2001
8	Jintang	620	Zhoushan Island	China	2008
9	Baishazhou	618	Wuhan	China	2000
10	Qingzhou	605	Fuzhou	China	2003
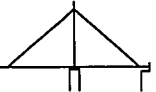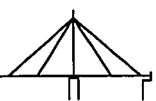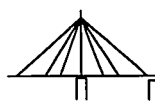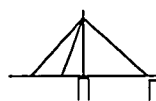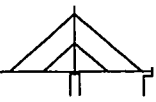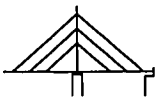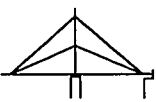
Table 1.2 Ten longest cable-stayed bridges in the United States

No.	Bridge name	Main span (m)	Location	Year[*]
1	The Arthur Ravenel Jr. Bridge	472	South Carolina	2005
2	Greenvill Bridge, US 82 over Mississippi	420	Mississippi	2005
3	Dame Point Bridge	397	Florida	1989
4	Fred Hartman/Houston Ship Channel	381	Texas	1995
5	Sidney Lanier Bridge, Brunswick	381	Georgia	2003
6	Hale Boggs/Luling Bridge	373	Louisiana	1984
7	Sunshine Skyway Bridge	366	Florida	1987
8	William Natcher/Owensboro Bridge	366	Kentucky	2002
9	Bill Emerson/Cape Girardeau Bridge	351	Missouri	2003
10	Talmadge Memorial Bridge, Savannah	336	Georgia	1991

* Year bridge construction completed
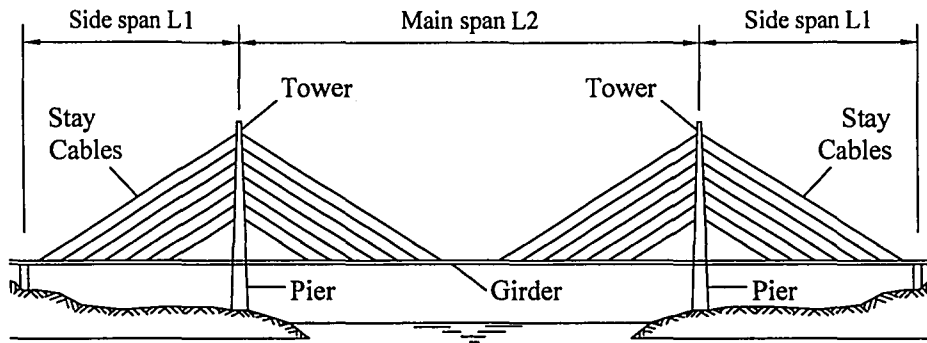
Figure 1.1 Schematic of cable-stayed bridge

STAY SYSTEM		SINGLE	DOUBLE	TRIPLE	MUTIPLE	VARIABLE
		1	2	3	4	5
1	BUNDLE OR CONVERGING OR RADIAL					
2	HARP OR PARALLEL					
3	FAN					
4	STAR					

Figure 1.2 Longitudinal layout of stay cables (Troitsky 1988)

13
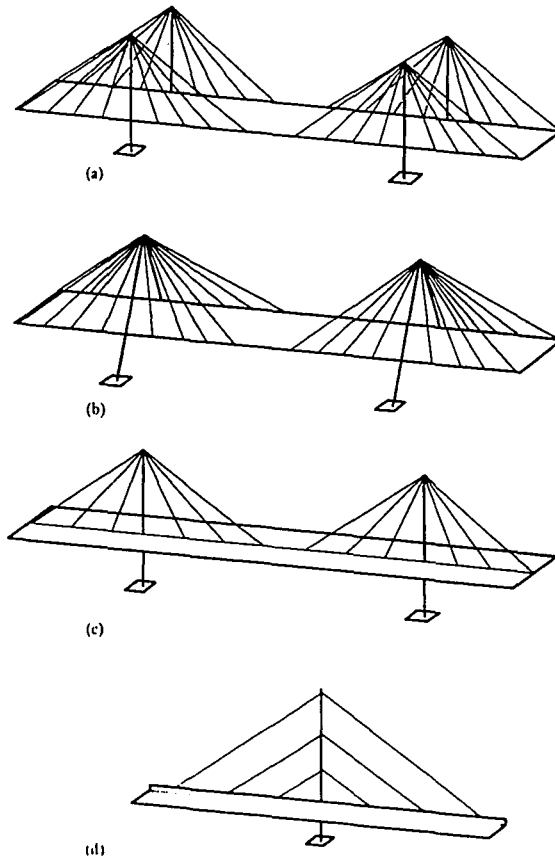
Figure 1.3 Transverse layout of stay cables (Troitsky 1988)
(a) Two vertical planes system   (b) Two inclined planed system
(c) Single plane system   (d) Asymmetrical planed system
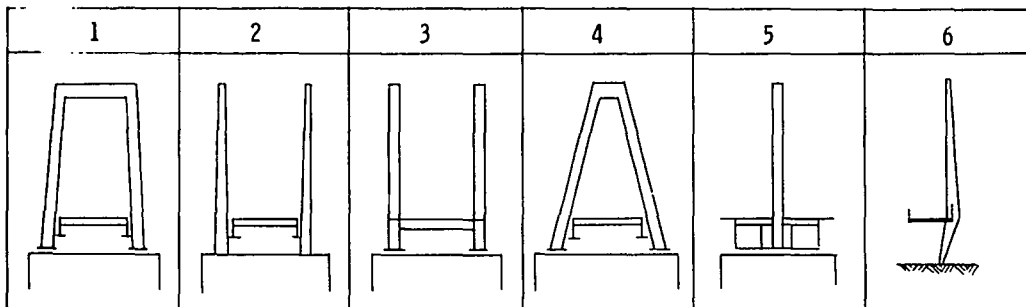
Figure 1.4 Transverse layout of tower (Troitsky 1988)
(1) Portal frame tower   (2) Twin monolithic tower   (3) Twin frame tower
(4) A-frame tower   (5) Single tower   (6) Side tower
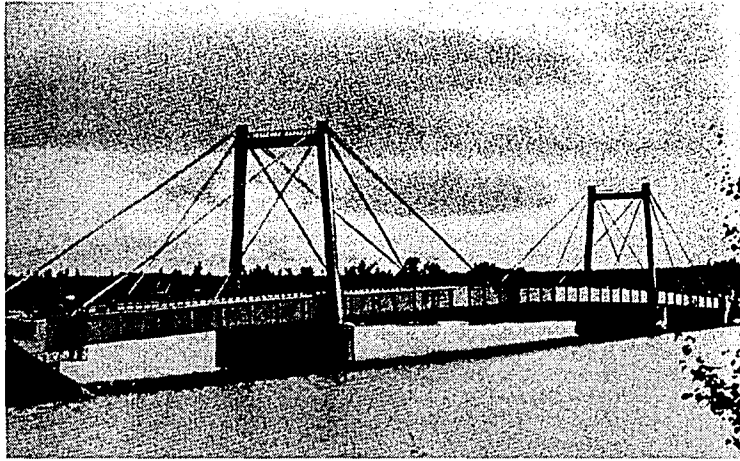
Figure 1.5 View of the Strömsund Bridge in Sweden (Troitsky 1988)
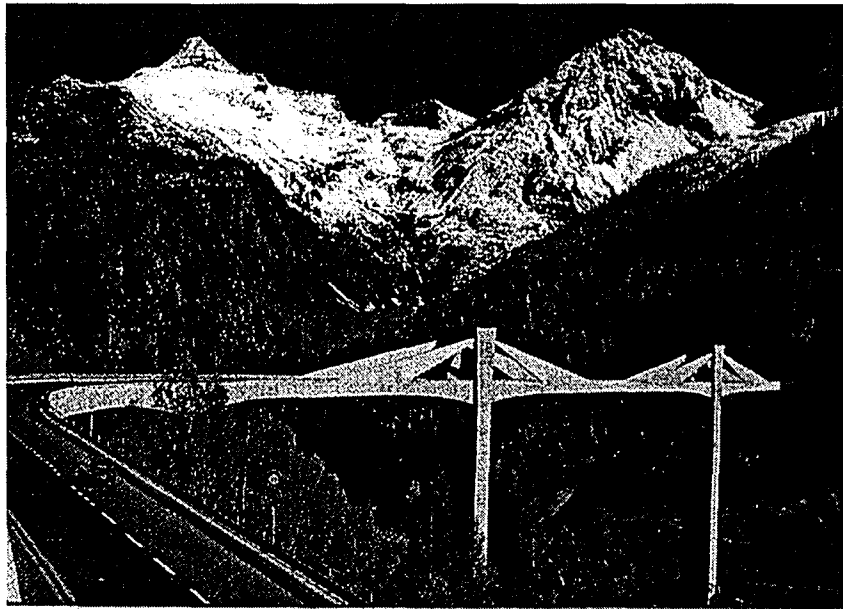
Figure 1.6 View of the Ganter Bridge in Switzerland (Courtesy of
http://en.structurae.de)
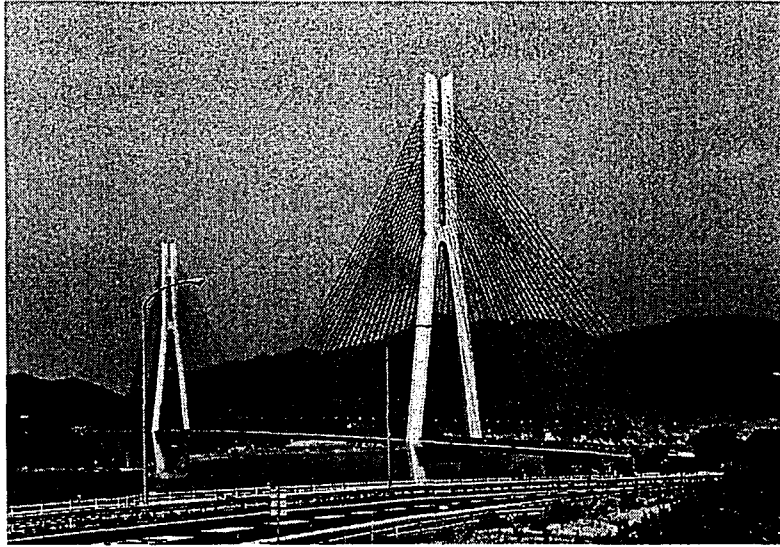
Figure 1.7 View of the Tatara Bridge in Japan (Courtesy of http://www.answers.com)
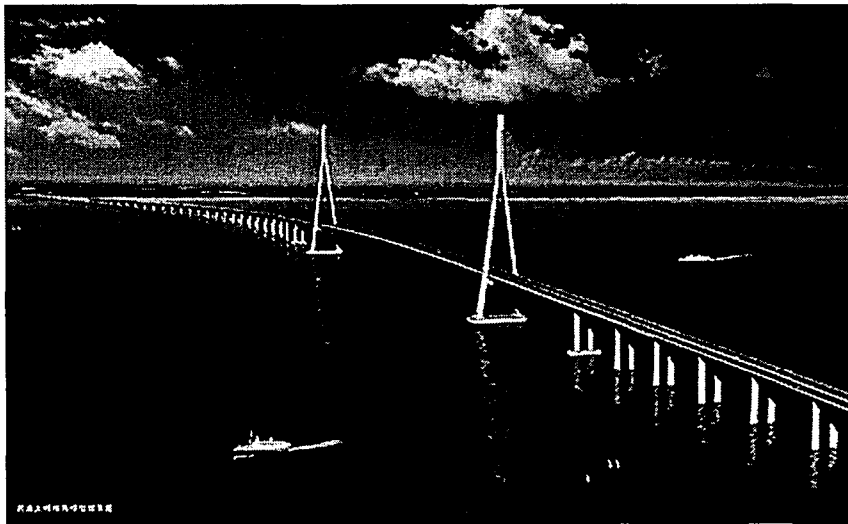
Figure 1.8 View of the Sutong Bridge in China (Courtesy of http://www.roadtraffic-technology.com)
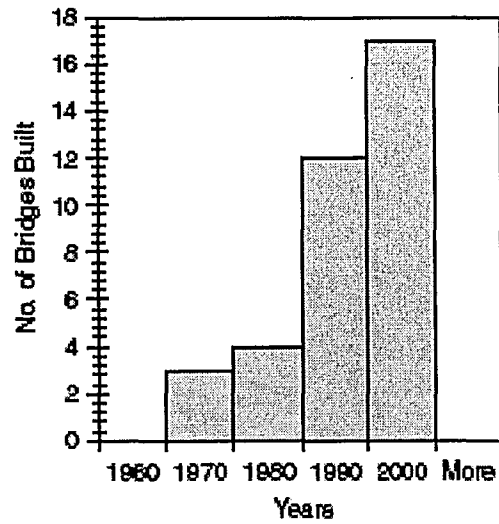
Figure 1.9 Number of cable-stayed bridges built in the United States (Tabatabai 2005)

Figure 1.10 View of the Arthur Ravenel Jr. Bridge in South Carolina (Courtesy of http://ravenelbridge.net)

17
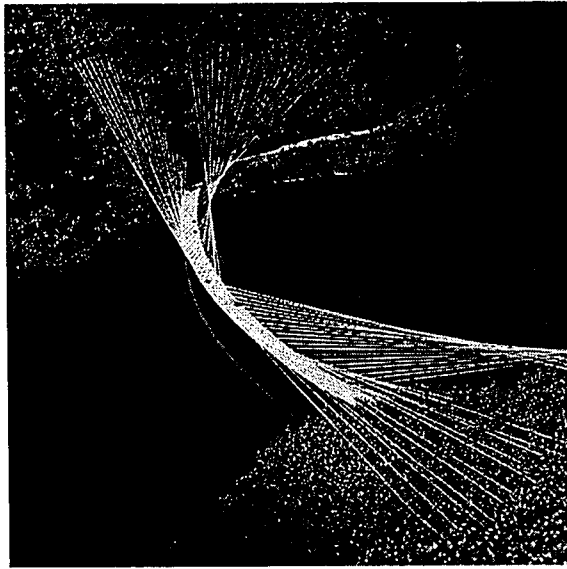
Figure 1.11 The Ruck-A-Chucky Bridge in California (Courtesy of http://www.ketchum.org)

Chapter 2

The Zhao-Bao-Shan Bridge

This chapter provides a general description of the Zhao-Bao-Shan Bridge (hereafter referred to as ZBS Bridge), a reinforced concrete cable-stayed bridge with a 258-m main span and a single tower. A brief description of an engineering accident that occurred during the construction of the ZBS Bridge as well as the corresponding retrofit actions taken to strengthen the bridge are also given in this chapter.

2.1 Location of the ZBS Bridge

The ZBS Bridge crosses the Yong River at its estuary, connecting the Zhao-Ban-Shan and Jin-Ji-Shan in Ningbo, China, as shown in Figure 2.1. Ningbo City is located on the east coast of China, as shown in Figure 2.2. Figure 2.3 shows the location of the ZBS Bridge in the local region of Ningbo City. Complex terrain conditions exist at the site of the ZBS Bridge, which consists of a piedmont marine alluvial plain and denudation buttes. The Jin-Ji-Shan hill on the east side of the ZBS Bridge, has a gradual slope except for some steep slopes due to man excavation; The Zhao-Bao-Shan hill on the west side of the bridge, has steep slopes and even cliffs at some locations. The altitudes of the top of both hills are about 80 m in terms of the Yellow Sea Altitude Level. The piedmont marine alluvial plain was formed during

19

the latter part of the Holocene Epoch and it has gradual terrain with the ground altitude being around 2.5 m to 3.5 m.

The Yong River is about 450 m wide at the location of the ZBS Bridge. A view of the estuary of the Yong River is shown in Figure 2.4. The main navigational channel is on the west-central side of the Yong River and has a water depth of 7 to 10 m. Due to the tide effect, its east side is an alluvial bank with a 150-m wide muddy tidal marsh. The geological bedrock at the bridge site consists of an upper layer with felsophyre and a lower tuff sandstone layer. On top of the bedrock, there lies a 14 to 33 m deep silt layer as well as a muddy clay blanket.

2.2 General Description

The ZBS Bridge is a prestressed concrete cable-stayed highway bridge with a main span of 258 m, a side span of 185 m and approach structures, totaling 568 m. It has a single tower with a height of 148.4 m. The ZBS Bridge was open to traffic on June 8, 2001, after a construction period of six years.

As shown in Figure 2.5, the main structural system of the ZBS Bridge is composed of prestressed concrete box girder, reinforced concrete tower and high-strength steel cables. There are a total of six piers (No. 20 to No. 25 in Figure 2.5) that are aligned to a straight line. No. 22 pier is the main pier that supports the bridge tower, from which the bridge deck surface has a 3% down slope in the longitudinal direction on

both sides. The span configuration is 74.5 m (west approach span) + 258 m (main span) + 185 m (side span) + 49.5 m (side span). The navigation channel is right beneath the main span of the bridge. The clearance for the navigation channel of the bridge is 32 m, which permits the passage of 5000-ton ships. There are transverse and longitudinal displacement restraint device on top of No. 22 pier (see Figure 2.6), pot-shape rubber bearings (Model No.GPZ) at No. 20, 21, 24, 25 piers (see Figure 2.7), and special tension-compression bearings (Model No.GJZF$_4$ plate rubber bearing) at No. 23 pier (see Figure 2.8). There are expansion joints (Model No.SSFB400) in the ZBS Bridge located at Pier No. 20 and No. 25 respectively.

The ZBS Bridge carries six lanes of traffic, with a design speed of 60 km/h for the traffic. The design traffic volume of the bridge is 40,000 to 50,000 vehicles per day. The bridge is designed to resist wind over Grade 12 with a maximum wind speed greater than 32.6 m/s (the design wind speed for bridge deck and tower is 40.3 m/s and 46.5 m/s respectively). Additionally, a total of eight ash transmission pipes with a diameter of 219 mm each are placed in the longitudinal direction along the middle line of the bridge.

2.3 Bridge Deck Structure

A standard cross section of the prestressed concrete box girder of the ZBS Bridge is shown in Figure 2.9. The ZBS Bridge has six traffic lanes, totaling 29.5 m in width.

The prestressed concrete box girder has a height of 2.5 m, with a standard section made up of double cells on the side, a single cell and an open section in the middle. Also, the layout of the carriageway on the deck is shown in Figure 2.10. The configuration of the traffic lanes is 1.5 m (buffer zone) + 11.25 m (for three traffic lanes) + 4.0 m (ash pipe zone) +11.25 m (for three traffic lanes) +1.5 m (buffer zone). The prestressed concrete box decks are made of C50 concrete (cube compressive strength $f_{cu,k}$ = 50 MPa, see note below Table 2.2).

2.4 Stay Cables

The 102 cables are made of high-strength stranded steel wires. 7-mm galvanized steel wires are used. The smallest cross-sectional area of the cables is 4195 mm^2, and the largest cable cross-sectional area is 11583 mm^2. The stay cables are covered with a 5- to 8-mm polyethylene sheath for corrosion protection. The typical spacing between the cable anchors is 8.0 m at the bridge deck and 2.0 m at the tower. The cable forces under dead load only from the maintenance and management manual for the ZBS Bridge are listed in Table 2.3. Also, the cable forces from measurement and design values are also presented in Figure 2.11.

2.5 Bridge Tower (Pylon)

The height of the ZBS bridge tower is 148.4 m. The tower is H-shaped. Each tower leg supports a total of 51 stay cables. The tower is made of C50 concrete with a cube compressive strength, $f_{cu,k}$ equal to 50 MPa. The cross sections of the tower at selected locations along its height are shown in Figure 2.12.

2.6 Foundation of Bridge Pier

The foundation of the ZBS bridge piers consists of deep-rock-socketed friction end-bearing bored piles with varying diameters. The deepest embedded length of the piles is 30 m in the bedrock. The pile caps are also deeply embedded in soil. The pile cap of the bridge towers, made of large volume of concrete, is located below the construction water level by 5 meters. Table 2.1 provides a detailed list of the dimensions of all bridge substructures.

2.7 Major Construction Materials for ZBS Bridge

The properties of the major construction materials used in the ZBS Bridge are summarized in Table 2.2.

2.8 The 1998 Bridge Accident and Corresponding Retrofit Action

2.8.1 The 1998 Engineering Accident of ZBS Bridge

The construction of the ZBS Bridge started in May 1995. On September 24, 1998, an accident happened in the ZBS Bridge when No. 23 segment of the bridge's prestressed concrete box girder was being built and the main span of the bridge was 21 m away from closure. At the time of the accident, the bottom flange plate, inclined web plate and vertical web plate of the concrete girder crushed at the location of No. 16 segment. The locations of No. 23 segment and No. 16 segment are illustrated in Figure 2.13. Immediately after the accident, a series of emergency measures were taken to stabilize the damage condition of the bridge and protect the bridge from further damage.

2.8.2 Retrofit Actions

After the bridge condition became stable after taking emergency measures, the following retrofit actions were made in the main span and side span respectively to strengthen the bridge (ZBS Bridge Maintenance & Management Manual 2002).

(1) Main Span

   i) Partial Removal: nine 8-m long segments in the prestressed concrete box girder as well as 36 stay cables were removed from the bridge. The removed sections are No. 15 to No. 23 segments as shown in Figure 2.14.

24

ii) Strengthening: As seen in Figure 2.14, the part of the bridge deck between Segment 14 and No.24 pier were preserved and strengthened. The length of this whole section is 305 m. Two longitudinal composite beams with embedded channel steel shapes were added at the corner location of the box girder cells. Additionally, the thickness of the inclined web plates in the bridge deck was increased by 10 cm. The details are shown in Figure 2.15.

iii) Rebuilding: No.15 to 25 deck segments, a 3.5-m transition segment on the Zhao-Bao-Shan side, and a 1.5-m closure segment in the main span were rebuilt. Additionally, a total of 44 stay cables were replaced in the retrofitted bridge. A standard cross section of the rebuilt bridge deck is illustrated in Figure 2.9 (a).

(2) 49.5-m Side Span (this span is located between No. 24 and No. 25 piers)

i) Removal: The redundant concrete blocks located on both sides of the bridge deck were cut by 80 cm to reduce the transverse internal force in the upper flange of the bridge deck. The removed part measures 39.84 m in length, from a point 10-m away from Pier 24 to Pier 25.

ii) Strengthening: The thickness of a 12-m long bottom flange plate of the bridge deck was increased by 18 cm. Additionally, four longitudinal diaphragms and two vertical webs were added to the bridge deck along the

retrofitted side span. The details of these vertical webs are illustrated in Figure 2.16.

On October 22, 1999, construction of the main span of the ZBS Bridge was completed. The removal and retrofit project was also successfully finished. From March 20 to April 10, 2001, the main structure of the ZBS Bridge was inspected by the Highway Engineering Test Center of the Ministry of Transportation. The field inspection program included static test, live load test, and ambient vibration test. Based on the test results, the bridge is considered to satisfy the criteria of the China bridge design code. On May 9, 2001, nineteen bridge engineering experts visited and evaluated the condition of the ZBS Bridge. It was concluded that overall the retrofit project was of a good quality. The ZBS Cable-stayed Bridge was opened to traffic on June 8, 2001.

Table 2.1 Dimension of bridge substructures

Pier No.	# of Piles	Pile D (m)	Pile Cap Beam (m)	Pier Column (m)	Pier Cap Beam (m)
20	8	1.5	24x7.8x3.0	3x4, t= 0.8	28.24x3.0x4.0
21	14	2.0	24.5x17x3.5	3x4, t= 0.8	22.50x3.0x4.0
22	20	2.5	40x20x5.5	Tower	-
23	8	1.5	19.5x7.8x3.0	3x4, t= 0.8	-
24	8	1.5	19.5x7.8x3.0	3x4, t= 0.8	20.40x3.0x4.0
25	8	1.5	19.5x7.8x3.0	3x4, t= 0.8	27.10x3.0x4.0

Note: D = diameter

   t = wall thickness (Pier column is made up of hollow reinforced concrete section)

Table 2.2 Properties of major construction materials in the ZBS Bridge

Materials	Strength (MPa)	Elastic Modulus (MPa)	Density (Kg/m³)	Structural Member
Concrete C50	$f_{cu,k}$ = 50	3.45E+04	2500	Deck, Tower
Concrete C30	$f_{cu,k}$ = 30	3.00E+04	2500	Pier
Steel	f_y = 1670	2.00E+05	7849	Stay Cable

Note: The measure of concrete quality is its compressive strength. Compressive strength test is based on the use of cube specimen with a dimension of 150 x 150 x 150 mm. Cube-shaped impermeable molds are filled with concrete during the concrete placement process as specified by the China Concrete Code GB50010-2002. The cubes are then moisture-cured for 28 days, and tested at a specified loading rate after completion of 28-day curing. The compressive strength obtained from such test specimens is termed cube compressive strength $f_{cu, k}$.

No.	Design Value (kN)	Measured Cable Force (kN)			
		Upstream		Downstream	
		Force	Error	Force	Error
C1	2303	2494	8.29%	2577	11.90%
C2	2475	2716	9.74%	2758	11.43%
C3	2418	2605	7.73%	2183	-9.72%
C4	2333	2332	-0.04%	2318	-0.64%
C5	2532	2533	0.04%	2563	1.22%
C6	2706	2791	3.14%	2797	3.36%
C7	2917	2943	0.89%	2986	2.37%
C8	3429	3432	0.09%	3566	4.00%
C9	3138	3135	-0.10%	3157	0.61%
C10	3443	3439	-0.12%	3508	1.89%
C11	3607	3659	1.44%	3637	0.83%
C12	3239	3287	1.48%	3290	1.57%
C13	3653	3692	1.07%	3769	3.18%
C14	3654	3721	1.83%	3721	1.83%
C15	4164	4229	1.56%	4217	1.27%
C16	4342	4388	1.06%	4351	0.21%
C17	4172	4223	1.22%	4183	0.26%
C18	4167	4173	0.14%	4110	-1.37%
C19	4186	4215	0.69%	4327	3.37%
C20	3951	3981	0.76%	4001	1.27%
C21	4329	4275	-1.25%	4393	1.48%
C22	4923	4867	-1.14%	4921	-0.04%
C23	5366	5302	-1.19%	5331	-0.65%
C24	5662	5407	-4.50%	5449	-3.76%
C25	5775	5597	-3.08%	5552	-3.86%
C1'	2163	2311	6.84%	2419	11.84%
C2'	2349	2482	5.66%	2433	3.58%
C3'	2582	2606	0.93%	2615	1.28%
C4'	2634	2622	-0.46%	2600	-1.29%
C5'	2216	2384	7.58%	2295	3.56%
C6'	2728	2849	4.44%	2847	4.36%
C7'	2919	3085	5.69%	3037	4.04%
C8'	3099	3328	7.39%	3345	7.94%

No.	Design Value (kN)	Measured Cable Force (kN)			
		Upstream		Downstream	
		Force	Error	Force	Error
C9'	3250	3457	6.37%	3363	3.48%
C10'	3553	3705	4.28%	3649	2.70%
C11'	3498	3597	2.83%	3655	4.49%
C12'	3094	3206	3.62%	3227	4.30%
C13'	3991	4069	1.95%	3874	-2.93%
C14'	3624	3771	4.06%	3573	-1.41%
C15'	4143	4278	3.26%	4229	2.08%
C16'	3922	3934	0.31%	3899	-0.59%
C17'	3765	3779	0.37%	3762	-0.08%
C18'	3821	3898	2.02%	3829	0.21%
C19'	4317	4343	0.60%	4283	-0.79%
C20'	4281	4169	-2.62%	4292	0.26%
C21'	4536	4456	-1.76%	4420	-2.56%
C22'	5157	4939	-4.23%	4981	-3.41%
C23'	5357	5473	2.17%	5605	4.63%
C24'	5902	5805	-1.64%	5865	-0.63%
C25'	5865	5841	-0.41%	5708	-2.68%
C0'	4759	4977	4.58%	4980	4.64%

Figure 2.1 Overall view of the ZBS Bridge from the Zhaobaoshan Hill side
(downloaded from http://forestlife.info)
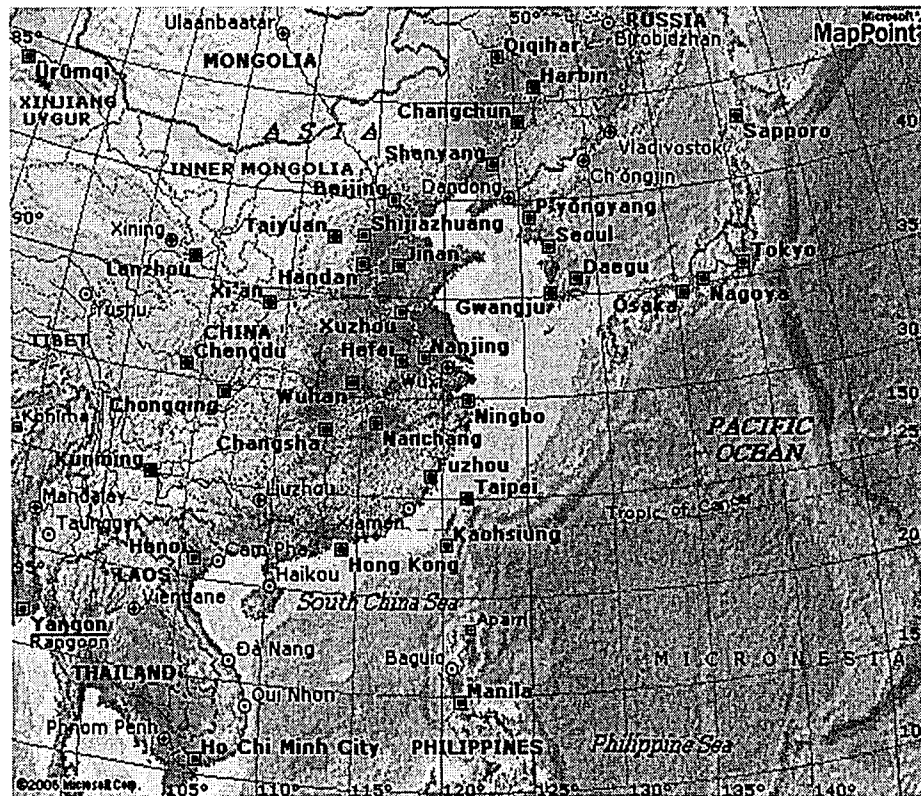
Figure 2.2 Map of China showing the location of Ningbo City (Courtesy of
Microsoft MapPoint)

Figure 2.1 Overall view of the ZBS Bridge from the Zhaobaoshan Hill side
(downloaded from http://forestlife.info)
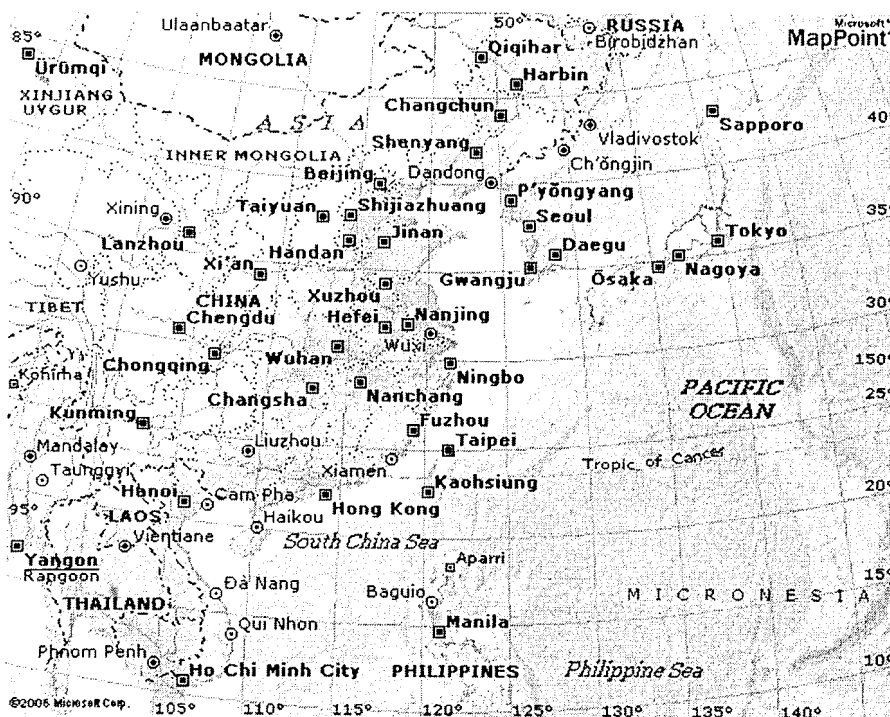
Figure 2.2 Map of China showing the location of Ningbo City (Courtesy of
Microsoft MapPoint)

30
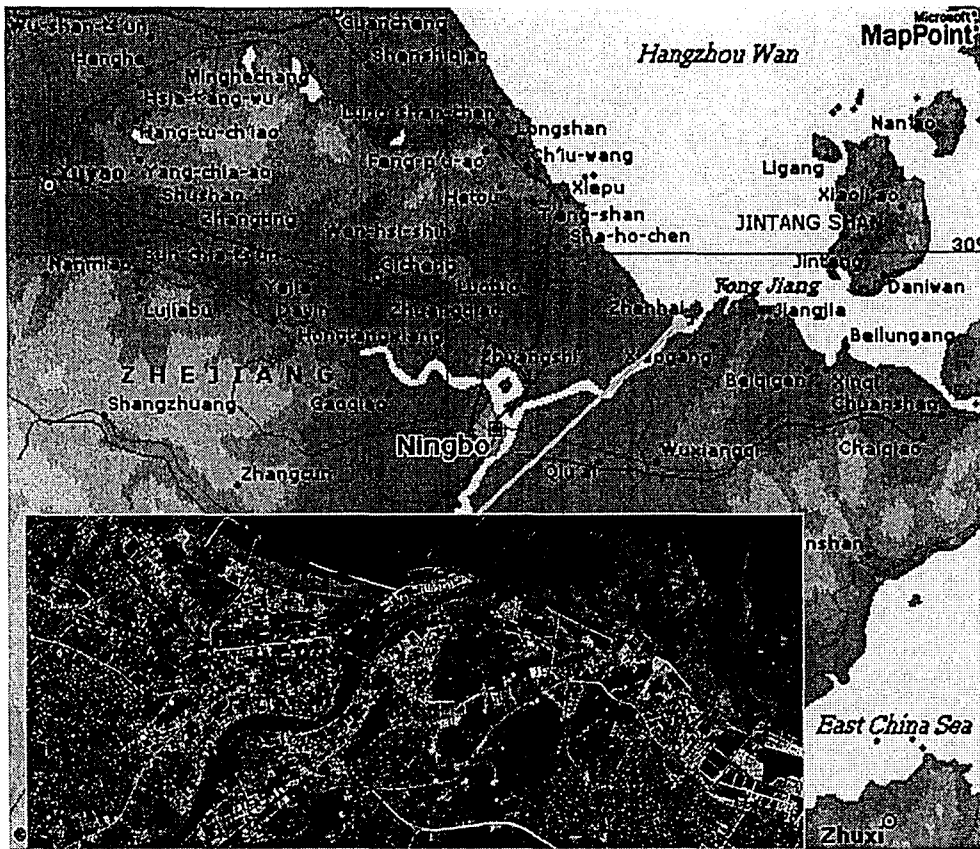
Figure 2.3 Location of the ZBS Bridge in Ningbo City (Courtesy of Microsoft MapPoint)
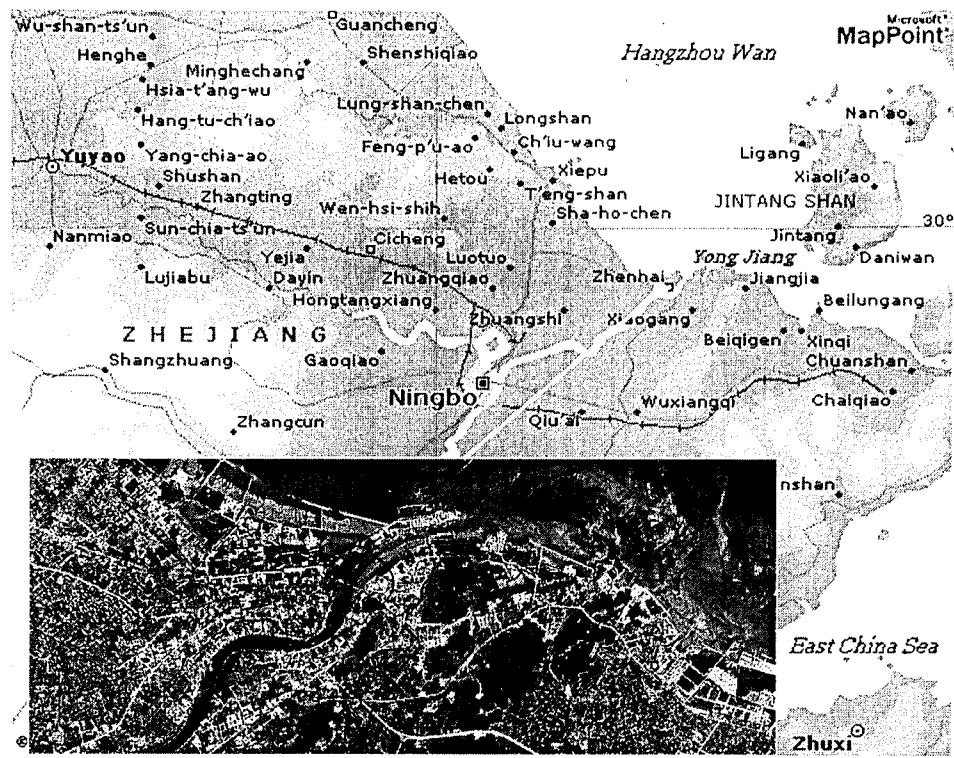
Figure 2.3 Location of the ZBS Bridge in Ningbo City (Courtesy of Microsoft MapPoint)
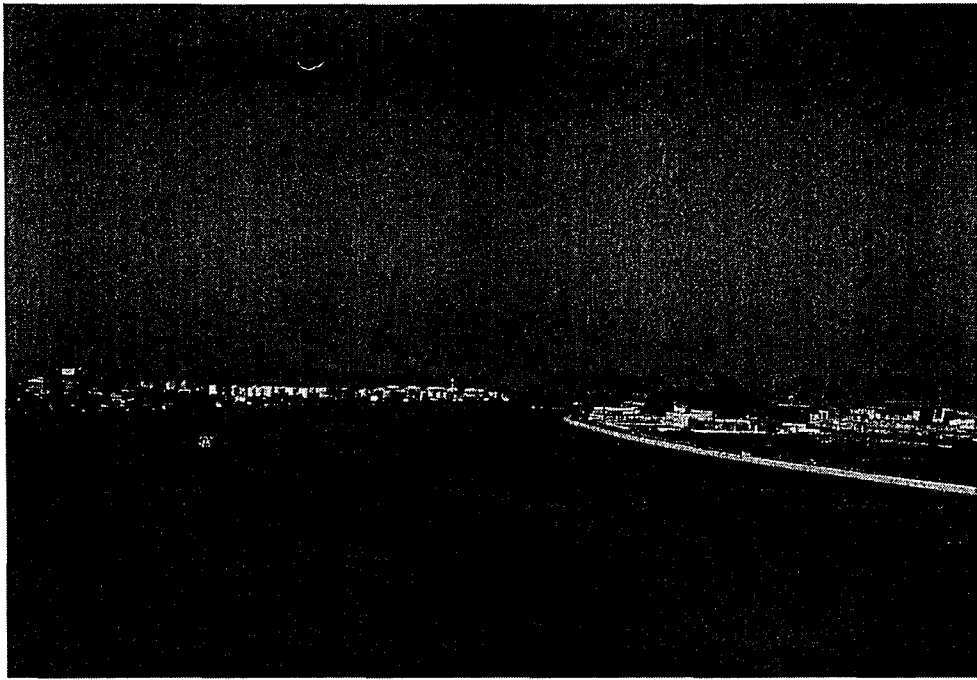
Figure 2.4 View of the estuary of Yong River
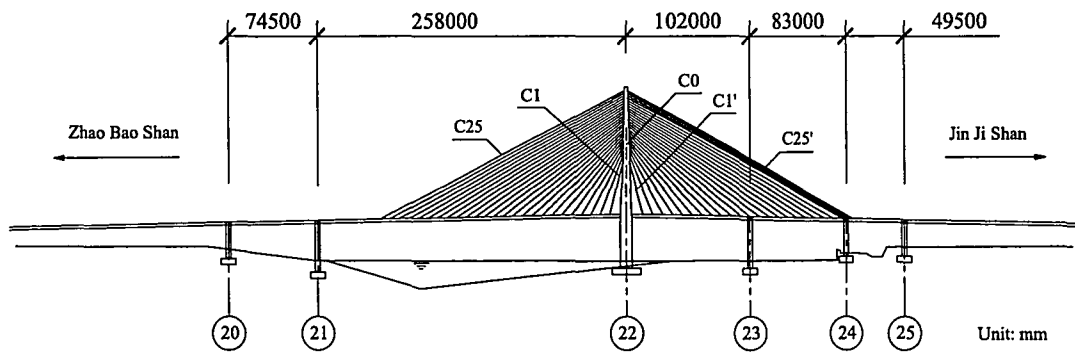
Figure 2.5 Elevation view of the ZBS Bridge

32

225 | 225

横梁中心线 | 主塔中心线 | 横梁中心线 | Deck

75 | 75 | 16 | 134 | 134 | 16 | 75 | 75

2 | 40 | 30 | 124/2 | 124/2 | 30 | 40 | 2

A

D

65

55

Bearing

40

Tower

B | B

40

40

130 | 25 | 40 | 55 | 50 | 50 | 55 | 40 | 25 | 130

340/2 | 340/2

700/2 | 700/2
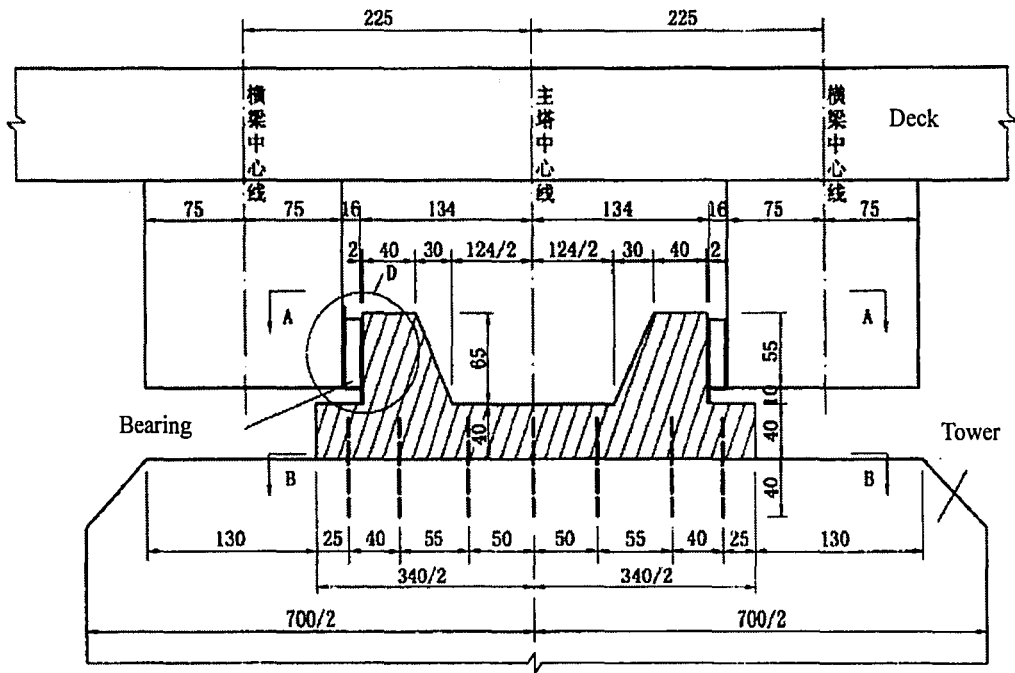
(a) Elevation view of the longitudinal displacement restraint device

Bearing | Bearing | 15

支座中心线

90 | 120

36 | 40 | 30 | 124/2 | 124/2 | 30 | 40 | 36 | 15

2 | 340/2 | 340/2 | 2 | Tower
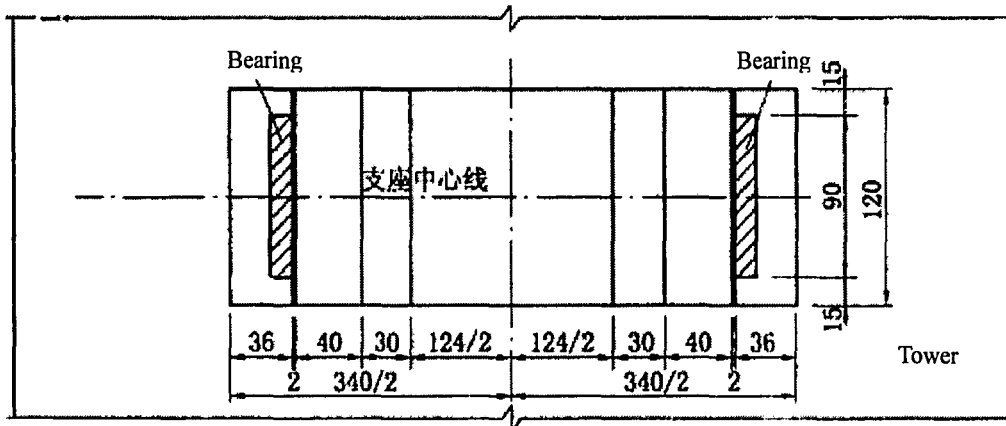
(b) A-A section of the longitudinal displacement restraint device (

Figure 2.6 continued)

33
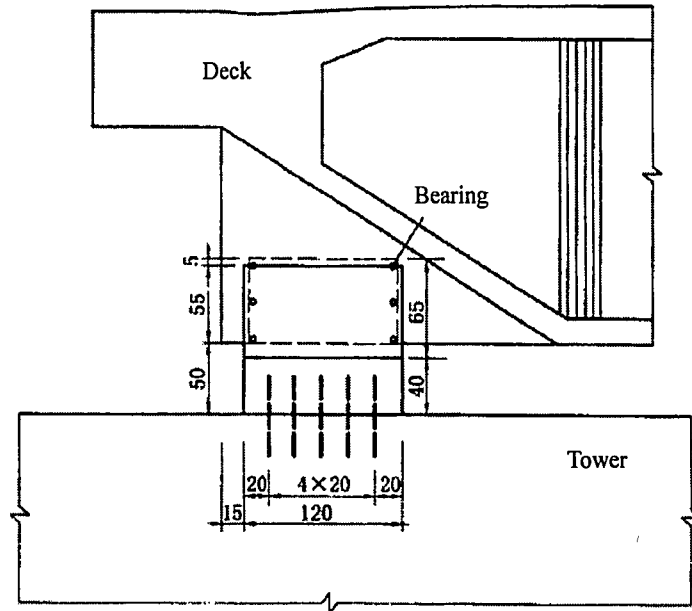
(c) Elevation view of the transverse displacement restraint device
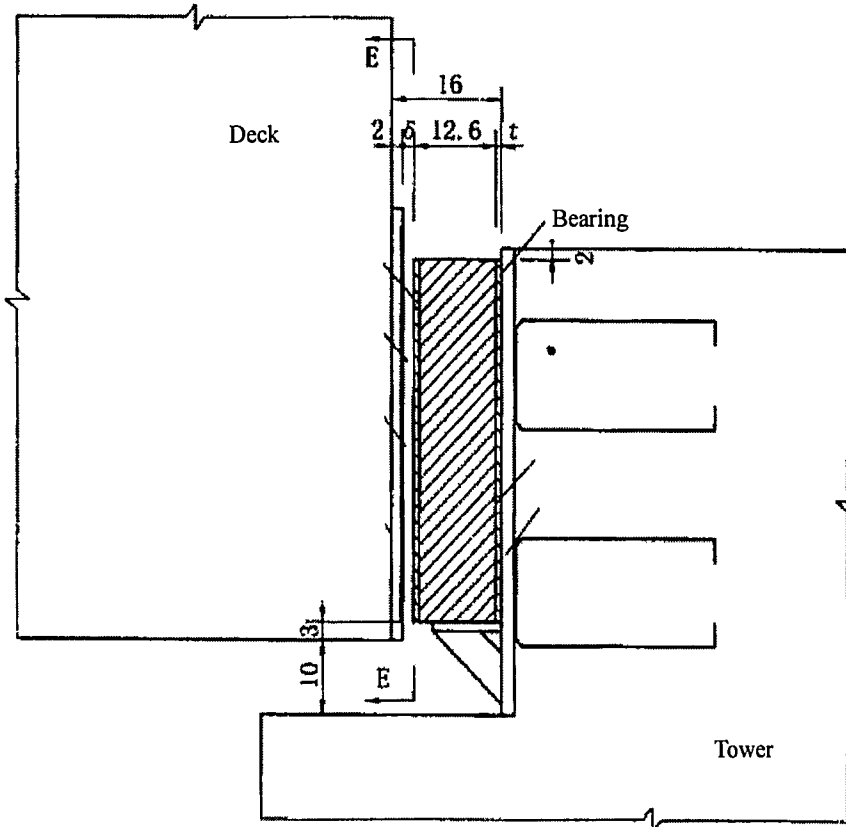
(d) D-D section of the transverse displacement restraint device

Figure 2.6 Details of displacement restraint device at deck/tower connection
(ZBS Bridge Maintenance & Management Manual 2002)
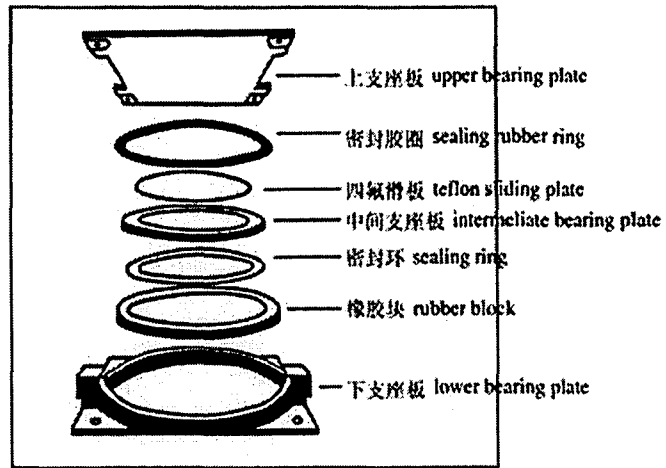
Figure 2.7 GPZ basin-style bearing (Courtesy of Tongji University, China)
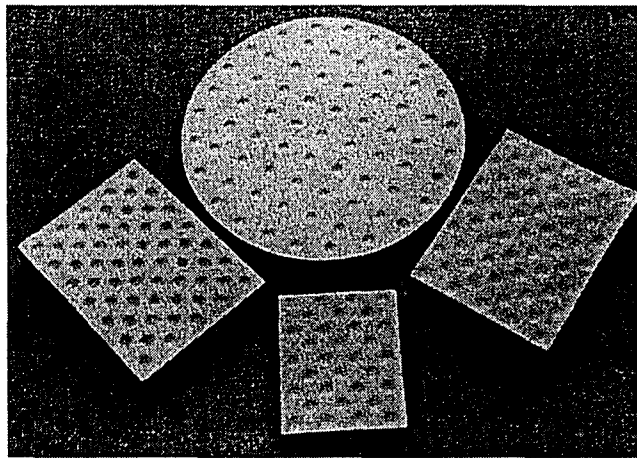
Figure 2.8 GJZF₄ plate rubber bearing (Courtesy of Tongji University, China)
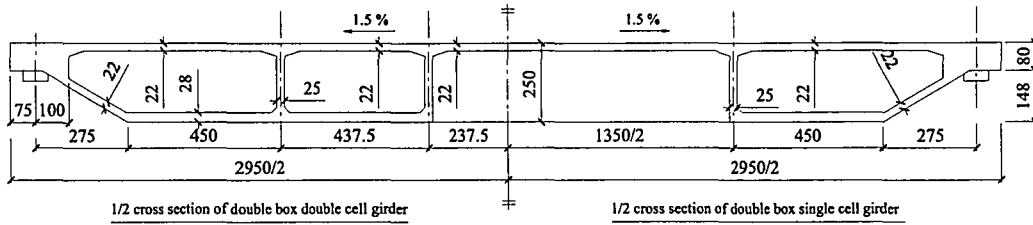
(a) Cross-section of rebuilt bridge deck
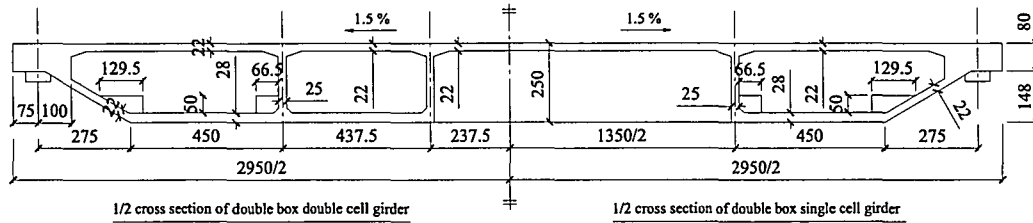
(b) Cross-section of preserved bridge deck

Figure 2.9 Standard deck cross section
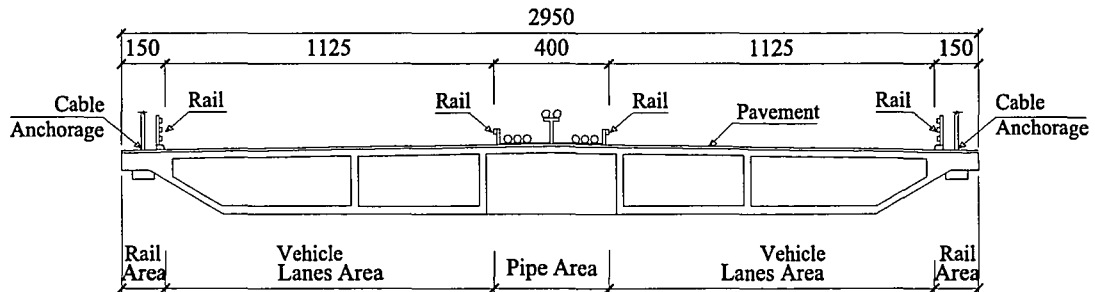
Figure 2.10 Roadway layout on bridge deck
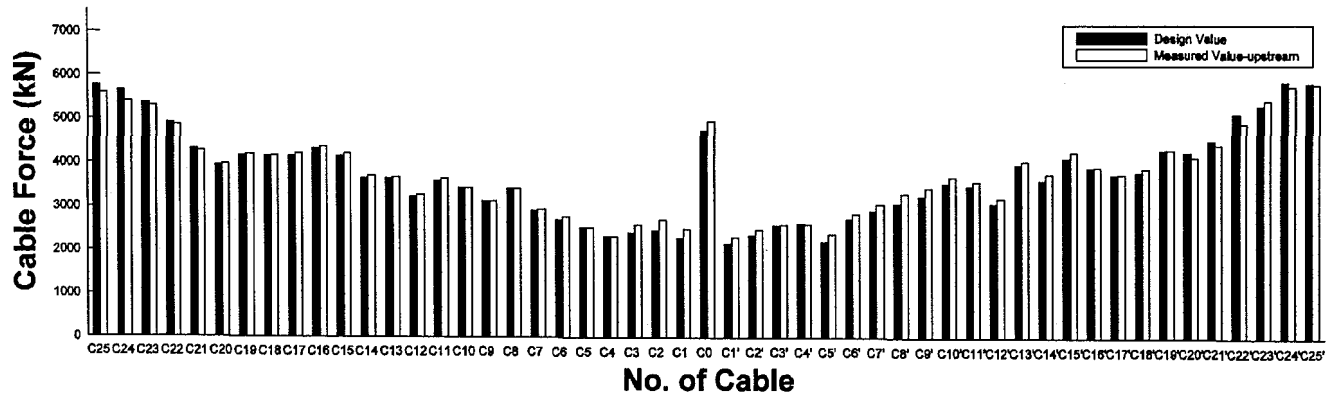
(a) Upstream cable plane
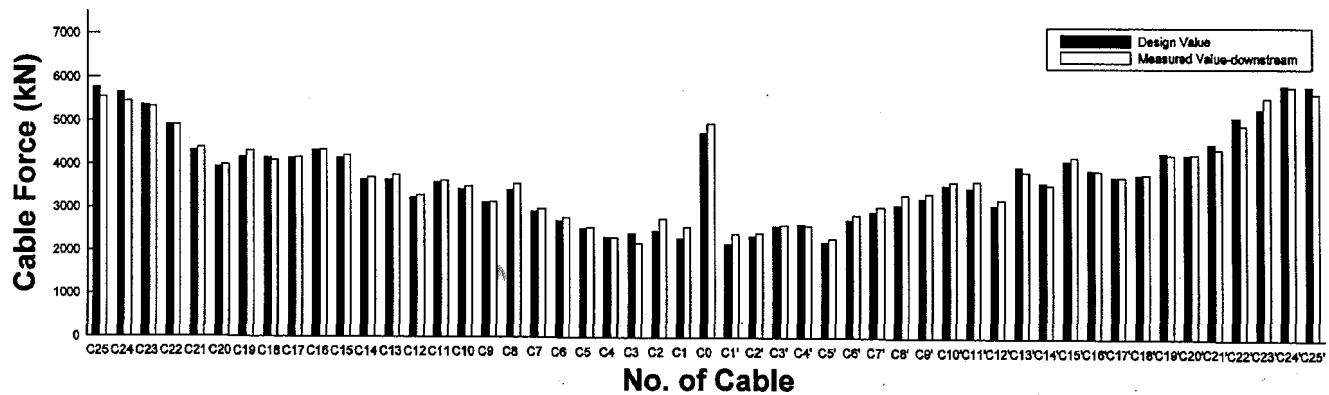
(b) Downstream cable plane

Figure 2.11 Distribution of cable forces measured in September 2001 (ZBS Bridge Maintenance & Management Manual 2002)
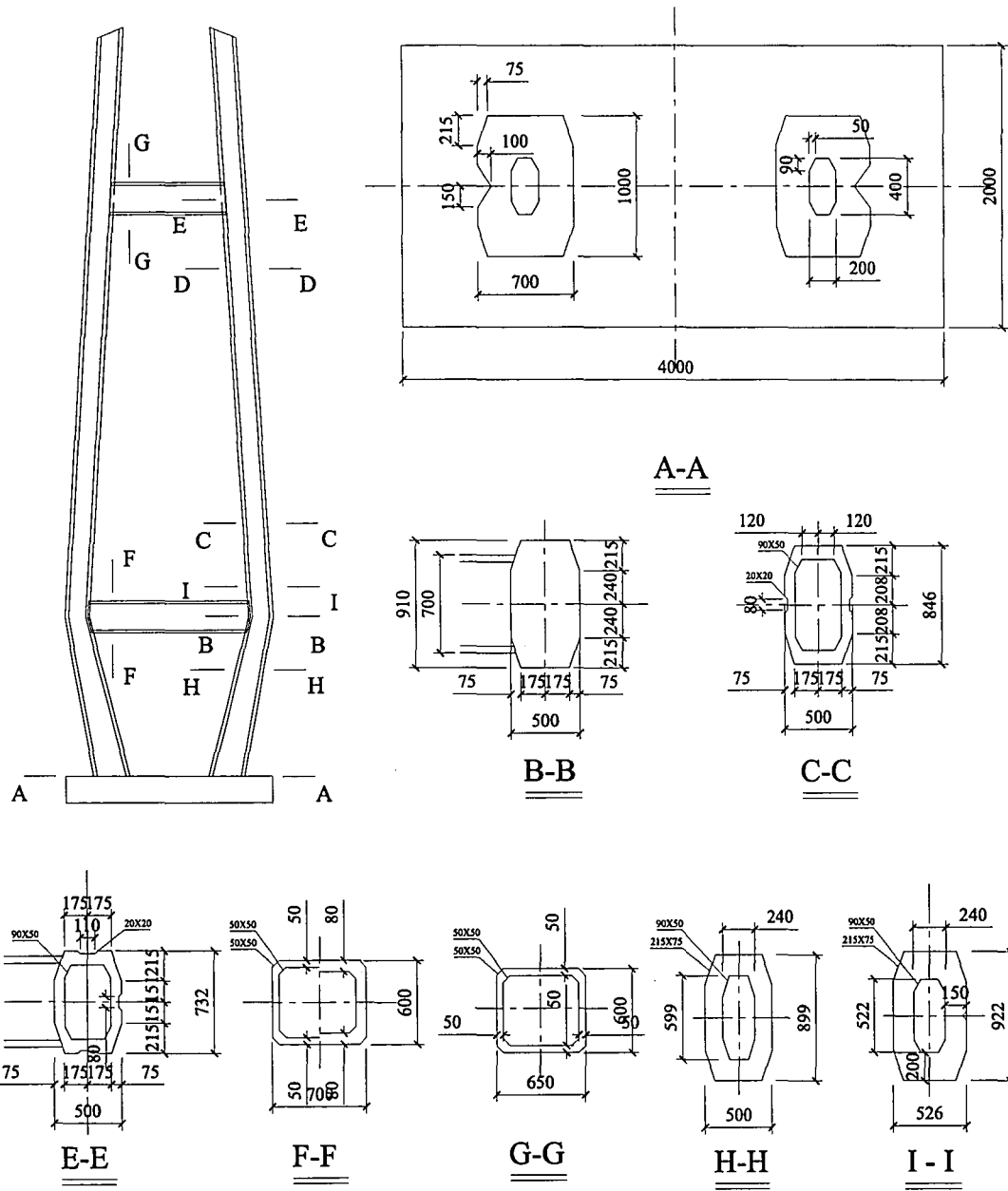
Figure 2.12 Geometry of bridge tower & selected sections (unit: cm)

38

Figure 2.13 Location of Segment No.16 and No.23 during accident

Part I : Cast-in site concrete transition section
Part II : Closure section
Part III : Rebuilt section
Part IV : Case -in site concrete transition section
Part V : Preserved section

Figure 2.14 Location of retrofit section

39
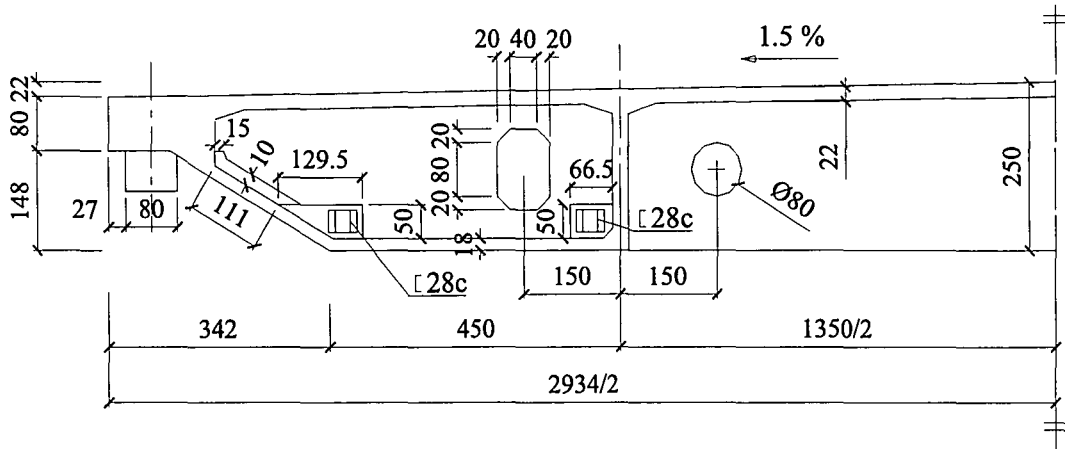
Figure 2.15 Cross-section of strengthened deck portion (Unit: cm)
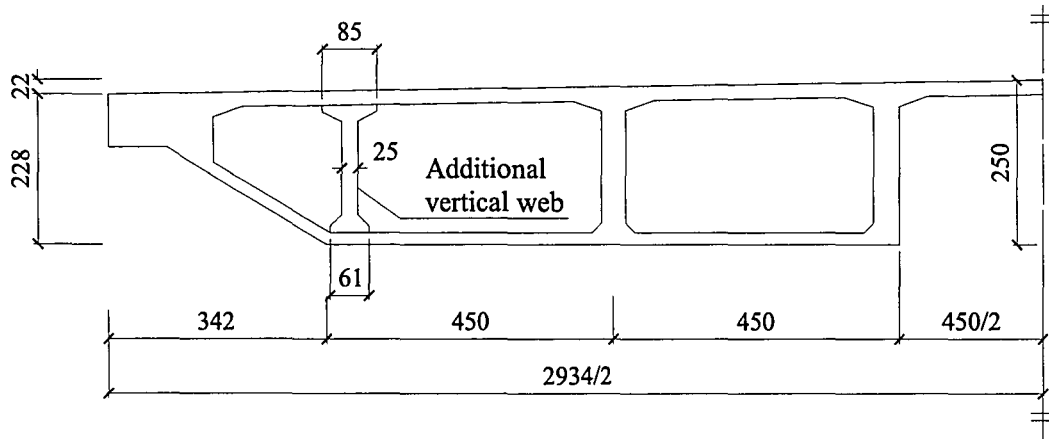
Figure 2.16 Cross-section of retrofit vertical web in the 49.5-m span (Unit: cm)

40

Chapter 3

Static Analysis

This chapter deals with a three-dimensional finite element model developed for static analysis of the Zhao-Bao-Shan (ZBS) Cable-stayed Bridge using the *SAP2000* software. Modeling details as well as the results of static analysis are presented in this chapter.

3.1 Introduction

The objective of this finite element based static analysis is three-fold, as described below,

i)   Static analysis is carried out to better understand the behavior of cable-stayed bridge structures under a variety of loading conditions such as dead load, temperature change, and load combinations.

ii) Field test data from the as-built bridge is used to validate the finite element model, which can then be used to predict the response of the bridge structure under various loading conditions.

iii) The results of static analysis provide essential data such as the deflected equilibrium shape of the bridge deck for subsequent dynamic analysis.

41

3.1.1 Loading Cases

Two types of loads are considered here: dead load and temperature load. The details of these loads are given in the following sections.

(1) Dead load

Two types of dead loads are considered in this study: (i) primary dead load from structural elements and secondary dead load due to gravity of nonstructural elements.

Primary dead load refers to the gravity loads of structural members such as bridge decks, tower (i.e., pylon), piers, cables, and etc. The material densities of the primary structural members are listed in Table 3.1.

Secondary dead loads are gravity load of nonstructural elements placed on the bridge structure after concrete hardened, which include bridge railings, transmission pipes, pavement, and etc. The arrangement of these nonstructural elements is illustrated in Figure 3.1.

The dead loads considered for the cable-stayed bridge in this study can be classified as,

a) Weight per unit volume for concrete: 24.500 kN/m^3

b) Weight per unit volume for steel (stay cable): 76.920 kN/m^3

c) Ash transmission pipe (in operation): 2.176 kN/m per pipe

d) Ash transmission pipe (not in operation): 1.676 kN/m per pipe

e) Water transmission pipe: 5.600 kN/m per pipe (The ash and water transmission pipes are idealized as a concentrated load which is applied in the center of bridge deck)

f) Bridge guide rails: 1.250 kN/m per rail (The guide rails are idealized as

four concentrated loads that are applied in the center and the sides of bridge deck)

g) Pavement: 57.516 kN/m (The pavement has a thickness of 80 mm and is modeled as uniform load on the deck)

(2) Temperature load

Temperature variations are considered in this study to examine the responses of bridge stay cables and concrete structural members under thermal loadings. The thermal expansion coefficient of steel is 1.17E-5 (/°C) while this coefficient is 1.00E-5 (/°C) for concrete. Thermal differentials between the top and bottom surfaces of the concrete deck are also included in this study.

A total of the following five cases are considered for the thermal loading in this study,

a) Temperature Load I (T_1): the temperature of the whole bridge increases by 25 °C.

b) Temperature Load II (T_2): the temperature of the whole bridge decreases by 25 °C.

c) Temperature Load III (T_3): the temperature of the stay cables increases by 15 °C while the temperature of other parts of the bridge does not change.

d) Temperature Load IV (T_4): the temperature of the stay cables decreases by 15°C while the temperature of other parts of the bridge does not change.

e) Temperature Load V (T_5): the temperature of the bottom surface of the bridge deck decreases by 5°C while the temperature of the deck top surface remains unchanged.

3.1.2 Load combination

Various load cases are considered to account for the combined effect of dead loads and temperature change. Details of the individual load cases can be found in the previous sections.

a) Load Combination 0 (LC#0): Dead Load only

b) Load Combination 1 (LC#1): Dead Load + Temperature Load I (D+T$_1$)

c) Load Combination 2 (LC#2): Dead Load + Temperature Load II (D+T$_2$)

d) Load Combination 3 (LC#3): Dead Load + Temperature Load III (D+T$_3$)

e) Load Combination 4 (LC#4): Dead Load + Temperature Load IV (D+T$_4$)

f) Load Combination 5 (LC#5): Dead Load + Temperature Load V (D+T$_5$)

3.2 Experimental Data

3.2.1 Field Test

An extensive series of ambient vibration tests were conducted to measure the dynamic response of the ZBS Bridge from March 20, 2001 to April 10, 2001 (ZBS Bridge Maintenance & Management Manual 2002). Conducting full-scale dynamic tests on bridge is one of the most reliable ways of assessing the actual dynamic properties of cable stayed bridges. The main objective was to experimentally determine the dynamic properties of the ZBS Bridge by conducting an ambient vibration test on the full-scale bridge using wind, water, etc. as the sources of random excitation without any traffic-induced loading or periodic vibration sources. The dynamic properties of principal interest are modal frequencies, mode shapes and information on damping of the structure.

A computer-based data acquisition system was used to collect and analyze the ambient vibration data. The instrumentation system consisted of the following components: (i) a total of 28 vibration transducers (Model 891 from Institute of Engineering Mechanics, Harbin, China) were placed at strategic locations on the bridge. These transducers with built-in amplifier can convert the ambient vibration (velocity or acceleration) signal into electrical signal. (ii) Cabling was used to transmit signals from transducers to the data acquisition system. (iii) Signals were amplified and filtered by signal conditioner.

To accurately identify the mode shapes of the bridge, locations of the vibration transducers must be carefully selected before the vibration test. In the ambient vibration test conducted by the Highway Engineering Inspection Center of the Department of Transportation, China (ZBS Bridge Maintenance & Management Manual 2002), vibration transducers were placed at the quarter points of the main span and mid points of the other spans. Therefore, a total of 28 vibration transducers were placed along both the upstream side and the downstream side of the bridge deck. The location of these transducers on the bridge deck is illustrated in Figure 3.2.

The modal frequencies and mode shapes of the first four dominant modes were identified for the bridge structure. Also, estimations were made for damping ratios based on ambient vibration test data. The experimental data indicates the occurrence of many closely spaced modal frequencies and spatially complicated mode shapes.

Table 3.2 lists four modal frequencies of the ZBS Bridge identified from the experimental data, which correspond to the dominant vertical, lateral, longitudinal and torsional modes, respectively. The modal frequencies of the first vertical, lateral,

45

longitudinal and torsional modes are 0.406 Hz, 0.564 Hz, 0.742 Hz and 0.957 Hz, respectively. The dynamic properties of the ZBS Bridge are characterized as low frequency vibration and small damping ratio.

3.2.2 Temperature-induced deformation measurements

A field survey of the ZBS bridge deflections was conducted by the Institute of Communication Science & Technology at Zhejiang University, China, from 4:00 AM on August 18th, 2001 to 10:00 AM on August 19th, 2001 after the bridge construction was completed (ZBS Bridge Maintenance & Management Manual 2002). During this survey, the bridge was closed to any traffic and the weather condition on these two days was sunny. Bridge deflection data were collected for the tower and the bridge deck. The measurement locations are indicated in Figure 3.3. The experimental data was processed using computers and measured values of the relative deflection for the tower and the bridge deck are summarized in Table 3.3 and Table 3.4, respectively. The following observations were made from the experimental measurements:

i) Lateral and Longitudinal Displacement of Tower: From Table 3.3, the tower displaced horizontally towards the west direction when the temperature increased. The tower returned to its initial position at 4:00 AM on the next day.

ii) Longitudinal Displacement of Deck: As seen in Table 3.4, there is a tendency that the two sides of the deck (i.e., main span and side span) extended westward and eastward, individually, with the increase of environmental temperature. Averagely speaking, the elongation of the west

46

side (main span) was about 1.7 times that of the east side (side span). In the meanwhile, with the decrease of the temperature, the deck deflected in the reverse direction. It was observed that the deck almost returned to its initial configuration at 4:00 AM on the next day. An elongation peak value of 14 mm occurred in the main span deck near pier #21 at 16:00 PM on August 18, 2001.

On August 10, 2001, a total of 86 concrete strain gages were installed to the selected locations inside the box girder cells of the ZBS Bridge in order to measure its thermal response behavior. Gauges were installed at five selected bridge sections in the main and side spans, as shown in Figure 3.4. Two sets of measurements were taken in different seasons: first measurements taken at 7:00 A.M. on August, 13th, 2001 and second measurements taken at 10:00 A.M. on January 12th, 2002. The measured temperature was 18°C and 30°C for the first and second measurements, respectively. The relative changes in strain measurements are listed in Figure 3.5. Using the measured strain and temperature data, sectional restraint stresses and continuity thermal stresses were calculated. However, effects of creep and shrinkage in reducing the effective modulus of elasticity, thereby relieving the thermal continuity stresses, were not considered. It is seen from Table 3.5 that temperature change causes strain in the bridge deck and for the -12 °C temperature difference. The average value of thermal strain is -115 με.

3.2.3 Cable force measurements

In April 2001, after the completion of the ZBS Bridge, the initial cable forces of the bridge under dead load only were measured by the Highway Engineering Inspection Center of the Department of Transportation, China (ZBS Bridge Maintenance & Management Manual 2002). The experimentally measured cable force data are shown in Figure 3.6. The design cable forces are also listed in Table 3.6 for comparison purposes.

3.3 Introduction of Finite Element Analysis Software

3.3.1 SAP2000 Program

SAP2000 version 10.0.0 is utilized in this study for static and dynamic analysis of the ZBS Cable-stayed Bridge. The *SAP* programs were originally developed by Dr. E.L. Wilson et al. at University of California, Berkeley. With a 3D object-based graphical modeling environment and nonlinear analysis capability, the *SAP2000* program provides a general purpose yet powerful finite element analysis software program for structural analysis. This computer program is one of the most popular structural analysis software packages used by structural engineers in the USA.

3.3.2 Frame Element

The frame element in *SAP2000* uses a general, three-dimensional, beam-column formulation, which includes the effects of biaxial bending, torsion, axial deformation, and biaxial shear deformations. Structures that can be modeled with this element include three-dimensional frames, three-dimensional trusses, cables, and etc.

A frame element is modeled as a straight line connecting two points. The frame element activates all six degrees of freedom at both of its connected joints. Each element has its own local coordinate system for defining section properties and loads, and for interpreting output. Figure 3.5 illustrates the frame element in the global coordinate system.

Material properties, geometric properties and section stiffness are defined independent of the frame elements and are assigned to the elements. Each frame element may be loaded by gravity (in any direction), multiple concentrated loads, multiple distributed loads, strain loads, and loads due to temperature change.

If frame elements are supposed not to transmit moments at the ends, the geometric section properties j, i_{33} and i_{22} can be set to zero, or both bending rotations, R_2 and R_3, at both ends and the torsional rotation, R_1, at either end can be released.

In a dynamic analysis, the mass of the structure is used to compute inertial forces. The mass contributed by the frame element is lumped at the joints i and j. No inertial effects are considered within the element itself. The total mass of the element is equal to the integral along the length of the mass density, m, multiplied by the cross sectional area, a, plus the additional mass per unit length, mpl. The total mass is applied to each of the three translational degrees of freedom: UX, UY, and UZ. No mass moments of inertia are computed for the rotational degrees of freedom.

3.3.3 Shell Element

The Shell element is a three- or four-node formulation that combines separate membrane and plate-bending behavior. The four-joint element does not have to be

49

planar. The membrane behavior uses an isoparametric formulation that includes translational in-plane stiffness components and a rotational stiffness component in the direction normal to the plane of the element.

The plate bending behavior includes two-way, out-of-plane, plate rotational stiffness components and a translational stiffness component in the direction normal to the plane of the element. By default, a thin-plate (Kirchhoff) formulation is used that neglects transverse shearing deformation. Alternatively, a thick-plate (Mindlin/Reissner) formulation can be chosen which includes the effects of transverse shearing deformation.

Structures that can be modeled with this element include three-dimensional shells (e.g., tanks and domes), plate structures (e.g., floor slabs), and membrane structures (e.g., shear walls). Each Shell element in the structure can be used to model pure membrane, pure plate, or full shell behavior. The use of full shell behavior is generally recommended unless the entire structure is planar and is adequately restrained.

Each Shell element has its own local coordinate system for defining Material properties and loads, and for interpreting output. Temperature-dependent orthotropic material properties are allowed. Each element may be loaded by gravity and uniform loads in any direction; surface pressure on the top, bottom, and side faces; and loads due to temperature change.

Each Shell element (and other types of area objects/elements) may have either of the following shapes, as shown in Figure 3.6: (i) Quadrilateral, defined by the four joints j_1, j_2, j_3, and j_4. (ii) Triangular, defined by the three joints j_1, j_2, and j_3.. The

50

Shell element always activates all six degrees of freedom at each of its connected joints.

In a dynamic analysis, the mass of the structure is used to compute inertial forces. The mass contributed by the Shell element is lumped at the element joints. No inertial effects are considered within the element itself. The total mass of the element is equal to the integral over the plane of the element of the mass density, *m*, multiplied by the thickness, *th*. The total mass is applied to each of the three translational degrees of freedom: UX, UY, and UZ. No mass moments of inertia are computed for the rotational degrees of freedom.

3.3.4 Linear Static Analysis

Static analyses are used to determine the response of the structure to various types of static loading. These load cases may include: self-weight loads on frame and/or shell elements, temperature loads, etc.

The linear static analysis of a structure involves the solution of the system of linear equations represented by Equation 3.1:

$$K \cdot u = r \tag{3.1}$$

where *K* is the stiffness matrix, *r* is the vector of applied loads, and *u* is the vector of resulting displacements.

For each linear static analysis case, a linear combination of one or more load cases can be defined to apply in the vector *r*. Most commonly, a single loads case in each linear static analysis case can be solved and the results may be combined later.

51

As a load case, temperature load creates thermal strains in the frame and shell elements. These strains are given by the product of the material coefficients of thermal expansion and the temperature change of the element. Two kinds of temperature loads can be specified: uniform temperature change and temperature gradient. The temperature change may be different for individual element in each load case. Temperature load cases are utilized to simulate the environmental temperature difference for the structure in the analysis.

3.3.5 Modal Analysis

Modal analysis is used to determine the vibration modes of a structure. These modes are useful in model calibration with experimental data and calculation of equivalent lateral seismic load for the structure.

There are two types of modal analysis to choose when defining a modal analysis case in *SAP2000*: (i) Eigenvector analysis determines the undamped free-vibration mode shapes and frequencies of the system. These natural modes provide some insight into the behavior of the structure. (ii) Ritz-vector analysis seeks to find modes that are excited by a particular loading. Ritz vectors can provide a better basis than do eigenvectors when used for response-spectrum or time-history analyses that are based on modal superposition.

3.4 FEM Model

3.4.1 Overview

In this study, a three-dimensional finite element model for the ZBS cable-stayed bridge is developed using SAP2000 version 10.0.0, as shown in Figure 3.7. This finite element model has a total of 59070 nodes, 1104 frame elements and 62906 shell elements. More specifically, 58062 nodes and 62906 shell elements are used for the bridge deck; the bridge tower has 356 nodes and 352 frame elements; 549 nodes and 544 frame elements are used for the five bridge piers. The stay cables are modeled using 204 nodes and 102 frame elements. Additionally, 134 nodes and 106 frame elements are employed to model the rigid links in this finite element model. For example, as shown in Figure 3.8, rigid links were used to connect the actual cable anchoring point with the corresponding tower nodes.

3.4.2 Properties of Elements

The material properties of structural members are listed in Table 3.7.

3.4.3 Support Conditions

Boundary conditions at the base of Piers #20, #21, #22 (tower), #23, #24 and #25 are specified such that their motion are restricted in all directions, i.e., they are modeled as fixed end supports.

3.4.4 Constraints

Constraints are applied to restrict the deck from moving in the longitudinal, vertical and lateral direction and rotating around x axis in Pier #20, #21, #23, #24 and #25 while Pier #22, the tower, is assigned with translational constraints in longitudinal and lateral directions and rotational constraints around x axis. In temperature load cases analysis, the longitudinal constraints are released in Pier #20, #21, #23, #24 and #25 in order to simulate the thermal response behavior of the bridge deck on the friction bearings at the top of these piers.

3.4.5 Equivalent Modulus for Cables

When modeling the stay cables, the catenary shape and its variation with the axial force in the cable are modeled with an equivalent elastic modulus. The stay cable can be modeled with a truss element that has a modified modulus of elasticity, E_{eq}, given by Ernst Equation (Ernst 1965).

$$E_{eq} = \frac{E_c}{1 + \left[\dfrac{(wL_x)^2 A_c E_c}{12 T_c^3} \right]} \tag{3.2}$$

where A_c is area of the cross-section, T_c is the tension in the cable, w is its unit weight, L_x is the projected length in the X-Z plane, and E_c is the modulus of elasticity of the cable under tension and is omitted otherwise. The cable elements are modeled as Frame Element in *SAP2000*, and their equivalent elastic moduli are used in the current analysis. The properties of these cables are listed in Table 3.8.

54

3.4.6 Initial Strains in Cables

The equilibrium configuration of a cable-stayed bridge under dead load has to be close to its initial geometry. This can be approximately realized by specifying the initial tension force in the stay cables. The initial cable tension forces are specified as an input quantity (pre-strain) to the corresponding cable element that is determined from the design cable force. Table 3.9 lists the initial tension forces and the input pre-strain correspondingly.

As a result, the maximum vertical deflection at selected locations along the main span is -12 cm, which implies a maximum ratio of deflection to main-span length of 0.05%. In this way, the equilibrium configuration of the bridge deck with design cable strain under dead load is considered as its initial equilibrium configuration.

3.4.7 Frequencies and Mode Shapes

The modal frequencies of the ZBS Bridge from the finite element model are listed in Table 3.10. Additionally, in order to evaluate the accuracy of the FEM results, ambient vibration test data are also given in the same table.

Table 3.11 lists the modal frequency results from the finite element model and from the ambient vibration test. The errors between these results are also given in Table 3.11. It is clearly seen that the finite element model gives a close estimate on frequency for the vertical, longitudinal and rotational mode. The error is 4% for the first vertical mode. Therefore, the finite element model in *SAP2000* is considered to be able to provide relatively reliable results.

55

3.5 FEM Linear Static Analysis Results

3.5.1 Cable forces

Tension forces of selected stay cables (Cable 25, Cable 12, Cable 1, Cable 0, Cable 1', Cable 12', Cable 25') under the afore-mentioned load combinations are tabulated in Table 3.12. The locations of the selected cables are illustrated in Figure 3.9. The design and measured cable forces of the corresponding stay cables are listed in Table 3.13.

The relative changes in selected stay cable tension forces as compared with the values from LC#0 (Dead load only) are listed in Table 3.14. From this table, the following observations can be made:

i) Among all load combinations considered, the cable forces are most sensitive to the thermal loading in cases LC#3 (Dead load + T_3) and LC#4 (Dead load + T_4). This may be explained by the fact that T_3 and T_4 are defined as temperature change in the stay cables. These two load cases are included to study the effect of temperature differentials between the stya cables and the deck on the bridge behavior.

ii) By comparing the results of LC#1 with LC#2 as well as comparing the results of LC#3 with LC#4, it is seen that the change in cable forces are of opposite signs but almost same amplitude except for cable C25' located in side span of the ZBS cable-stayed bridge..

iii) Largest change in cable forces in Cable C25 for all of the five load combination cases considered. C25 is the outermost stay cable in the main span. Therefore, special attention should be given cable C25 when

56

iv)	Among all five load combination cases, LC#5 has the least effect on stay cable force. Less than 1% change in cable forces are observed in all load cases. LC#5 is considered to simulate the thermal differentials between the top and bottom of the bridge deck.

v)	Under dead load only (LC#0), the cable forces from the finite element analysis are in close agreement with the design values and measured values, as shown in Table 3.15.

vi)	As shown in Table 3.15, all cable forces are within 40% of their corresponding yield strength. Therefore, for all five load combination cases considered the stay cables are well within their safety operating range.

3.5.2 Stress of Deck

The stress contour of the bridge deck in the cable-stayed span (i.e., from Cable C25 to Pier 23) under all six load combinations are shown in Figure 3.10 to Figure 3.15. In these figures, half of the surface flange of the bridge deck is removed for clear view of the stress in the bottom flange, longitudinal web and transverse web.

In general, the top flange of the deck is in compression. The compressive stress in the top flange becomes larger when approaching the bridge tower - Pier #22. The bottom flange of the deck is mostly in compression except for the region close to Cable C25. The transverse web is in compression in the upper quarter portion and in tension for the rest part. The longitudinal vertical web is in compression with a distribution pattern similar to that of the top flange. The general stress contour

patterns in these figures appear to be right since the pre-stress in the stay cables combined with dead load lead to the compressive stress in the bridge deck. Additionally, the bridge deck is attached to the stay cables along the two longitudinal sides at the ends of the transverse webs, and thus the upper portion of the transverse web is in compression and the lower portion is in tension.

Although the general stress contour pattern for all six load cases are very close, each load case has slightly different stress contour patterns in selected local areas. For LC#1, the compressive stress in both the top flange and bottom flange is smaller than that of the LC#0 (Dead load only) while for LC#2, opposite changes in the compressive stress of the top and bottom flange of the deck occurs. For LC#3, the top flange compressive stress increases while the bottom flange stress decreases in compression. The stress near Pier 22 and Pier 23 in LC#3 is about the same as that of LC#0. For LC#4, the stresses change reversely. For LC#5, the compressive stresses decrease in both the top and bottom flange, but the difference is not as large as that in LC#3.

When the temperature of the entire bridge increases by 25 °C in LC#1, the deck and the stay cables both elongate. The decrease of compressive stress in the deck implies that the elongation of cables is greater than that of the deck. Therefore, case LC#2 is more critical for the deck in which the compressive stress becomes larger. For LC#5, the temperature differential is smaller, and thus the change in stresses is less than other load combination cases. Also, the temperature gradient which is designed to simulate the different level of sunshine exposure and radiation between the top and bottom surfaces of the deck yields little change in the stress of deck as a

whole.

3.5.3 Comparison with Measurements Data

Table 3.3 lists the displacement changes of the tower estimated by the finite element model due to the temperature change within a 30-hour period. As seen from Table 3.3, the movement of the tower in both the longitudinal and lateral directions is much smaller than the measured values, while the general trend of movement is similar. The tower top displaced westward with the increase of temperature.

The difference between the results of the finite element analysis and the field test data on the displacement of the tower may be due to a couple factors. First of all, the tower is modeled with two-node frame element in the current finite element model. The frame element cannot simulate the thermal gradient in a structural member with a box cross section. If the tower is modeled as shell elements and temperature measurements at different locations of the tower cross section are available, the computed displacement values would be expected to be closer to the experimental data. The deformation of the tower itself induced by thermal gradient contributes a lot to its top displacement. Additionally, the actual environment temperature distribution in the tower, which is very complex and was thus not measured in the field survey, is very challenging to model in the finite element analysis. If the actual nonuniform temperature distribution in the tower is considered, the finite element analysis may give displacement estimations in better agreement with the measured values.

Table 3.4 lists the longitudinal displacement changes of the deck estimated by the finite element model due to temperature change over a 30-hour time period. If the lag

59

effect in temperature change due to the time delay caused by thermal conduction is taken into consideration, the results of this finite element analysis show a good agreement with the measured values for the longitudinal displacements of the bridge deck. Two deck ends extended in the direction consistent with what was observed in the test result. The deformation of the west side deck (main span) is about 1.5 times that of the east side deck (side span), which is consistent with the length ratio of the bridge decks on both sides of the tower.

In reality, the deck exhibits a lag effect in thermal induced displacement according to the field test data. It may be caused by the time required for thermal conduction. However, other factors such as actual environmental conditions (e.g., wind, moisture, etc), or temperature gradient due to the different exposure to the sun may also contribute to the error between the finite element analysis results and field test data. Undoubtedly, in FEM modeling, improved accuracy will result from detailed temperature distribution data from bridge monitoring.

The thermal induced strains at selected sections along the bridge deck are given in Table 3.5 corresponding to the case in which a temperature change of -12 °C occurs in the entire bridge. It is seen that the general tendency of the strain changes in the deck estimated by the FE model is in good agreement with the experimental data. For example, the average estimated value of the strain from FE model is -106 $\mu\varepsilon$, which is very close to the average value of the measured data, -115 $\mu\varepsilon$. The errors between the FE results and measured values are also listed in Table 3.5. In a number lines, large errors are observed, which may be due to measurement errors since the two measurements were done over a 5-month period of time. Additionally, the stresses in

effect in temperature change due to the time delay caused by thermal conduction is taken into consideration, the results of this finite element analysis show a good agreement with the measured values for the longitudinal displacements of the bridge deck. Two deck ends extended in the direction consistent with what was observed in the test result. The deformation of the west side deck (main span) is about 1.5 times that of the east side deck (side span), which is consistent with the length ratio of the bridge decks on both sides of the tower.

In reality, the deck exhibits a lag effect in thermal induced displacement according to the field test data. It may be caused by the time required for thermal conduction. However, other factors such as actual environmental conditions (e.g., wind, moisture, etc), or temperature gradient due to the different exposure to the sun may also contribute to the error between the finite element analysis results and field test data. Undoubtedly, in FEM modeling, improved accuracy will result from detailed temperature distribution data from bridge monitoring.

The thermal induced strains at selected sections along the bridge deck are given in Table 3.5 corresponding to the case in which a temperature change of -12 °C occurs in the entire bridge. It is seen that the general tendency of the strain changes in the deck estimated by the FE model is in good agreement with the experimental data. For example, the average estimated value of the strain from FE model is -106 $\mu\varepsilon$, which is very close to the average value of the measured data, -115 $\mu\varepsilon$. The errors between the FE results and measured values are also listed in Table 3.5. In a number lines, large errors are observed, which may be due to measurement errors since the two measurements were done over a 5-month period of time. Additionally, the stresses in

the longitudinal direction at selected deck sections estimated by the FE model are listed in Table 3.5. The stresses caused by the temperature difference of -12 °C are seen to be minimal.

3.6 Conclusion

The following conclusions can be drawn with regard to the static analysis of the ZBS cable-stayed bridge using the finite element model presented in this chapter,

i) This finite element model established in *SAP2000* is validated with modal frequencies derived from field test data.

ii) The focus of this analysis is on the thermal response behavior of the ZBS cable-stayed bridge due to thermal differentials. The cable forces, deck stresses under six different load combinations are presented. The displacements of the deck and tower as well as the deformations of the deck are compared with experimental data. The FE model results are in good agreement with measured data in both trend and magnitude.

iii) The error between the FE model estimate and field measurements is likely to be caused by: (a) Limitations of the bridge model elements; (b) Idealized simulation of thermal differentials; and (c) Measurement error.

Table 3.1 Material densities of primary structural members

Materials	Density (Kg/m^3)	Structural Members
Concrete	2500	Deck, tower, piers
Stay Cables (Steel)	7849	Stayed cables

Table 3.2 Modal frequencies identified from ambient vibration test data

	Mode	Frequency (Hz)	Damping ratio (%)
1	First Vertical Mode	0.406	0.782
2	First Lateral Mode	0.564	0.501
3	First Longitudinal Mode	0.742	0.431
4	First Rotational Mode	0.957	0.331

Table 3.3 Measured deflection values in bridge tower over a 30-h period (Unit: mm)

Date		08/18/2001		08/18/2001		08/18/2001		08/18/2001		08/19/2001		08/19/2001	
Time		4:00		10:00		16:00		22:00		4:00		10:00	
Temp.		22 °C		27.5 °C		24 °C		22.5 °C		21 °C		27.5 °C	
		Δ_x	Δ_y	Δ_x	Δ_y	Δ_x	Δ_y	Δ_x	Δ_y	Δ_x	Δ_y	Δ_x	Δ_y
Test	T01	0	0	-15.9	9.4	-9.5	7.0	-2.3	-0.3	-1.6	8.4	-16.6	8.6
	T02	0	0	-14.0	0.3	-3.6	4.6	-0.6	3.7	0.3	5.0	-17.0	1.7
FEM	T01	0	0	-1.4	-0.7	-0.5	-0.2	-0.1	0	0.3	0.2	-1.4	-0.7
	T02	0	0	-1.5	0.7	-0.5	0.2	-0.1	0	0.3	-0.2	-1.5	0.7

Table 3.4 Measured deflection values in bridge deck over a 30-h period (Unit: mm)

Date		08/18/2001	08/18/2001	08/18/2001	08/18/2001	08/19/2001	08/19/2001
Time		4:00	10:00	16:00	22:00	4:00	10:00
Temp.		22 °C	27.5 °C	24 °C	22.5 °C	21 °C	27.5 °C
Test	20-1	0	-5.0	-14.0	-6.0	0	-3.0
	20-2	0	-4.5	-13.0	-5.2	-1.0	-3.0
	25-1	0	2.5	9.5	4.0	0	1.0
	25-2	0	2.5	9.0	3.0	0	1.0
FEM	20-1	0	-19.0	-6.9	-1.8	3.4	-19.0
	20-2	0	-19.0	-6.9	-1.8	3.4	-19.0
	25-1	0	13.1	4.8	1.2	-2.3	13.1
	25-2	0	13.1	4.8	1.2	-2.3	13.1

Table 3.5 Deck deformations at selected sections

	u_1 (mm)	u_2 (mm)	Δu (mm)	FE Strain ($\mu\epsilon$)	Experimental Strain ($\mu\epsilon$)	Error	FE σ_{xx} (Mpa)
A-1	31.5948	31.7191	-0.1243	-124	-102	22%	0.06
A-2	31.5890	31.7198	-0.1308	-131	-116	13%	0.32
A-3	31.5823	31.7185	-0.1362	-136	-96	42%	-0.27
A-4	31.5802	31.7175	-0.1373	-137	-96	43%	0.40
A-5	31.9639	32.0901	-0.1262	-126	-124	2%	-0.81
A-6	31.9368	32.0923	-0.1555	-156	-132	18%	-0.11
A-7	31.9325	32.0931	-0.1606	-161	-106	52%	0.05
A-8	31.9343	32.0953	-0.1610	-161	-106	52%	0.53
A-1'	31.5949	31.7191	-0.1242	-124	-138	10%	0.05
A-2'	31.5890	31.7198	-0.1308	-131	-84	56%	0.28
A-3'	31.5823	31.7185	-0.1362	-136	-96	42%	-0.27
A-4'	31.5802	31.7175	-0.1373	-137	-88	56%	0.40
A-5'	31.9639	32.0901	-0.1262	-126	-96	31%	-0.80
A-6'	31.9368	32.0923	-0.1555	-156	-70	122%	-0.10
A-7'	31.9325	32.0931	-0.1606	-161	-136	18%	0.06
A-8'	31.9343	32.0953	-0.1610	-161	-112	44%	0.46
B-1	25.0066	25.1086	-0.1020	-102	-138	26%	0.01
B-2	24.9842	25.0855	-0.1013	-101	-124	18%	0.03
B-3	24.9801	25.0813	-0.1012	-101	-116	13%	0.04
B-4	24.9779	25.0792	-0.1013	-101	-110	8%	0.03
B-5	25.3643	25.4666	-0.1023	-102	-118	13%	-0.07
B-6	25.3666	25.4688	-0.1022	-102	-54	89%	-0.03
B-1'	25.0067	25.1087	-0.1020	-102	-134	24%	0.01
B-2'	24.9843	25.0856	-0.1013	-101	-108	6%	0.03
B-3'	24.9802	25.0813	-0.1011	-101	-116	13%	0.04
B-4'	24.9779	25.0792	-0.1013	-101	-124	18%	0.03
B-5'	25.3643	25.4667	-0.1024	-102	-92	11%	-0.07
B-6'	25.3666	25.4688	-0.1022	-102	-86	19%	-0.03
C-1	11.4585	11.5547	-0.0962	-96	-108	11%	-0.02
C-2	11.4657	11.5618	-0.0961	-96	-108	11%	-0.02
C-3	11.2703	11.3663	-0.0960	-96	-94	2%	-0.01
C-4	11.2702	11.3661	-0.0959	-96	-120	20%	-0.01
C-5	11.3357	11.4317	-0.0960	-96	-144	33%	-0.01

	u_1 (mm)	u_2 (mm)	Δu (mm)	FE Strain ($\mu\varepsilon$)	Experimental Strain ($\mu\varepsilon$)	Error	FE σ_{xx} (Mpa)
C-6	11.3074	11.4034	-0.0960	-96	-110	13%	-0.01
C-1'	11.4587	11.5549	-0.0962	-96	-132	27%	-0.02
C-2'	11.4657	11.5619	-0.0962	-96	-142	32%	-0.02
C-3'	11.2704	11.3664	-0.0960	-96	-112	14%	-0.01
C-4'	11.2702	11.3662	-0.0960	-96	-102	6%	-0.01
C-5'	11.3357	11.4318	-0.0961	-96	-186	48%	-0.01
C-6'	11.3075	11.4035	-0.0960	-96	-92	4%	-0.01
D-1	-12.2146	-12.1280	-0.0866	-87	-116	25%	1.05
D-2	-12.2502	-12.1376	-0.1126	-113	-100	13%	0.67
D-3	-12.2423	-12.1297	-0.1126	-113	-132	15%	0.68
D-4	-12.2627	-12.1285	-0.1342	-134	-124	8%	-1.70
D-5	-12.2398	-12.1318	-0.1080	-108	-156	31%	-1.65
D-1'	-12.2146	-12.1280	-0.0866	-87	-110	21%	1.05
D-2'	-12.2502	-12.1376	-0.1126	-113	-100	13%	0.66
D-3'	-12.2423	-12.1297	-0.1126	-113	-114	1%	0.78
D-4'	-12.2627	-12.1285	-0.1342	-134	-118	14%	-1.72
D-5'	-12.2398	-12.1317	-0.1081	-108	-116	7%	-0.14
E-1	-22.2399	-22.1659	-0.0740	-74	-146	49%	-0.16
E-2	-22.2685	-22.1781	-0.0904	-90	-106	15%	0.48
E-3	-22.2782	-22.1827	-0.0955	-95	-112	15%	-0.33
E-4	-22.2804	-22.1896	-0.0908	-91	-80	14%	-0.19
E-5	-22.2334	-22.1530	-0.0804	-80	-140	43%	-0.75
E-6	-22.3051	-22.2147	-0.0904	-90	-96	6%	-0.15
E-7	-22.3267	-22.2355	-0.0912	-91	-118	23%	-0.75
E-8	-22.3525	-22.2545	-0.0980	-98	-96	2%	-1.14
E-1'	-22.2399	-22.1659	-0.0740	-74	-180	59%	-0.17
E-2'	-22.2685	-22.1781	-0.0904	-90	-134	33%	0.47
E-3'	-22.2782	-22.1827	-0.0955	-95	-90	6%	-0.34
E-4'	-22.2804	-22.1896	-0.0908	-91	-112	19%	-0.19
E-5'	-22.2334	-22.1530	-0.0804	-80	-140	43%	-0.73
E-6'	-22.1367	-22.0497	-0.0870	-87	-112	22%	-0.16
E-7'	-22.3244	-22.2355	-0.0889	-89	-60	48%	-0.74
E-8'	-22.1497	-22.0636	-0.0861	-86	-102	16%	-1.16
F-1	-25.2451	-25.1442	-0.1009	-101	-142	29%	-0.18
F-2	-25.2485	-25.1520	-0.0965	-96	-158	39%	0.01

	u_1 (mm)	u_2 (mm)	Δu (mm)	FE Strain ($\mu\varepsilon$)	Experimental Strain ($\mu\varepsilon$)	Error	FE σ_{xx} (Mpa)
F-3	-25.2496	-25.1553	-0.0943	-94	-84	12%	0.08
F-4	-25.2525	-25.1616	-0.0909	-91	-94	3%	0.21
F-5	-25.2521	-25.1520	-0.1001	-100	-126	21%	-0.12
F-6	-25.2518	-25.1551	-0.0967	-97	-158	39%	0.02
F-7	-25.2514	-25.1563	-0.0951	-95	-202	53%	0.10
F-8	-25.2513	-25.1581	-0.0932	-93	-126	26%	0.18
F-1'	-25.2451	-25.1442	-0.1009	-101	-100	1%	-0.18
F-2'	-25.2485	-25.1520	-0.0965	-96	-172	44%	0.01
F-3'	-25.2496	-25.1553	-0.0943	-94	-50	89%	0.08
F-4'	-25.2525	-25.1616	-0.0909	-91	-76	20%	0.21
F-5'	-25.2521	-25.1520	-0.1001	-100	-126	21%	-0.12
F-6'	-25.2518	-25.1551	-0.0967	-97	-86	12%	0.03
F-7'	-25.2514	-25.1563	-0.0951	-95	-154	38%	0.10
F-8'	-25.2513	-25.1581	-0.0932	-93	-68	37%	0.18

Table 3.6 Measured cable tension force values (Unit: kN)

	Design Value	Measured Cable Force			
		Upstream side		Downstream side	
	T_d	T_m	Error	T_m	Error
C1	2303	2494	8.29%	2577	11.90%
C2	2475	2716	9.74%	2758	11.43%
C3	2418	2605	7.73%	2183	-9.72%
C4	2333	2332	-0.04%	2318	-0.64%
C5	2532	2533	0.04%	2563	1.22%
C6	2706	2791	3.14%	2797	3.36%
C7	2917	2943	0.89%	2986	2.37%
C8	3429	3432	0.09%	3566	4.00%
C9	3138	3135	-0.10%	3157	0.61%
C10	3443	3439	-0.12%	3508	1.89%
C11	3607	3659	1.44%	3637	0.83%
C12	3239	3287	1.48%	3290	1.57%
C13	3653	3692	1.07%	3769	3.18%
C14	3654	3721	1.83%	3721	1.83%
C15	4164	4229	1.56%	4217	1.27%
C16	4342	4388	1.06%	4351	0.21%
C17	4172	4223	1.22%	4183	0.26%
C18	4167	4173	0.14%	4110	-1.37%
C19	4186	4215	0.69%	4327	3.37%
C20	3951	3981	0.76%	4001	1.27%
C21	4329	4275	-1.25%	4393	1.48%
C22	4923	4867	-1.14%	4921	-0.04%
C23	5366	5302	-1.19%	5331	-0.65%
C24	5662	5407	-4.50%	5449	-3.76%
C25	5775	5597	-3.08%	5552	-3.86%
C1'	2163	2311	6.84%	2419	11.84%
C2'	2349	2482	5.66%	2433	3.58%
C3'	2582	2606	0.93%	2615	1.28%
C4'	2634	2622	-0.46%	2600	-1.29%
C5'	2216	2384	7.58%	2295	3.56%
C6'	2728	2849	4.44%	2847	4.36%
C7'	2919	3085	5.69%	3037	4.04%
C8'	3099	3328	7.39%	3345	7.94%

	Design Value	Measured Cable Force			
		Upstream side		Downstream side	
	T_d	T_m	Error	T_m	Error
C9'	3250	3457	6.37%	3363	3.48%
C10'	3553	3705	4.28%	3649	2.70%
C11'	3498	3597	2.83%	3655	4.49%
C12'	3094	3206	3.62%	3227	4.30%
C13'	3991	4069	1.95%	3874	-2.93%
C14'	3624	3771	4.06%	3573	-1.41%
C15'	4143	4278	3.26%	4229	2.08%
C16'	3922	3934	0.31%	3899	-0.59%
C17'	3765	3779	0.37%	3762	-0.08%
C18'	3821	3898	2.02%	3829	0.21%
C19'	4317	4343	0.60%	4283	-0.79%
C20'	4281	4169	-2.62%	4292	0.26%
C21'	4536	4456	-1.76%	4420	-2.56%
C22'	5157	4939	-4.23%	4981	-3.41%
C23'	5357	5473	2.17%	5605	4.63%
C24'	5902	5805	-1.64%	5865	-0.63%
C25'	5865	5841	-0.41%	5708	-2.68%
C0'	4759	4977	4.58%	4980	4.64%

Table 3.7 Material properties of structural members

Materials	E (Mpa)	Density (Kg/m^3)	Poission's Ratio	Coef. of Thermal Expansion (/°C)	Structural Member
Concrete C50	3.45E+04	2500	0.2	1.00E-5	Decks, Tower
Concrete C30	3.00E+04	2500	0.2	1.00E-5	Piers
Steel (Cables)	2.00E+05	7849	0.3	1.17E-5	Cables

Table 3.8 Properties of stay cables

Cable No.	Length (m)	No. of Strands	Area (mm²)	Length Density (Kg/m)	E_{eq} (Mpa)	Cable No.	Length (m)	No. of Strands	Area (mm²)	Length Density (Kg/m)	E_{eq} (Mpa)
C1	45.06	151	5811	45.61	1.999E+05	C1'	45.06	151	5811	45.61	1.999E+05
C2	52.81	109	4195	32.92	1.999E+05	C2'	52.80	109	4195	32.92	1.999E+05
C3	59.55	109	4195	32.92	1.998E+05	C3'	59.55	109	4195	32.92	1.998E+05
C4	66.20	109	4195	32.92	1.998E+05	C4'	66.19	109	4195	32.92	1.998E+05
C5	73.02	127	4887	38.36	1.996E+05	C5'	73.01	127	4887	38.36	1.995E+05
C6	80.62	127	4887	38.36	1.996E+05	C6'	80.62	127	4887	38.36	1.996E+05
C7	87.91	151	5811	45.61	1.993E+05	C7'	87.91	151	5811	45.61	1.993E+05
C8	95.28	151	5811	45.61	1.995E+05	C8'	95.27	151	5811	45.61	1.993E+05
C9	102.78	151	5811	45.61	1.992E+05	C9'	102.77	151	5811	45.61	1.992E+05
C10	110.39	151	5811	45.61	1.992E+05	C10'	110.38	151	5811	45.61	1.993E+05
C11	118.28	187	7196	56.49	1.986E+05	C11'	118.28	187	7196	56.49	1.984E+05
C12	126.07	187	7196	56.49	1.977E+05	C12'	126.06	187	7196	56.49	1.974E+05
C13	133.61	187	7196	56.49	1.981E+05	C13'	133.60	187	7196	56.49	1.985E+05
C14	141.50	187	7196	56.49	1.979E+05	C14'	141.49	187	7196	56.49	1.978E+05
C15	149.43	187	7196	56.49	1.983E+05	C15'	149.43	187	7196	56.49	1.983E+05
C16	157.40	187	7196	56.49	1.983E+05	C16'	157.40	187	7196	56.49	1.978E+05
C17	165.42	187	7196	56.49	1.979E+05	C17'	165.43	187	7196	56.49	1.972E+05
C18	173.46	187	7196	56.49	1.977E+05	C18'	173.48	187	7196	56.49	1.970E+05
C19	181.53	187	7196	56.49	1.975E+05	C19'	181.56	187	7196	56.49	1.977E+05
C20	189.64	187	7196	56.49	1.967E+05	C20'	189.70	187	7196	56.49	1.974E+05
C21	197.84	223	8582	67.36	1.954E+05	C21'	197.83	223	8582	67.36	1.960E+05
C22	206.05	265	10198	80.05	1.943E+05	C22'	206.06	265	10198	80.05	1.950E+05
C23	214.25	265	10198	80.05	1.952E+05	C23'	209.78	301	11583	90.92	1.934E+05
C24	222.46	265	10198	80.05	1.955E+05	C24'	213.41	301	11583	90.92	1.948E+05
C25	230.68	265	10198	80.05	1.954E+05	C25'	217.01	301	11583	90.92	1.946E+05
C0	71.48	223	8582	67.36	1.999E+05						

Table 3.9 Initial forces and pre-strains of stay cables

Cable No.	T_c (kN)	A_c (m²)	E_c (Pa)	Stress (kN/m²)	Pre-strain	Cable No.	T_c (kN)	A_c (m²)	E_c (Pa)	Stress (kN/m²)	Pre-strain
C1	2303	0.005811	1.999E+11	396318	1.983E-03	C1	2303	0.005811	1.999E+11	396318	1.983E-03
C2	2475	0.004195	1.999E+11	590032	2.952E-03	C2	2475	0.004195	1.999E+11	590032	2.952E-03
C3	2418	0.004195	1.999E+11	576443	2.884E-03	C3	2418	0.004195	1.999E+11	576443	2.884E-03
C4	2333	0.004195	1.999E+11	556180	2.782E-03	C4	2333	0.004195	1.999E+11	556180	2.782E-03
C5	2532	0.004887	1.999E+11	518068	2.592E-03	C5	2532	0.004887	1.999E+11	518068	2.592E-03
C6	2706	0.004887	1.999E+11	553670	2.770E-03	C6	2706	0.004887	1.999E+11	553670	2.770E-03
C7	2917	0.005811	1.999E+11	501980	2.511E-03	C7	2917	0.005811	1.999E+11	501980	2.511E-03
C8	3429	0.005811	1.999E+11	590089	2.952E-03	C8	3429	0.005811	1.999E+11	590089	2.952E-03
C9	3138	0.005811	1.999E+11	540011	2.701E-03	C9	3138	0.005811	1.999E+11	540011	2.701E-03
C10	3443	0.005811	1.999E+11	592498	2.964E-03	C10	3443	0.005811	1.999E+11	592498	2.964E-03
C11	3607	0.007196	1.999E+11	501223	2.507E-03	C11	3607	0.007196	1.999E+11	501223	2.507E-03
C12	3239	0.007196	1.999E+11	450087	2.252E-03	C12	3239	0.007196	1.999E+11	450087	2.252E-03
C13	3653	0.007196	1.999E+11	507616	2.539E-03	C13	3653	0.007196	1.999E+11	507616	2.539E-03
C14	3654	0.007196	1.999E+11	507755	2.540E-03	C14	3654	0.007196	1.999E+11	507755	2.540E-03
C15	4164	0.007196	1.999E+11	578623	2.895E-03	C15	4164	0.007196	1.999E+11	578623	2.895E-03
C16	4342	0.007196	1.999E+11	603358	3.018E-03	C16	4342	0.007196	1.999E+11	603358	3.018E-03
C17	4172	0.007196	1.999E+11	579735	2.900E-03	C17	4172	0.007196	1.999E+11	579735	2.900E-03
C18	4167	0.007196	1.999E+11	579040	2.897E-03	C18	4167	0.007196	1.999E+11	579040	2.897E-03
C19	4186	0.007196	1.999E+11	581680	2.910E-03	C19	4186	0.007196	1.999E+11	581680	2.910E-03
C20	3951	0.007196	1.999E+11	549025	2.746E-03	C20	3951	0.007196	1.999E+11	549025	2.746E-03
C21	4329	0.008582	1.999E+11	504440	2.523E-03	C21	4329	0.008582	1.999E+11	504440	2.523E-03
C22	4923	0.010198	1.999E+11	482737	2.415E-03	C22	4923	0.010198	1.999E+11	482737	2.415E-03
C23	5366	0.010198	1.999E+11	526177	2.632E-03	C23	5366	0.010198	1.999E+11	526177	2.632E-03
C24	5662	0.010198	1.999E+11	555202	2.777E-03	C24	5662	0.010198	1.999E+11	555202	2.777E-03
C25	5775	0.010198	1.999E+11	566282	2.833E-03	C25	5775	0.010198	1.999E+11	566282	2.833E-03
C0'	4759	0.008582	1.999E+11	554546	2.774E-03	C0'	4759	0.008582	1.999E+11	554546	2.774E-03

Table 3.10 Modal frequencies of the ZBS bridge calculated from the FE model

Mode #	Period (sec)	Frequency (Hz)	Mode Shape
1	2.562	0.390	vertical
2	1.892	0.528	lateral
3	1.578	0.634	vertical
4	1.393	0.718	lateral
5	1.265	0.790	vertical+long.
6	1.139	0.878	rotational
7	1.119	0.894	vertical
8	0.988	1.012	local
9	0.924	1.082	local
10	0.868	1.151	vertical
11	0.611	1.638	local
12	0.525	1.906	tower lateral+rotational
13	0.523	1.912	tower long.+vertical
14	0.360	2.778	tower lateral+rotational
15	0.244	4.099	local
16	0.193	5.183	tower long.+vertical

Table 3.11 Comparison of modal frequencies from test data and FE model

	Mode	Frequency (Hz)			Period (sec)		
		FEM	Test	Error	FEM	Test	Error
1	First Vertical Mode	0.390	0.406	4%	2.562	2.463	4%
2	First Lateral Mode	0.528	0.564	6%	1.892	1.773	7%
3	First Longitudinal Mode	0.790	0.742	6%	1.265	1.348	6%
4	First Rotational Mode	0.878	0.957	8%	1.139	1.045	9%

Table 3.12 Cable forces in selected stay cables under various load combinations

(Unit: kN)

Cable #	LC#0 (D)		LC#1 (D+T_1)		LC#2 (D+T_2)	
	upstream	downstream	upstream	downstream	upstream	downstream
C25	5478	5478	5395	5395	5560	5561
C12	3030	3030	3036	3036	3024	3024
C1	2477	2477	2489	2489	2465	2465
C0	4897	4897	4919	4919	4875	4875
C1'	2361	2361	2375	2375	2346	2346
C12'	2880	2880	2863	2863	2896	2896
C25'	5583	5583	5543	5542	5646	5646
Cable #	LC#3 (D+T_3)		LC#4 (D+T_4)		LC#5 (D+T_5)	
	upstream	downstream	upstream	downstream	upstream	downstream
C25	5165	5165	5791	5791	5445	5446
C12	3052	3052	3008	3008	3032	3032
C1	2519	2519	2435	2435	2477	2477
C0	4830	4830	4964	4964	4887	4887
C1'	2414	2414	2307	2307	2362	2361
C12'	2805	2805	2955	2955	2876	2876
C25'	5427	5426	5825	5825	5563	5562

Table 3.13 Comparison of cable forces with field test and design values (Unit: kN)

	Design Value	Measured Value	FE Result					
			LC#0	LC#1	LC#2	LC#3	LC#4	LC#5
C25	5775	5428	5478	5395	5561	5165	5791	5446
C12	3239	3414	3030	3036	3024	3052	3008	3032
C1	2303	2529	2477	2489	2465	2519	2435	2477
C0	4759	5187	4897	4919	4875	4830	4964	4887
C1'	2163	2320	2361	2375	2346	2414	2307	2362
C12'	3094	3137	2880	2863	2896	2805	2955	2876
C25'	5865	5775	5583	5543	5646	5427	5825	5563

Table 3.14 Relative change in selected cable force from case LC#0

	LC#0	LC#1	LC#2	LC#3	LC#4	LC#5
C25	0	-1.52%	1.52%	-5.71%	5.71%	-0.58%
C12	0	0.20%	-0.20%	0.73%	-0.73%	0.07%
C1	0	0.48%	-0.48%	1.70%	-1.70%	0.00%
C0	0	0.45%	-0.45%	-1.37%	1.37%	-0.20%
C1'	0	0.59%	-0.64%	2.24%	-2.29%	0.04%
C12'	0	-0.59%	0.56%	-2.60%	2.60%	-0.14%
C25'	0	-0.72%	1.13%	-2.79%	4.33%	-0.36%

Table 3.15 Ratio of cable force to its yield capacity in selected cables under various load combinations

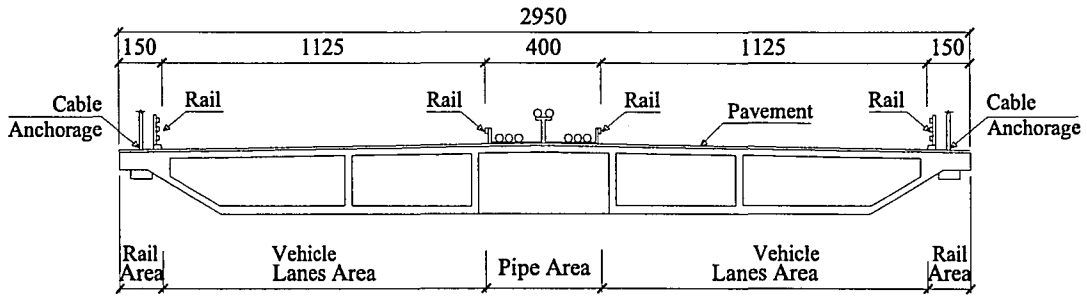| Cable #	Area (m^2)	σ_y (Mpa)	F_y (kN)	Ratio of F/F_y							
				T_d	T_m	LC0	LC1	LC2	LC3	LC4	LC5
C25	0.0101	1670	16900	34%	32%	32%	32%	33%	31%	34%	32%
C12	0.0072	1670	12017	27%	28%	25%	25%	25%	25%	25%	25%
C1	0.0058	1670	9704	24%	28%	26%	26%	25%	26%	25%	26%
C0	0.0086	1670	14332	33%	35%	34%	34%	34%	34%	35%	34%
C1'	0.0058	1670	9704	22%	26%	24%	24%	24%	25%	24%	24%
C12'	0.0072	1670	12017	26%	27%	24%	24%	24%	23%	25%	24%
C25'	0.0116	1670	19339	30%	29%	29%	29%	29%	28%	30%	29%

Figure 3.1 Transverse layout of the ZBS bridge deck
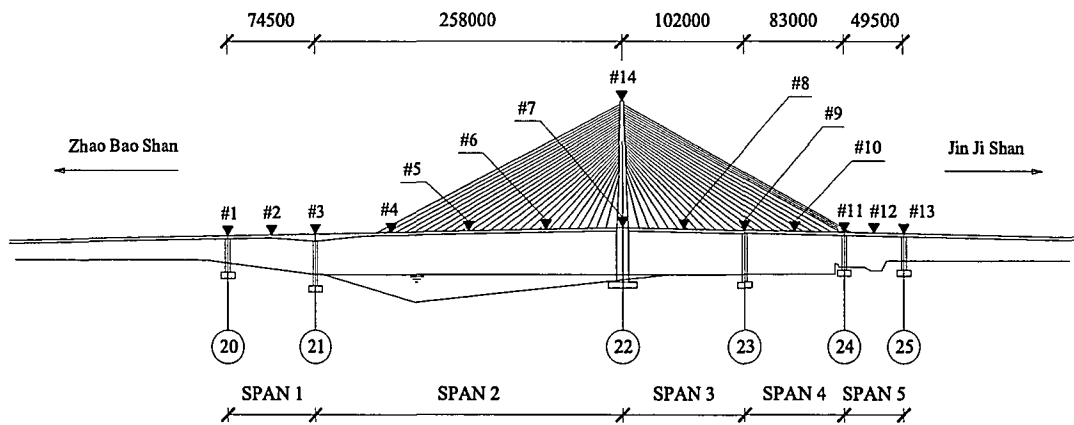
Elevation view of ZBS Bridge
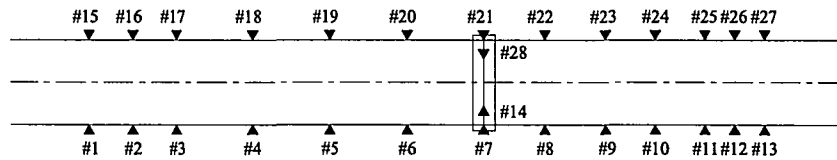
Plan view of ZBS Bridge

Figure 3.2 Transducer locations in ambient vibration test (Unit: mm)

73

74500 258000 102000 83000 49500

#T01 (#T02)

Zhao Bao Shan

Jin Ji Shan

#20-1 (#20-2)

#25-1 (#25-2)

20 21 22 23 24 25

SPAN 1 SPAN 2 SPAN 3 SPAN 4 SPAN 5

Elevation view of ZBS Bridge

#20-2 #25-2

#T02

#T01

#20-1 #25-1

Plan view of ZBS Bridge
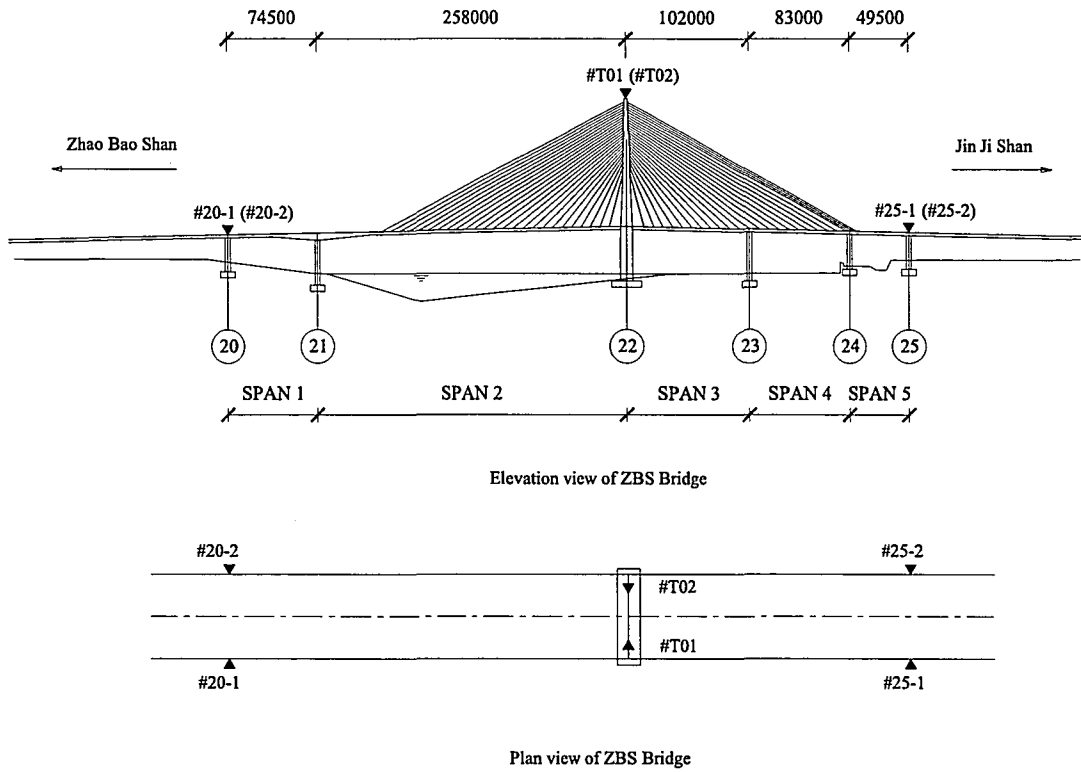
Figure 3.3 Locations of displacement survey stations on the ZBS Bridge (Unit: mm)
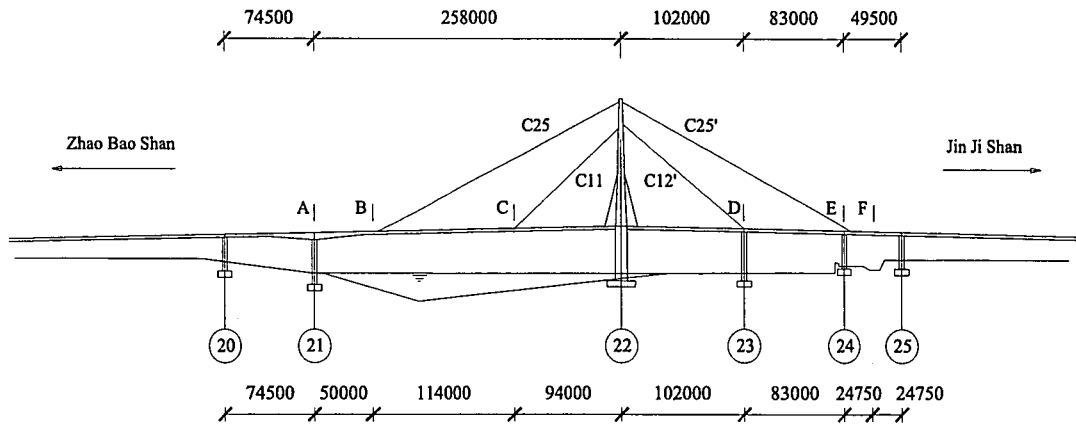
(a) Locations of sections with strain measurement (Unit: mm)
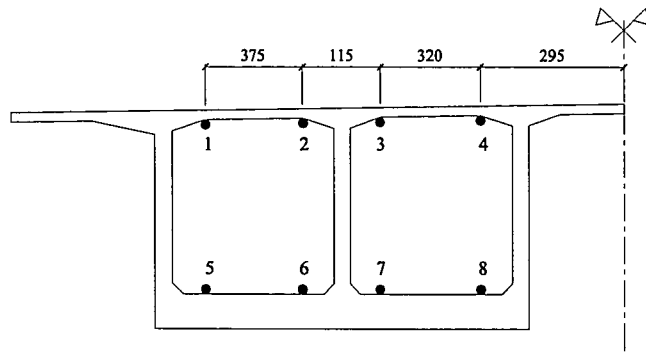
(b) Section A (unit = cm)
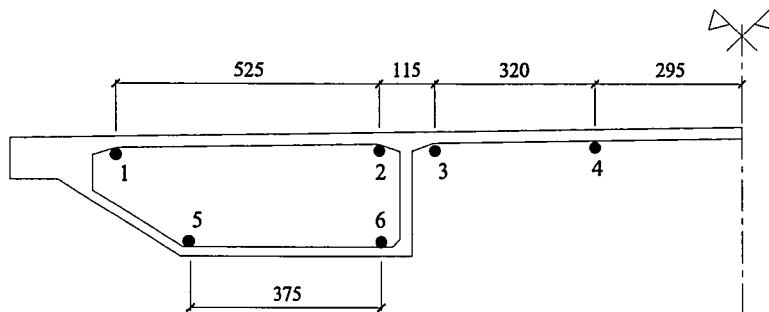
(c) Section B (unit = cm)

(**Figure 3.4** continued next page)

75
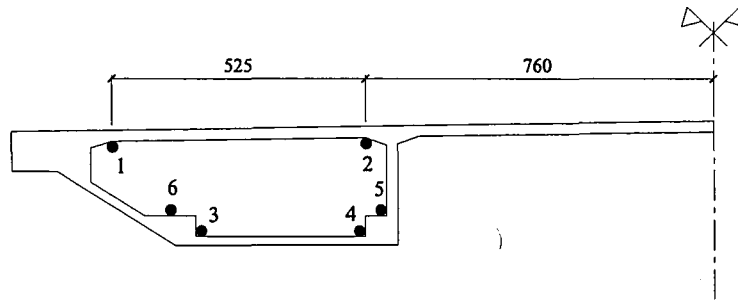
(d) Section C (unit = cm)
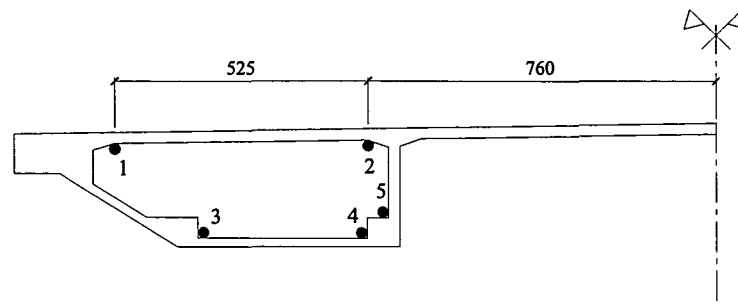
(e) Section D (unit = cm)
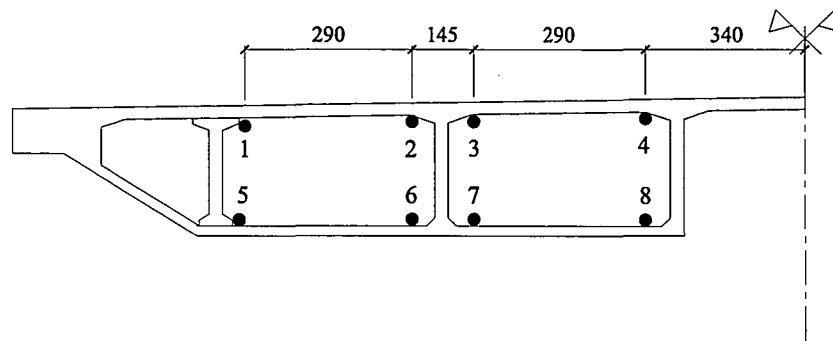
(f) Section E, F (unit = cm)

Figure 3.4 Locations of concrete strain gauges in selected bridge sections
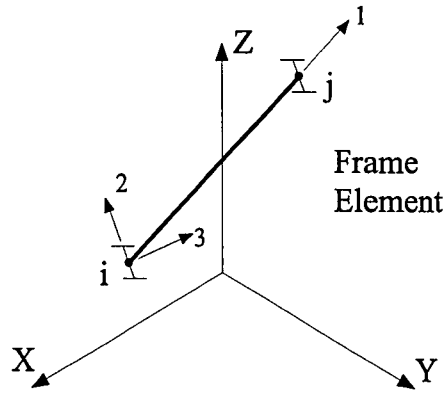
Figure 3.5 Frame element

Four-node Quadrilateral Shell Element

Three-node Triangular Shell Element
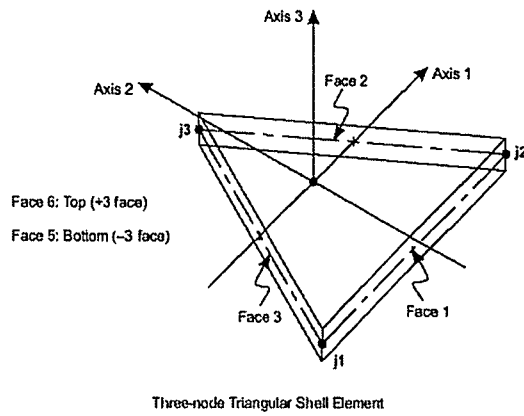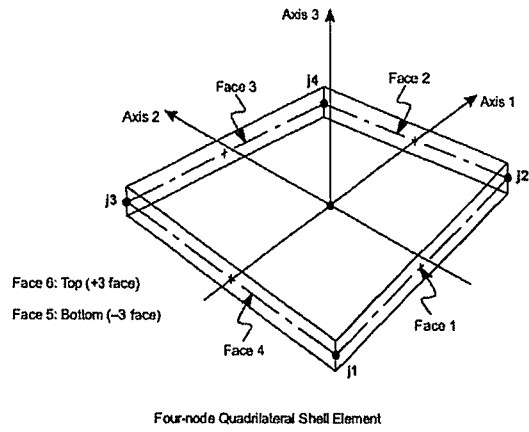
Figure 3.6 Shell element

77
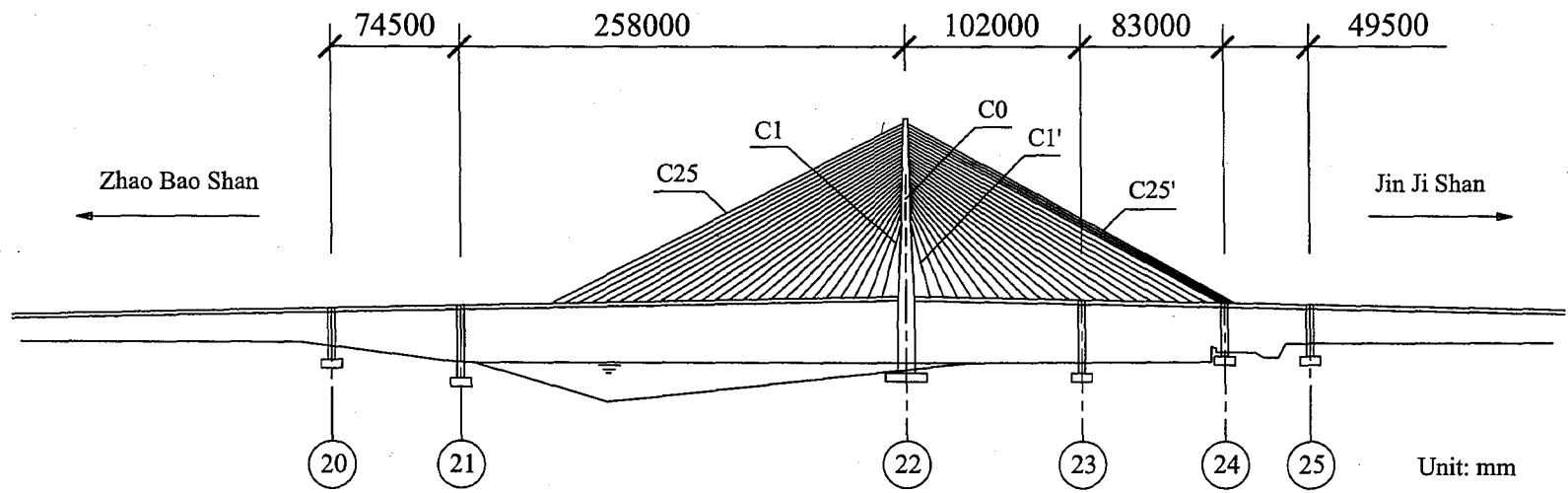
(a) Elevation view of the ZBS Bridge (**Figure 3.7** continued)
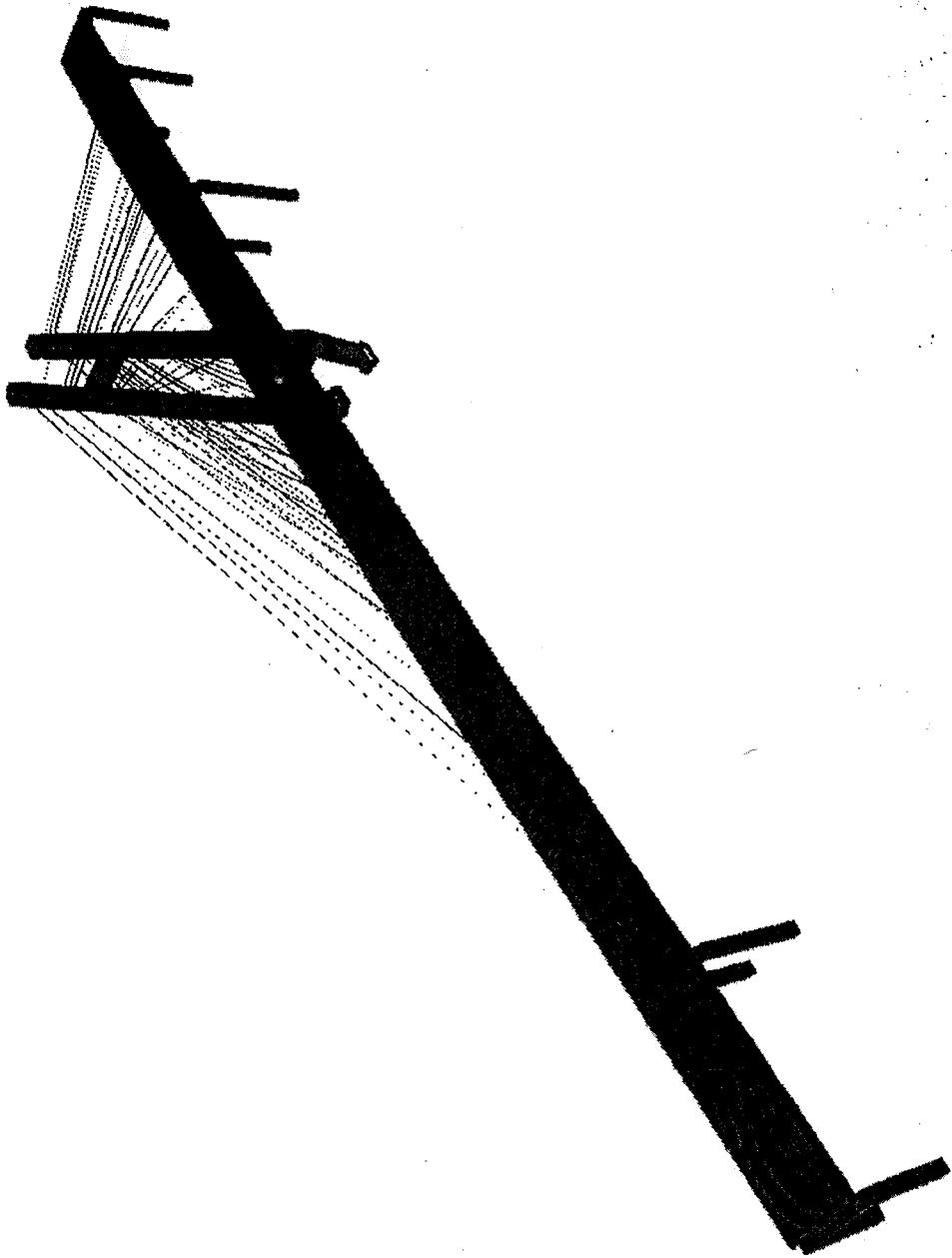
(b) Extruded view of 3-D FEM model (**Figure 3.7** continued)

79
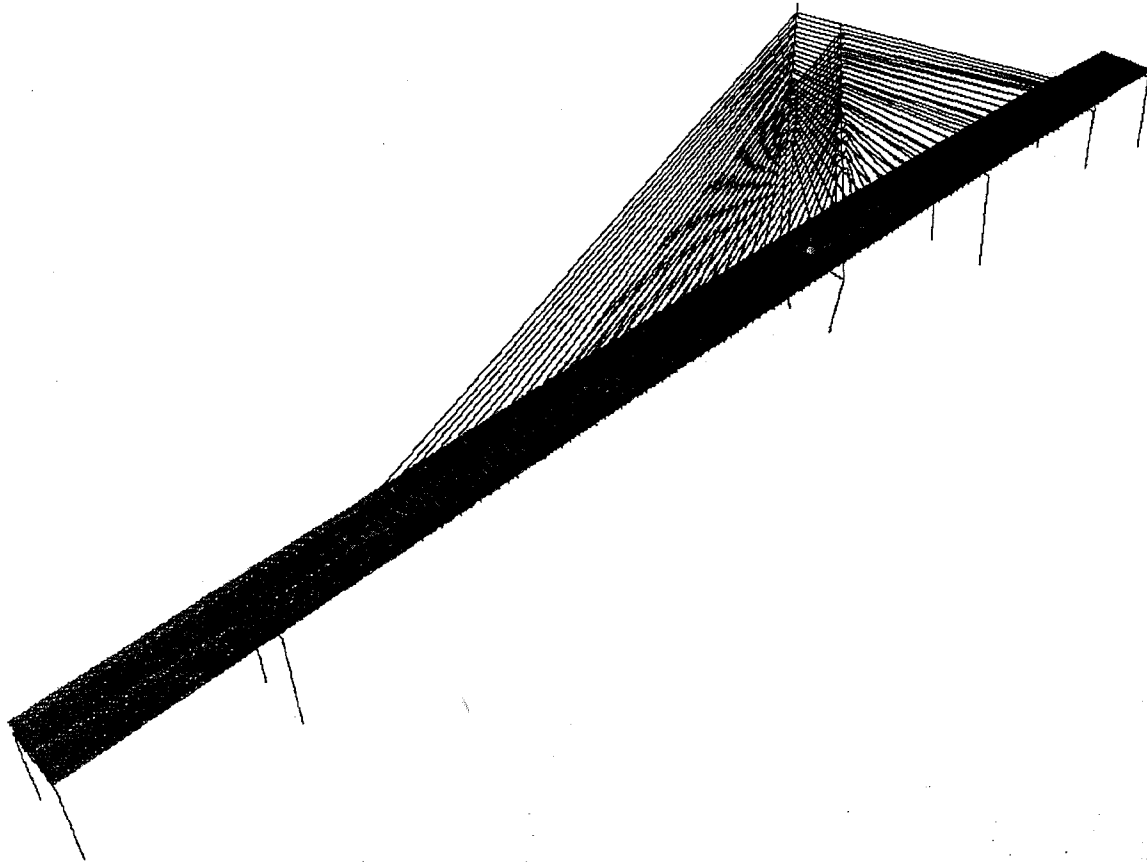
(c) Wire frame view of 3-D FEM model

Figure 3.7 Global view of the finite element model of the ZBS Bridge
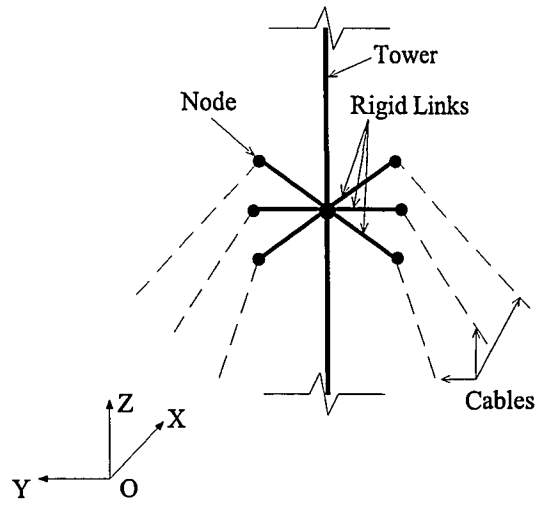
Figure 3.8 Connections between tower and cables
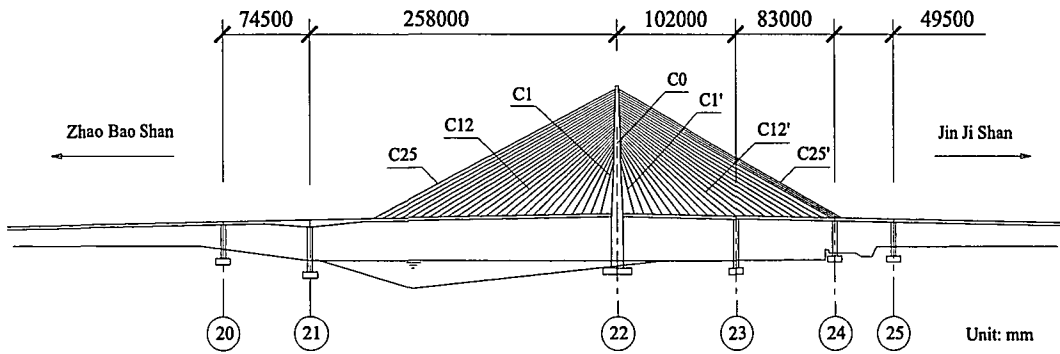
Figure 3.9 Locations of selected cables in the ZBS Bridge

81
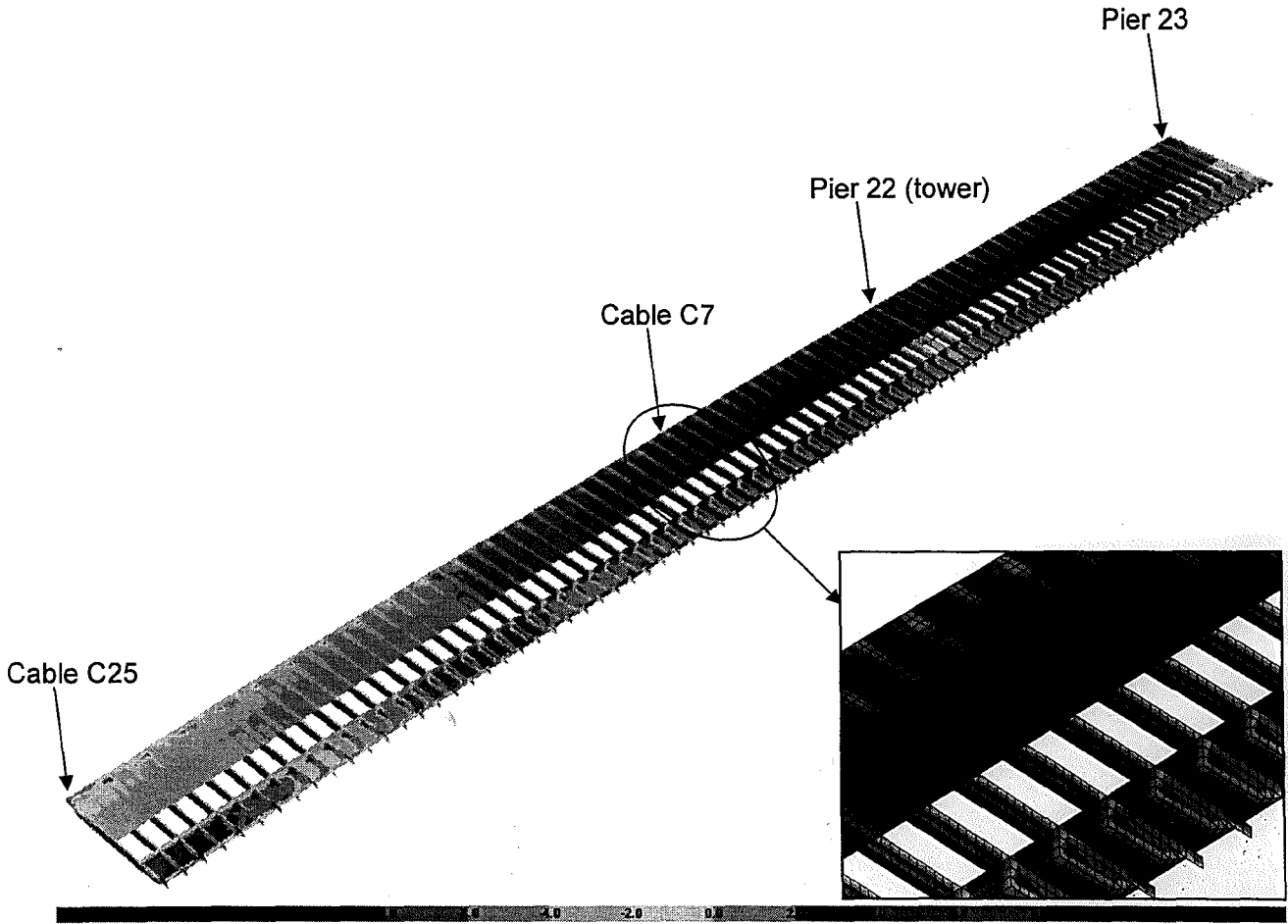
Figure 3.10 Stress contour of bridge deck in stay cable span under case LC#0 (Dead load only)

82
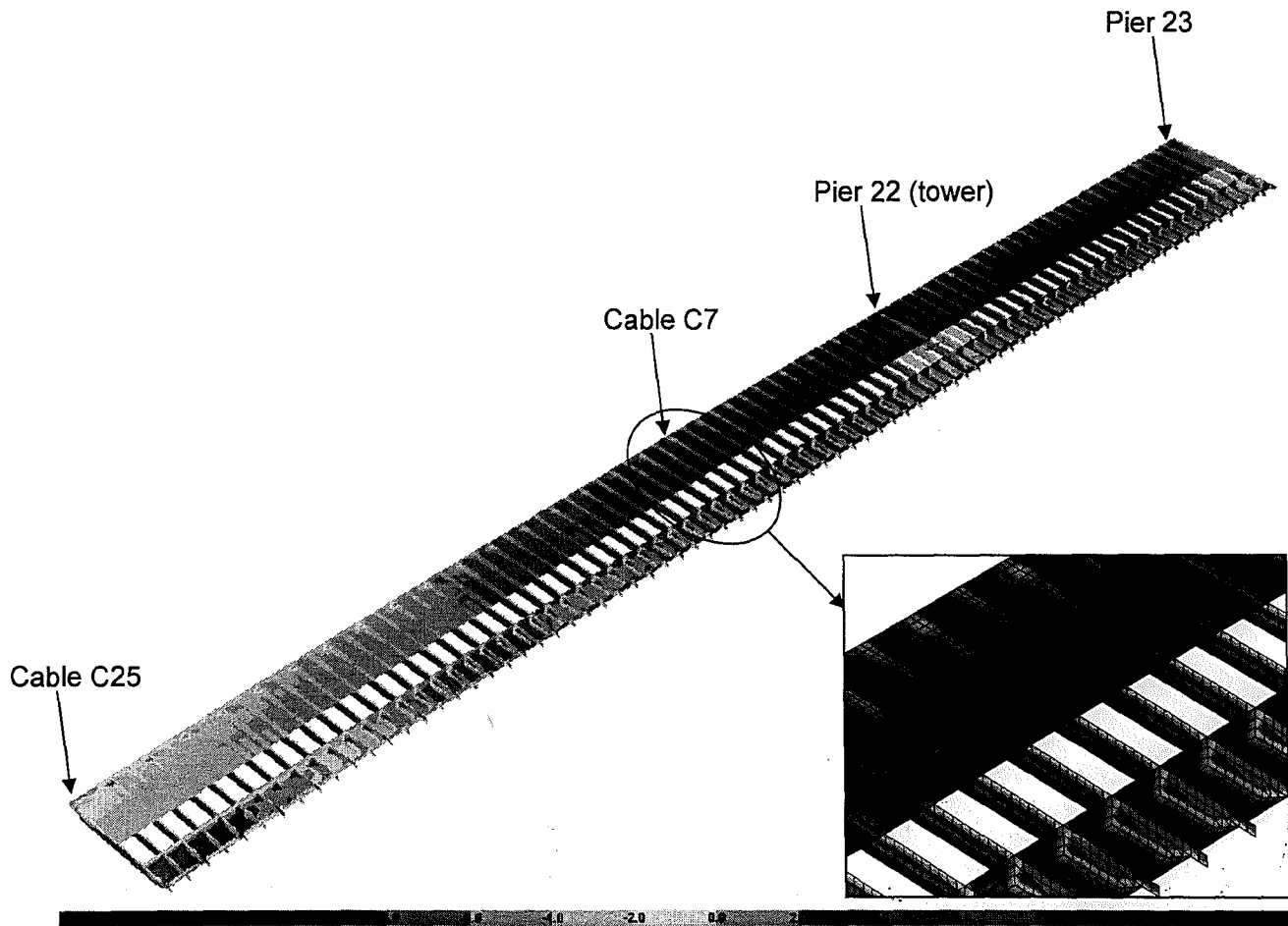
Figure 3.11 Stress contour of bridge deck in stay cable span under case LC#1 (Dead load + T1)
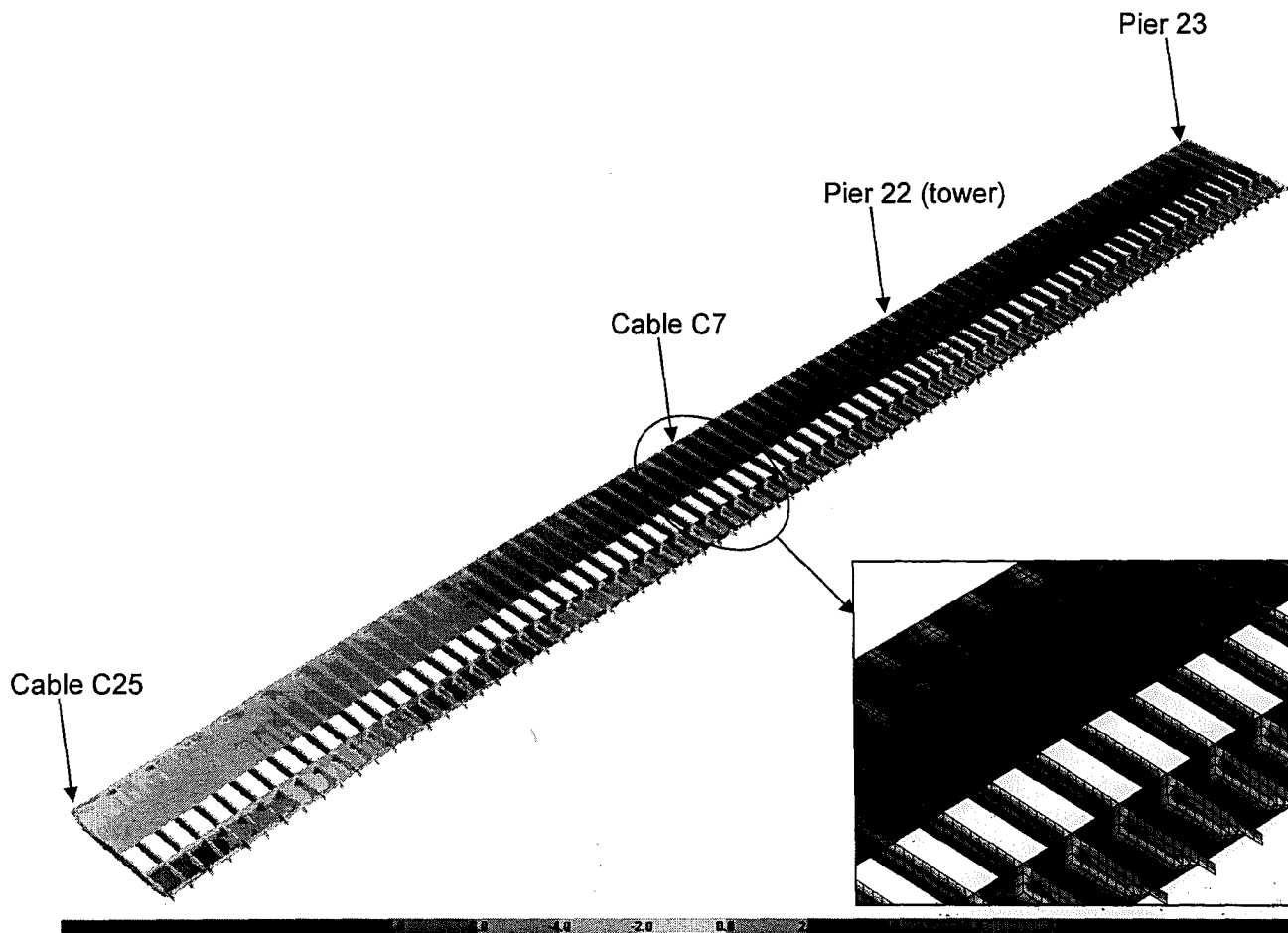
Figure 3.12 Stress contour of bridge deck in stay cable span under case LC#2 (Dead load +T2)

84
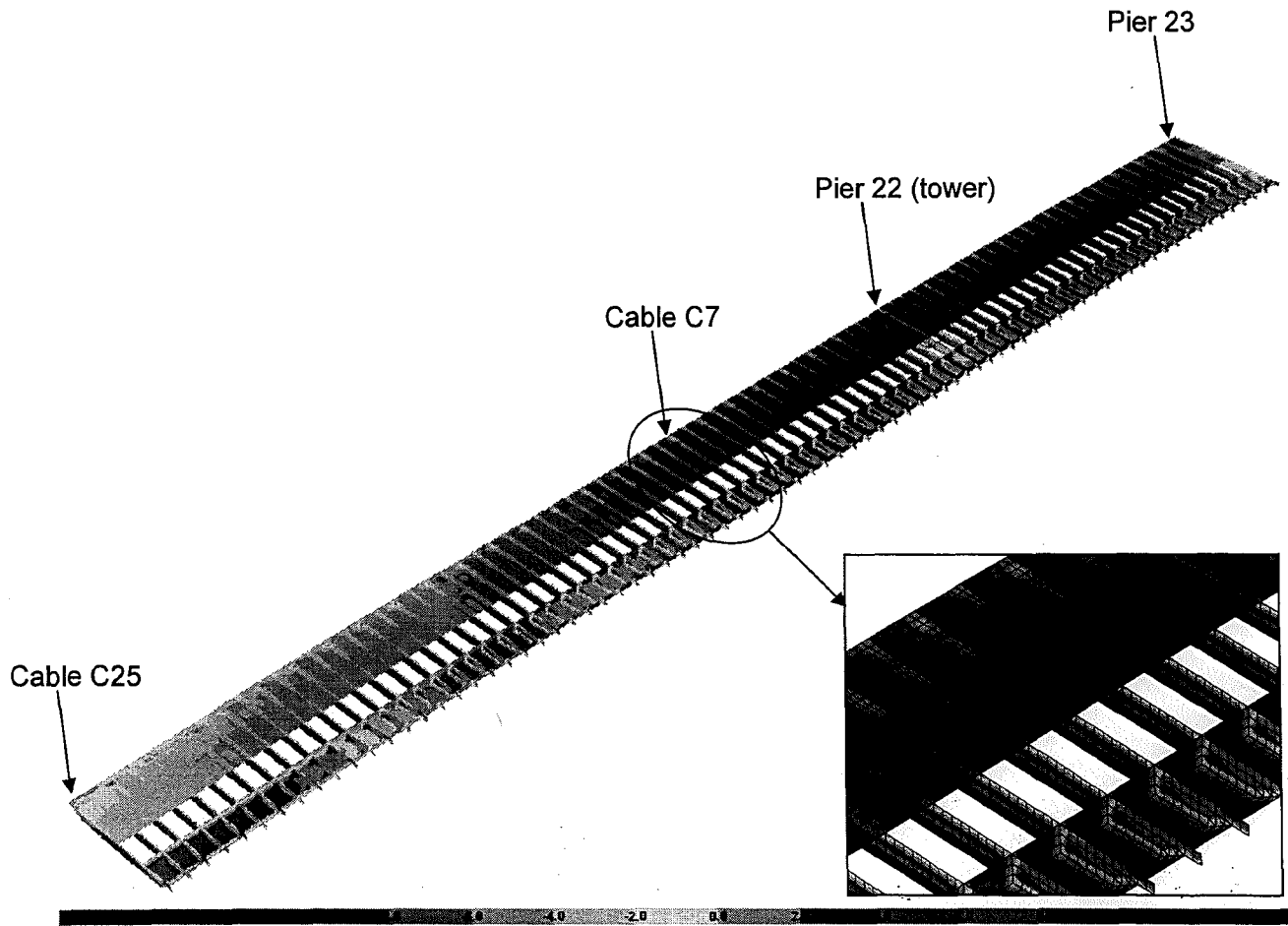
Figure 3.13 Stress contour of bridge deck in stay cable span under case LC#4 (Dead load +T4)

85
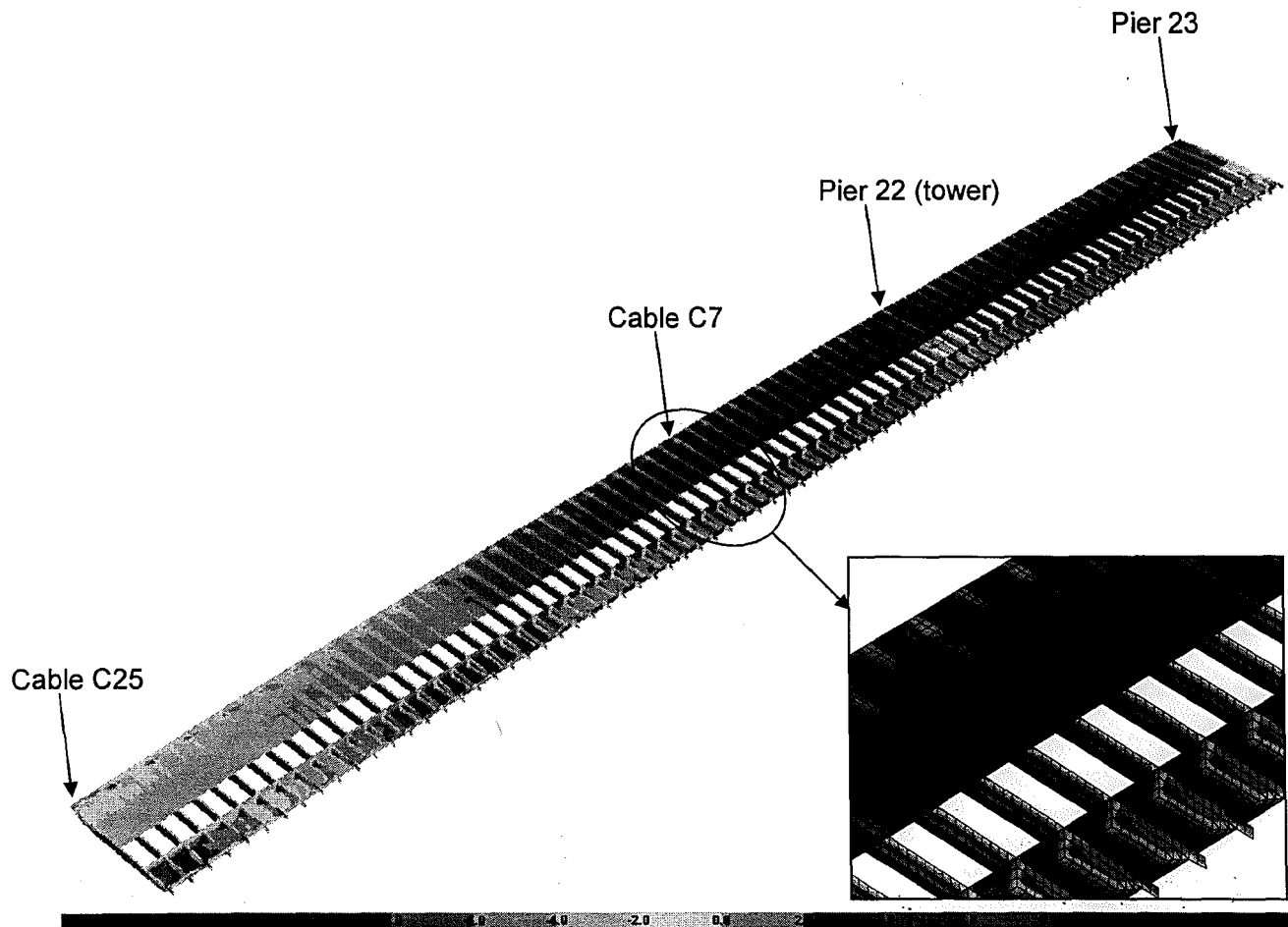
Figure 3.14 Stress contour of bridge deck in stay cable span under case LC#5 (Dead load +T5)
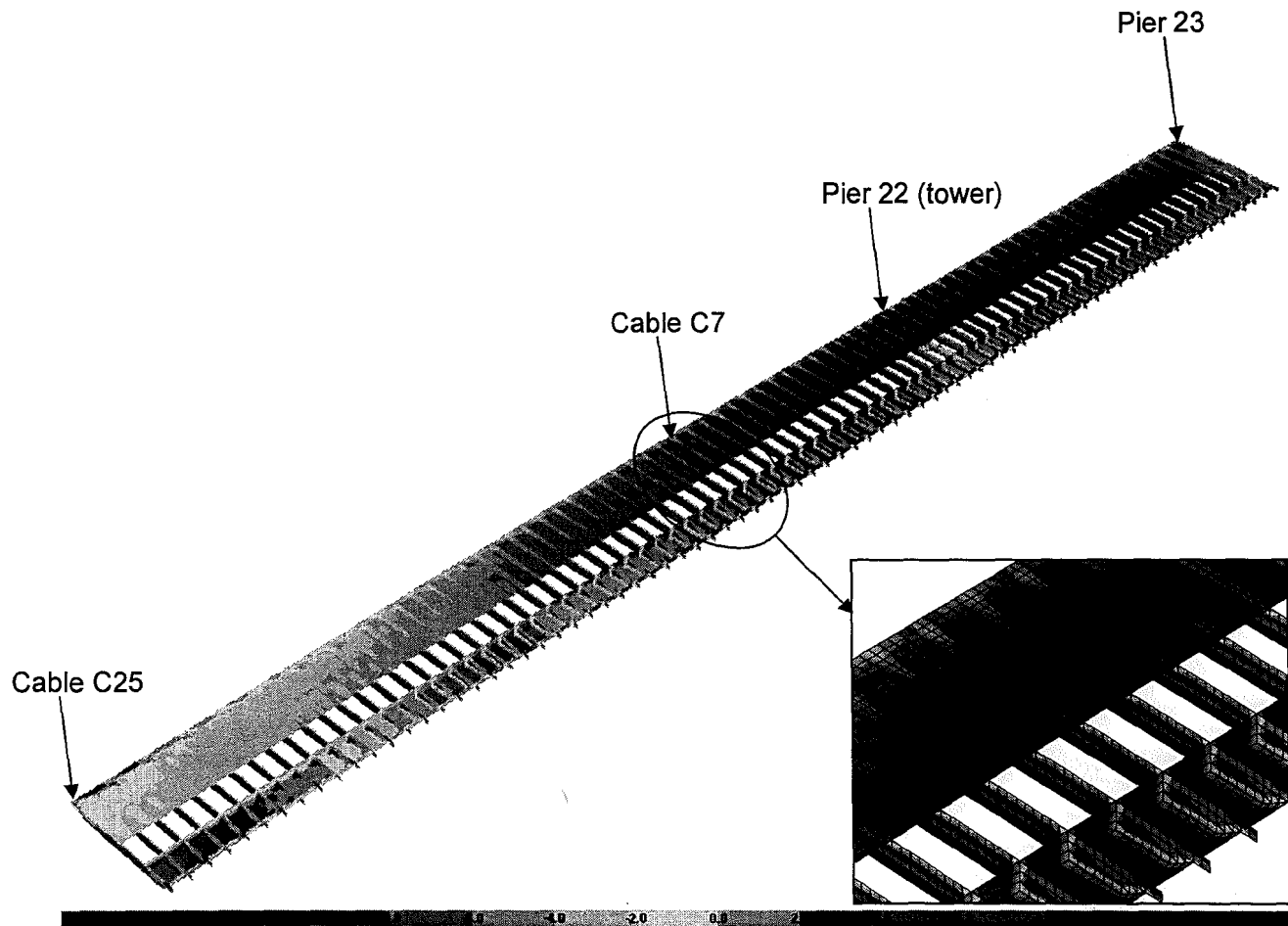
Figure 3.15 Stress contour of bridge deck in stay cable span under case LC#6 (Dead load +T6)

Chapter 4

Model for Dynamic Analysis

In this chapter, a three-dimensional finite element model for dynamic analysis is described in details. Compared with the finite element model described in Chapter 3, no shell element is used in this model which is computationally more efficient for dynamic analysis. This finite element model for dynamic analysis is validated with ambient vibration test data. The modal parameters of the ZBS cable-stayed bridge derived from this model are also presented here.

4.1 Description of Finite Element Model

In building the finite element model for dynamic analysis of the ZBS Bridge, a modeling approach suggested by Wilson and Gravelle (1993) was employed. Similar approach has also been used by a number of researchers (e.g., Dyke et al. 2003; Chang et al 2001). This comprises introducing a single central spine of linear elastic beam elements that has the actual bending and torsional stiffness of the deck. These stiffnesses were evaluated by establishing an equivalent cross section and the contribution of the prestressing steel tendons were considered in the model. The cross section of the deck is not uniform along the bridge which was taken into account while setting up the deck spine elements.

4.1.1 Overview of the dynamic model

The three-dimensional finite element model of the ZBS Cable-stayed Bridge for dynamic analysis is developed using *SAP2000 version 10.0.0*, as shown in Figure 4.1. This wire frame based finite element model has a total of 873 nodes and 969 frame elements, among which 150 nodes and 149 frame elements are used for the deck (spine) and 92 nodes, 88 frame elements for the tower and 121 nodes and 116 frame elements for the bridge piers. The stay cables are modeled using 204 nodes and 102 frame elements, 143 nodes. Additionally, 112 frame elements are employed to model the rigid links on the bridge tower, while 552 nodes and 402 frame elements are used for the rigid links on the bridge deck.

4.1.2 Mass Distribution

Inclusion of the masses in dynamic analysis model is essential to realistic analysis of the dynamic response of the cable-stayed bridge to lateral loads such as earthquake loading. When calculating the masses of the bridge deck, contributions from the concrete deck, railings, transmission pipes, pavements, are considered. The details and layout of these components can be found in Section 3.1.1. For example, the individual mass components for a typical deck spine node are listed in Table 4.1.

In this finite element model, the bridge deck is modeled as a massless central spine. The actual masses of the deck and additional loads are then assigned as additional lumped masses which are connected to the spine by rigid links, as shown in Figure 4.2. The deck is represented as two lumped masses, each having a mass equal to half of the total mass of the deck. As seen in Figure 4.2, rigid links are also employed to

connect cables to the deck. The use of rigid links ensures that the length and inclination angle of the cables in the model conform to the actual configuration.

The masses of the tower and stay cables are assigned to the frame elements as the self weight. The material densities of the primary structural members are listed in Table 4.2. Also, mass distribution for the deck is summarized in Table 4.3.

As illustrated in Figure 4.3, the spine is located at the shear center of the cross section in Pier 22 (tower). The mass center is determined from the masses of concrete deck, rails, transmission pipes, pavements, the details of which were described in Section 3.1.1. The centerline of the spine is set to go through the shear center, which is indicated in Figure 4.3.

4.1.3 Mass Moment of Inertia

The mass moment of inertia induced by the lumped masses is different than the actual one of the deck. The differences need to be considered to achieve the correct value. The mass moment of inertia of the lumped masses with respect to the j_{th} axis (either the X, Y, or Z axis), I_j, is calculated using the following expression,

$$I_j = 2M_l r^2$$

(4.1)

where M_l is the mass of each lumped mass, and r is the perpendicular distance from the mass to each axis. The actual mass moment of inertia of the deck with respect to the j_{th} axis, I_{mj}, is calculated using the equation below,

$$I_{mj} = \sum_{i=1}^{n}(I_{mi} + m_i r_i^2)$$

(4.2)

where I_{mj} is the mass moment of inertia of each of the component of the deck with

90

respect to its own centroidal axis, m_i is the mass of each component, and r_i is the perpendicular distance between the cancroids of each component and the j_{th} axis. Thus, the corrected mass moment of inertia of the section becomes

$$\Delta_j = I_{mj} - I_j \tag{4.3}$$

The values of this parameter about each axis for section of the deck are listed in Table 4.3. Negative values indicate that the contribution of the lumped masses to the mass moment of inertia of the section is larger than the mass moment of inertia of the actual section.

4.1.4 Support Condition and Constraints

Boundary conditions at the base of Pier #20, #21, #22 (tower), #23, #24 and #25 are specified such that their motion are restricted in all directions, i.e., they are modeled as fixed support.

When performing modal analysis, the constraints for this dynamic model are the same as those specified in the static analysis model (see Section 3.3.4). In seismic analysis, a link element as shown in Figure 4.4 is utilized to simulate the true support conditions of the bearings between the bridge deck and the cap of the piers. This kind of friction-pendulum isolator is one of the nonlinear two-node link elements in *SAP2000*. This element can be used to model gap and friction behavior between contacting surfaces. The friction forces and pendulum forces are directly proportional to the compressive axial force in the element. Therefore, the constraints at Pier #21, #23, #24, #25 for this model were replaced with nonlinear friction isolators in the form of link elements when doing time history analysis.

91

4.1.5 Equivalent Modulus for Cables

Equivalent elastic modules are employed for the stay cables in this finite element model for dynamic analysis. Details can be found in Section 3.3.5.

4.2 Modal Parameters

4.2.1 Modal Parameters of FE Model

Table 4.4 lists the modal frequencies of the ZBS cable-stayed bridge derived from the finite element model. Figure 4.5 shows the mode shapes of the first four dominant modes of the ZBS cable-stayed bridge from the finite element model.

4.2.2 Model Validation with Experimental Data

As mentioned in Section 3.3.6, a series of ambient vibration tests have been conducted on the ZBS cable-stayed bridge to measure its ambient vibration dynamic response from March 20th to April 10th, 2001. The instrumentation and data acquisition, measurement station arrangements and test data are presented in Section 3.3.6 (2). The modal frequencies and associated mode shapes of four dominant vibrational modes of the ZBS cable-stayed bridge were identified from the ambient vibration test data.

The experimentally identified modal frequencies of the ZBS Bridge have been listed in Table 3.5. The modal frequencies of the first vertical, lateral, longitudinal and torsional modes of the bridge are 0.406 Hz, 0.564 Hz, 0.742 Hz and 0.957 Hz, respectively.

Table 4.6 lists the modal frequencies of the ZBS Bridge calculated from the finite element model in comparison with those from the ambient vibration test. The error between the finite element analysis results and experimental results is illustrated in Figure 4.6 and also the data are listed in Table 4.6. It is clearly seen that the finite element model gives a reasonably good estimate of the modal frequencies for the vertical, lateral, longitudinal and rotational mode. The error is 1% for the first vertical mode between the prediction of finite element model and the field test data. As a result, the finite element model based on SAP2000 is considered to provide relatively accurate results for dynamic analysis.

4.3 Conclusion

Regarding the finite element model discussed in this chapter, the following conclusions can be made,

i)   The natural frequencies of the ZBS cable-stayed bridge as determined from the current finite element model are in good agreement with those derived from the ambient vibration test data. This three-dimensional finite element spine model for dynamic model is thus considered to be validated by the field test data. It is thus believed that the SAP2000 program is capable of modeling the dynamic response characteristics of cable stayed bridges.

ii) Compared with the frequency values from the test data, the error in the modal frequencies calculated from the finite element spine model are 1%, 9%, 12% and 10% for the four modes under consideration. It is seen that

93

the error increases with the increase in modal frequency, i.e., higher modes have larger error.

iii) In comparison with the static analysis model discussed in Chapter 3, the spine model given in this chapter is computationally more efficient while appears to achieve a similar level of accuracy in terms of predicting the dynamic response characteristics of the bridge. This is because the total number of degrees of freedom of the spine model is much smaller than that of the static analysis model which involves shell element for bridge deck. Naturally, the computation time for dynamic simulation by the spine model is much less than the static analysis model. The average computation time for modal analysis of the ZBS cable-stayed bridge between the spine model and the static analysis model is 1:60. The spine model is also advantageous since much less internal memory space is required of computer, while being able to achieve accurate results for dynamic response simulation. The error in modal frequencies predicted by the static analysis model and the spine model is illustrated in Figure 4.7.

Table 4.1 Mass components for a typical deck spine node

No.	Component	Mass (Kg)
1	Self Weight of Deck	1.23E+05
2	Ash Transimission Pipes	6.70E+03
3	Water Transmission Pipes	4.57E+03
4	Pavement	2.35E+04
5	Rails	2.04E+03
6	Transverse web	3.98E+04
Sum	-	2.00E+05

Table 4.2 Material densities of primary structural members

Materials	Density (Kg/m^3)	Structural Members
Concrete	2500	Tower, decks, piers
Cables (Steel)	7849	Stayed cables

Table 4.3 Lumped mass and mass moment of inertia distribution for deck

No.		Area (cm^2)	Length (m)	Lumped Mass (Kg)	Correction for mass moment of inertia		
					Δ_X (Kg·m^2)	Δ_Y (Kg·m^2)	Δ_Z (Kg·m^2)
1	Pier 20	155305	1.475	38748	1.230E+05	1.117E+05	1.124E+04
2		155305	2.950	77497	-1.778E+05	2.038E+05	-3.816E+05
3		155305	2.950	77497	-1.778E+05	2.038E+05	-3.816E+05
4		155305	2.950	77497	-1.778E+05	2.038E+05	-3.816E+05
5		155305	2.950	77497	-1.778E+05	2.038E+05	-3.816E+05
6		155305	2.950	77497	-1.778E+05	2.038E+05	-3.816E+05
7		155305	2.950	77497	-1.778E+05	2.038E+05	-3.816E+05
8		155305	2.950	77497	-1.778E+05	2.038E+05	-3.816E+05
9		155305	2.950	77497	-1.778E+05	2.038E+05	-3.816E+05
10		155305	2.950	77497	-1.778E+05	2.038E+05	-3.816E+05
11		163727	3.725	101778	-1.778E+05	2.038E+05	-3.816E+05
12		172149	4.500	127690	-4.196E+04	5.759E+05	-6.178E+05
13		188993	4.500	137165	9.392E+04	9.481E+05	-8.540E+05
14		205837	4.000	130347	2.298E+05	1.320E+06	-1.090E+06
15		218938	3.500	119785	3.355E+05	1.610E+06	-1.274E+06
16		232038	3.500	125516	4.412E+05	1.899E+06	-1.458E+06
17		245139	3.500	131248	5.469E+05	2.189E+06	-1.642E+06
18		258240	3.500	136980	6.525E+05	2.478E+06	-1.825E+06
19		271341	3.500	142711	7.582E+05	2.768E+06	-2.009E+06
20		284442	3.500	148443	8.639E+05	3.057E+06	-2.193E+06

No.		Area (cm²)	Length (m)	Lumped Mass (Kg)	Correction for mass moment of inertia		
					Δ_X (Kg·m²)	Δ_Y (Kg·m²)	Δ_Z (Kg·m²)
21		297542	3.250	143162	9.696E+05	3.347E+06	-2.376E+06
22		308772	3.500	159087	1.060E+06	3.595E+06	-2.534E+06
23	Pier 21	323744	4.000	189300	1.181E+06	3.926E+06	-2.744E+06
24		308772	3.500	159087	1.060E+06	3.595E+06	-2.534E+06
25		297542	3.250	143162	9.696E+05	3.347E+06	-2.376E+06
26		284442	3.500	148443	8.639E+05	3.057E+06	-2.193E+06
27		271341	3.500	142711	7.582E+05	2.768E+06	-2.009E+06
28		258240	3.500	136980	6.525E+05	2.478E+06	-1.825E+06
29		245139	3.500	131248	5.469E+05	2.189E+06	-1.642E+06
30		232038	3.500	125516	4.412E+05	1.899E+06	-1.458E+06
31		218938	3.500	119785	3.355E+05	1.610E+06	-1.274E+06
32		205837	4.000	130347	2.298E+05	1.320E+06	-1.090E+06
33		188993	4.500	137165	9.392E+04	9.481E+05	-8.540E+05
34		172149	4.500	127690	-4.196E+04	5.759E+05	-6.178E+05
35		155305	4.000	105081	-1.778E+05	2.038E+05	-3.816E+05
36		139374	2.500	60697	9.693E+05	1.648E+05	8.044E+05
37		132546	1.750	40994	1.543E+06	1.453E+05	1.397E+06
38	C25	123443	3.000	81793	2.116E+06	1.259E+05	1.990E+06
39		123443	4.000	109058	2.282E+06	1.523E+05	2.130E+06
40	C24	123443	4.000	109058	2.282E+06	1.523E+05	2.130E+06
41		123443	4.000	109058	2.282E+06	1.523E+05	2.130E+06
42	C23	123443	4.000	109058	2.282E+06	1.523E+05	2.130E+06
43		123443	4.000	109058	2.282E+06	1.523E+05	2.130E+06
44	C22	123443	4.000	109058	2.282E+06	1.523E+05	2.130E+06
45		123443	4.000	109058	2.282E+06	1.523E+05	2.130E+06
46	C21	123443	4.000	109058	2.282E+06	1.523E+05	2.130E+06
47		123443	4.000	109058	2.282E+06	1.523E+05	2.130E+06
48	C20	123443	4.000	109058	2.282E+06	1.523E+05	2.130E+06
49		123443	4.000	109058	2.282E+06	1.523E+05	2.130E+06
50	C19	123443	4.000	109058	2.282E+06	1.523E+05	2.130E+06
51		123443	4.000	109058	2.282E+06	1.523E+05	2.130E+06
52	C18	123443	4.000	109058	2.282E+06	1.523E+05	2.130E+06
53		123443	4.000	109058	2.282E+06	1.523E+05	2.130E+06
54	C17	123443	4.000	109058	2.282E+06	1.523E+05	2.130E+06
55		123443	4.000	109058	2.282E+06	1.523E+05	2.130E+06
56	C16	123443	4.000	109058	2.282E+06	1.523E+05	2.130E+06
57		123443	4.000	109058	2.282E+06	1.523E+05	2.130E+06
58	C15	123443	4.000	109058	2.282E+06	1.523E+05	2.130E+06
59		123443	4.000	109058	2.282E+06	1.523E+05	2.130E+06
60	C14	123443	4.000	119042	3.216E+06	1.885E+05	3.028E+06
61		123443	4.000	119042	3.216E+06	1.885E+05	3.028E+06

No.		Area (cm²)	Length (m)	Lumped Mass (Kg)	Correction for mass moment of inertia		
					Δ_X (Kg·m²)	Δ_Y (Kg·m²)	Δ_Z (Kg·m²)
62	C13	123443	4.000	119042	3.216E+06	1.885E+05	3.028E+06
63		123443	4.000	119042	3.216E+06	1.885E+05	3.028E+06
64	C12	123443	4.000	119042	3.216E+06	1.885E+05	3.028E+06
65		123443	4.000	119042	3.216E+06	1.885E+05	3.028E+06
66	C11	123443	4.000	119042	3.216E+06	1.885E+05	3.028E+06
67		123443	4.000	119042	3.216E+06	1.885E+05	3.028E+06
68	C10	123443	4.000	119042	3.216E+06	1.885E+05	3.028E+06
69		123443	4.000	119042	3.216E+06	1.885E+05	3.028E+06
70	C9	123443	4.000	119042	3.216E+06	1.885E+05	3.028E+06
71		123443	4.000	119042	3.216E+06	1.885E+05	3.028E+06
72	C8	123443	4.000	119042	3.216E+06	1.885E+05	3.028E+06
73		123443	4.000	119042	3.216E+06	1.885E+05	3.028E+06
74	C7	123443	4.000	119042	3.216E+06	1.885E+05	3.028E+06
75		123443	4.000	119042	3.216E+06	1.885E+05	3.028E+06
76	C6	123443	4.000	119042	3.216E+06	1.885E+05	3.028E+06
77		123443	4.000	119042	3.216E+06	1.885E+05	3.028E+06
78	C5	123443	4.000	119042	3.216E+06	1.885E+05	3.028E+06
79		123443	4.000	119042	3.216E+06	1.885E+05	3.028E+06
80	C4	123443	4.000	119042	3.216E+06	1.885E+05	3.028E+06
81		123443	4.000	119042	3.216E+06	1.885E+05	3.028E+06
82	C3	123443	4.000	119042	3.216E+06	1.885E+05	3.028E+06
83		123443	4.000	119042	3.216E+06	1.885E+05	3.028E+06
84	C2	123443	4.000	119042	3.216E+06	1.885E+05	3.028E+06
85		123443	4.000	119042	3.216E+06	1.885E+05	3.028E+06
86	C1	123443	3.750	111601	3.116E+06	1.797E+05	2.936E+06
87		123443	3.500	104161	3.016E+06	1.708E+05	2.846E+06
88		123443	3.500	104161	3.016E+06	1.708E+05	2.846E+06
89		123443	3.500	104161	3.016E+06	1.708E+05	2.846E+06
90	Pier 22	123443	3.500	104161	3.016E+06	1.708E+05	2.846E+06
91		123443	3.500	104161	3.016E+06	1.708E+05	2.846E+06
92		123443	3.500	104161	3.016E+06	1.708E+05	2.846E+06
93		123443	3.500	104161	3.016E+06	1.708E+05	2.846E+06
94	C1'	123443	3.750	111601	3.116E+06	1.797E+05	2.936E+06
95		123443	4.000	119042	3.216E+06	1.885E+05	3.028E+06
96	C2'	123443	4.000	119042	3.216E+06	1.885E+05	3.028E+06
97		123443	4.000	119042	3.216E+06	1.885E+05	3.028E+06
98	C3'	123443	4.000	119042	3.216E+06	1.885E+05	3.028E+06
99		123443	4.000	119042	3.216E+06	1.885E+05	3.028E+06
100	C4'	123443	4.000	119042	3.216E+06	1.885E+05	3.028E+06
101		123443	4.000	119042	3.216E+06	1.885E+05	3.028E+06
102	C5'	123443	4.000	119042	3.216E+06	1.885E+05	3.028E+06

No.		Area (cm²)	Length (m)	Lumped Mass (Kg)	Correction for mass moment of inertia		
					Δ_X (Kg·m²)	Δ_Y (Kg·m²)	Δ_Z (Kg·m²)
103		123443	4.000	119042	3.216E+06	1.885E+05	3.028E+06
104	C6'	123443	4.000	119042	3.216E+06	1.885E+05	3.028E+06
105		123443	4.000	119042	3.216E+06	1.885E+05	3.028E+06
106	C7'	123443	4.000	119042	3.216E+06	1.885E+05	3.028E+06
107		123443	4.000	119042	3.216E+06	1.885E+05	3.028E+06
108	C8'	123443	4.000	119042	3.216E+06	1.885E+05	3.028E+06
109		123443	4.000	119042	3.216E+06	1.885E+05	3.028E+06
110	C9'	123443	4.000	119042	3.216E+06	1.885E+05	3.028E+06
111		123443	4.000	119042	3.216E+06	1.885E+05	3.028E+06
112	C10'	123443	4.000	119042	3.216E+06	1.885E+05	3.028E+06
113		123443	4.000	119042	3.216E+06	1.885E+05	3.028E+06
114	C11'	123443	4.000	119042	3.216E+06	1.885E+05	3.028E+06
115		123443	4.000	119042	3.216E+06	1.885E+05	3.028E+06
116	Pier 23	123443	4.000	119042	3.216E+06	1.885E+05	3.028E+06
117		123443	4.000	119042	3.216E+06	1.885E+05	3.028E+06
118	C13'	123443	4.000	119042	3.216E+06	1.885E+05	3.028E+06
119		123443	4.000	119042	3.216E+06	1.885E+05	3.028E+06
120	C14'	123443	4.000	119042	3.216E+06	1.885E+05	3.028E+06
121		123443	4.000	119042	3.216E+06	1.885E+05	3.028E+06
122	C15'	123443	4.000	119042	3.216E+06	1.885E+05	3.028E+06
123		123443	4.000	119042	3.216E+06	1.885E+05	3.028E+06
124	C16'	123443	4.000	119042	3.216E+06	1.885E+05	3.028E+06
125		123443	4.000	119042	3.216E+06	1.885E+05	3.028E+06
126	C17'	123443	4.000	119042	3.216E+06	1.885E+05	3.028E+06
127		123443	4.000	119042	3.216E+06	1.885E+05	3.028E+06
128	C18'	123443	4.000	119042	3.216E+06	1.885E+05	3.028E+06
129		123443	4.000	119042	3.216E+06	1.885E+05	3.028E+06
130	C19'	123443	4.000	119042	3.216E+06	1.885E+05	3.028E+06
131		123443	4.000	119042	3.216E+06	1.885E+05	3.028E+06
132	C20'	143723	4.000	129181	2.320E+06	2.453E+05	2.075E+06
133		164002	4.000	139321	1.424E+06	3.021E+05	1.121E+06
134	C21'	164002	4.000	139321	1.424E+06	3.021E+05	1.121E+06
135		164002	4.000	139321	1.424E+06	3.021E+05	1.121E+06
136	C22'	164002	3.500	121906	1.448E+06	2.701E+05	1.178E+06
137	Pier 24	164002	3.000	118075	3.432E+05	3.031E+05	4.004E+04
138	C24'	164002	3.000	118075	3.432E+05	3.031E+05	4.004E+04
139	C25'	164002	3.000	118075	3.432E+05	3.031E+05	4.004E+04
140		164002	3.525	138738	1.202E+05	3.481E+05	-2.280E+05
141		164002	4.050	117872	3.732E+05	2.535E+05	1.198E+05
142		164002	4.050	117872	3.732E+05	2.535E+05	1.198E+05
143		164002	4.050	117872	3.732E+05	2.535E+05	1.198E+05

No.		Area (cm^2)	Length (m)	Lumped Mass (Kg)	Correction for mass moment of inertia		
					Δ_X (Kg·m^2)	Δ_Y (Kg·m^2)	Δ_Z (Kg·m^2)
144		164002	4.050	117872	3.732E+05	2.535E+05	1.198E+05
145		164002	4.050	117872	3.732E+05	2.535E+05	1.198E+05
146		164002	4.050	117872	3.732E+05	2.535E+05	1.198E+05
147		164002	4.050	117872	3.732E+05	2.535E+05	1.198E+05
148		164002	4.050	117872	3.732E+05	2.535E+05	1.198E+05
149		164002	4.050	117872	3.732E+05	2.535E+05	1.198E+05
150	Pier 25	164002	2.025	58936	6.234E+05	1.416E+05	4.818E+05

Table 4.4 Frequencies output from FE model

Mode #	Period (sec)	Frequency (Hz)	Mode Shape
1	2.482	0.403	vertical
2	1.932	0.518	lateral
3	1.509	0.663	vertical
4	1.320	0.758	lateral
5	1.190	0.840	longitudinal
6	1.050	0.952	local
7	1.019	0.982	vertical
8	0.942	1.061	rotational
9	0.889	1.125	local
10	0.671	1.490	vertical
11	0.593	1.687	vertical
12	0.564	1.774	vertical
13	0.437	2.287	lateral
14	0.338	2.955	vertical
15	0.303	3.297	tower long.+vertical
16	0.223	4.476	tower vertical+vertical

Table 4.5 Ambient test results

	Mode	Frequency (Hz)	Damping ratio (%)
1	First Vertical Mode	0.406	0.782
2	First Lateral Mode	0.564	0.501
3	First Longitudinal Mode	0.742	0.431
4	First Rotational Mode	0.957	0.331

Table 4.6 Frequencies results summary

	Mode	Frequency (Hz)			Period (sec)		
		FEM	Test	Error	FEM	Test	Error
1	First Vertical Mode	0.403	0.406	1%	2.482	2.463	1%
2	First Lateral Mode	0.518	0.564	8%	1.932	1.773	9%
3	First Longitudinal Mode	0.840	0.742	13%	1.190	1.348	12%
4	First Rotational Mode	1.061	0.957	11%	0.942	1.045	10%

| 74500 | 258000 | 102000 | 83000 | 49500 |

Zhao Bao Shan

C0
C1
C1'
C25
C25'

Jin Ji Shan

20　21　22　23　24　25

Unit: mm
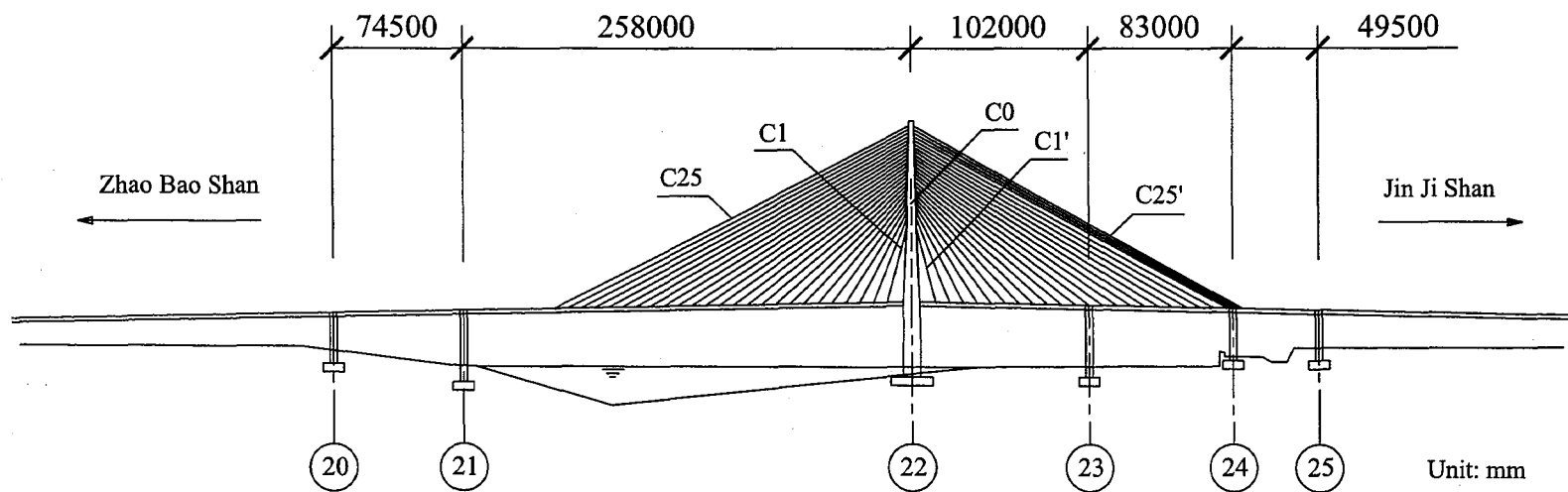
(a) Overview of the ZBS Bridge (Figure 4.1 continued in the next page)
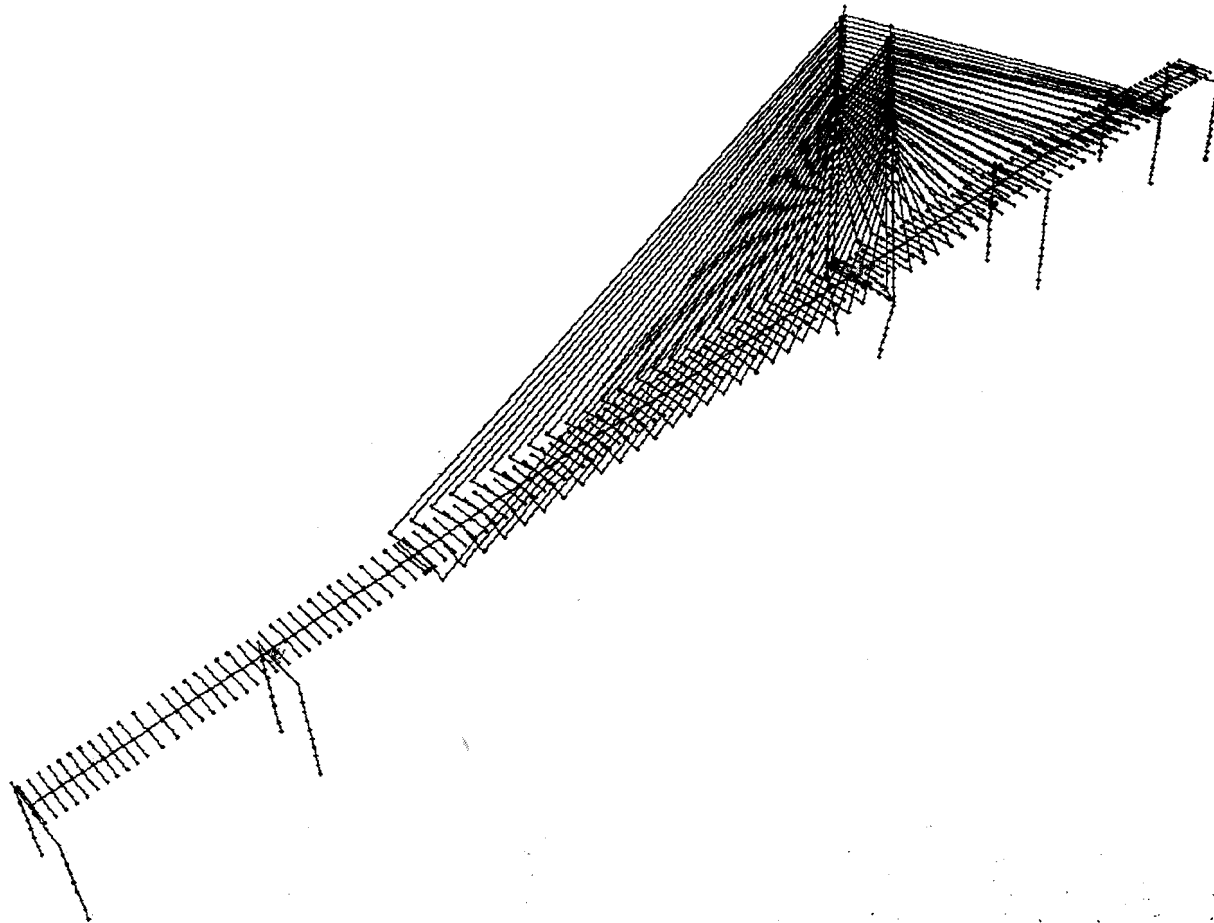
(b) Intruded view of 3-D FEM model

Figure 4.1 Global view of the bridge model
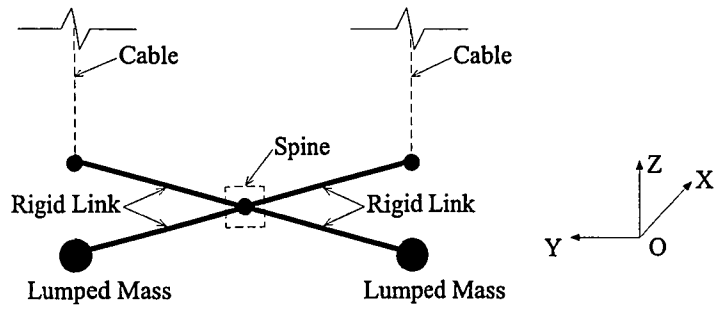
Figure 4.2 Finite element modeling of the cross section of the deck
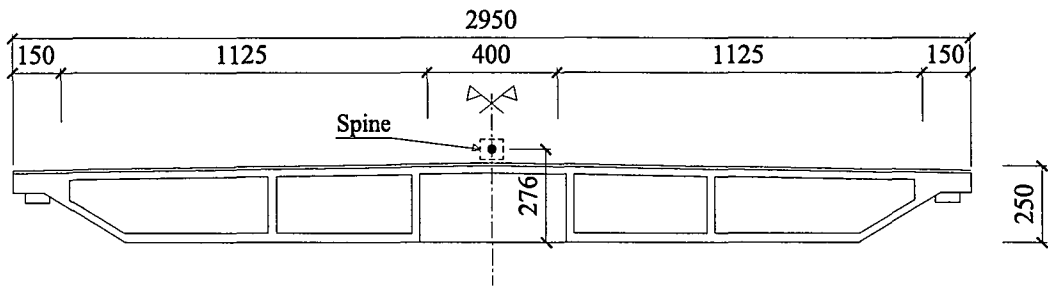
Figure 4.3 Location of spine in Pier 22 (tower)
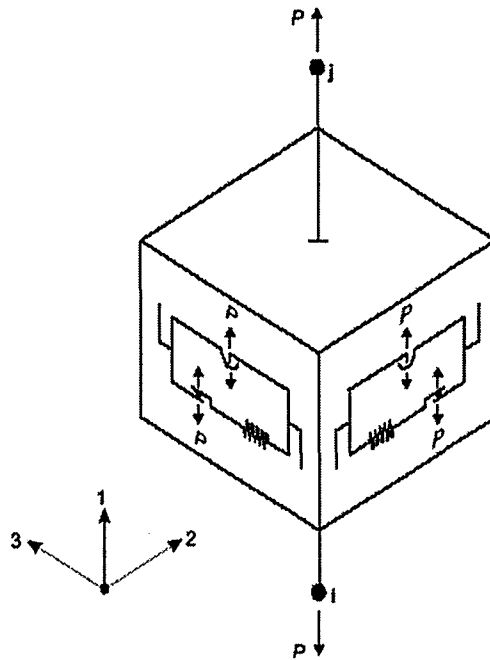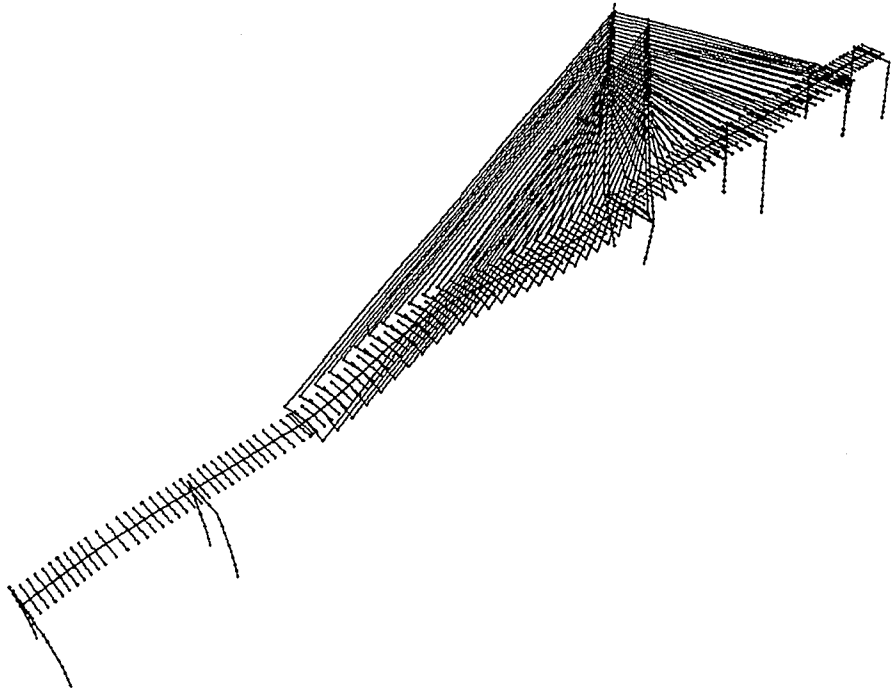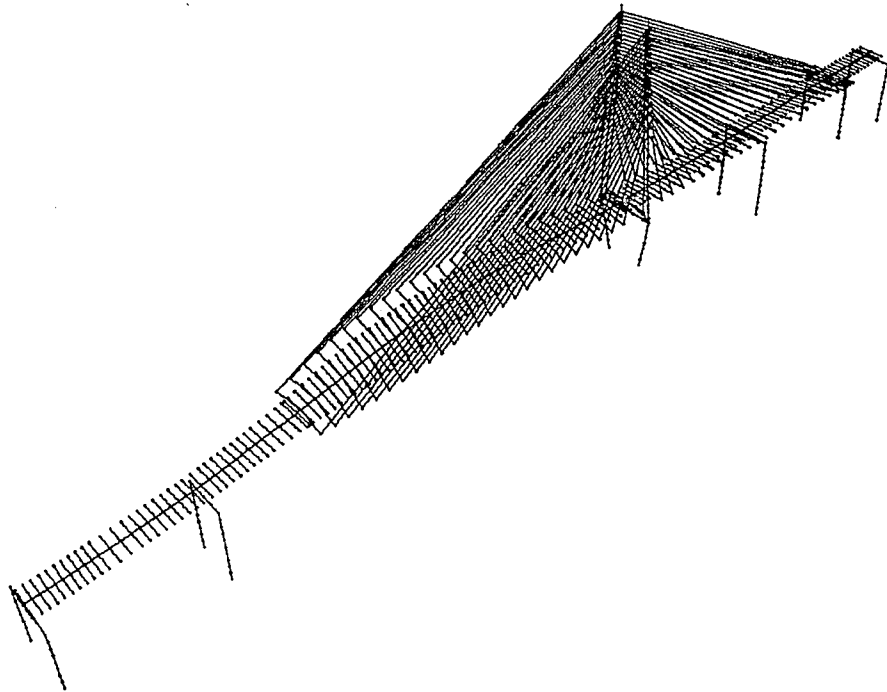

Figure 4.4 Link element (Friction-Pendulum Isolator)

103
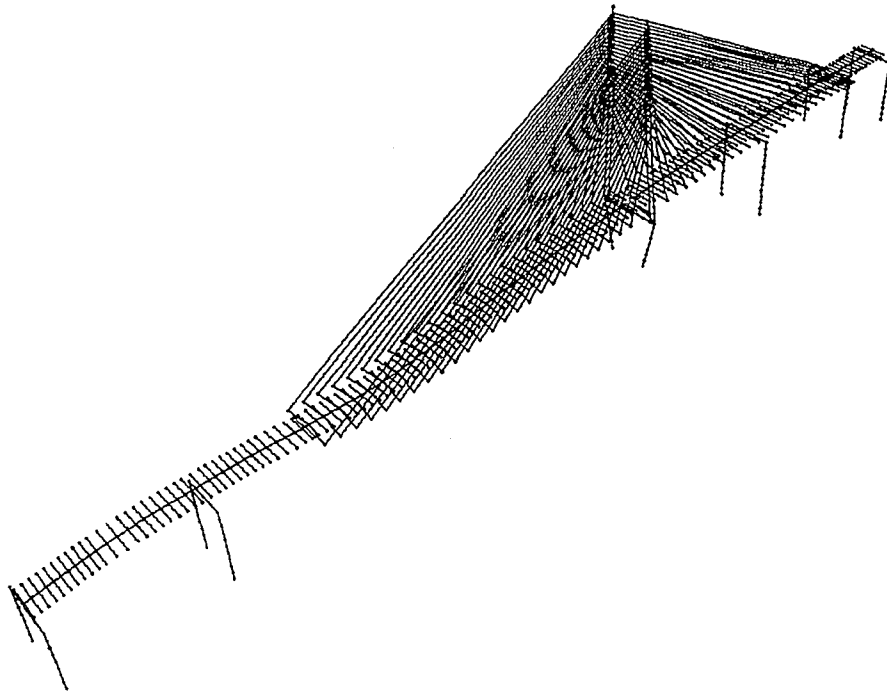
(a) 1st vertical mode (Mode 1 period 2.482 s)
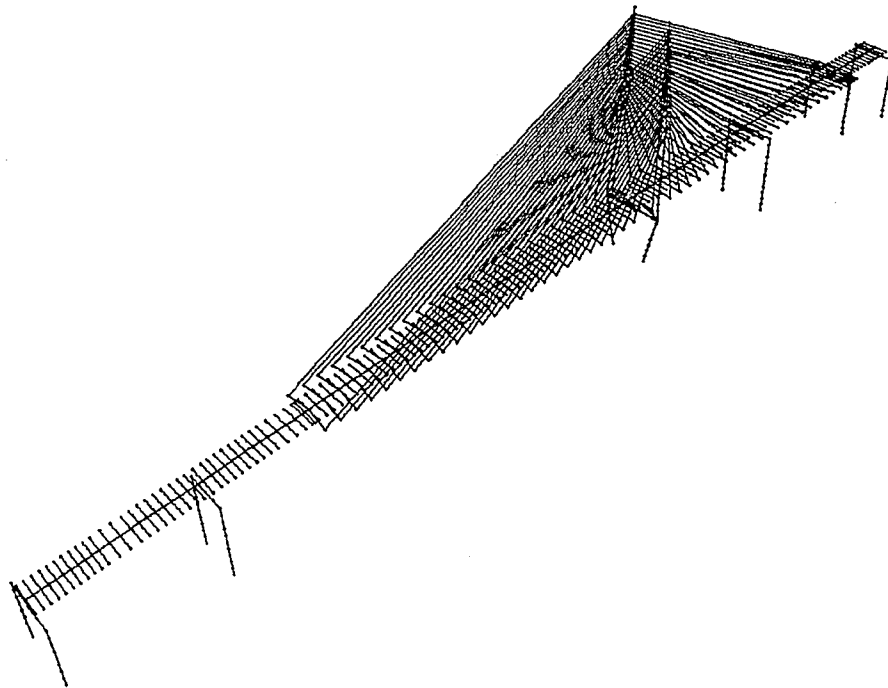
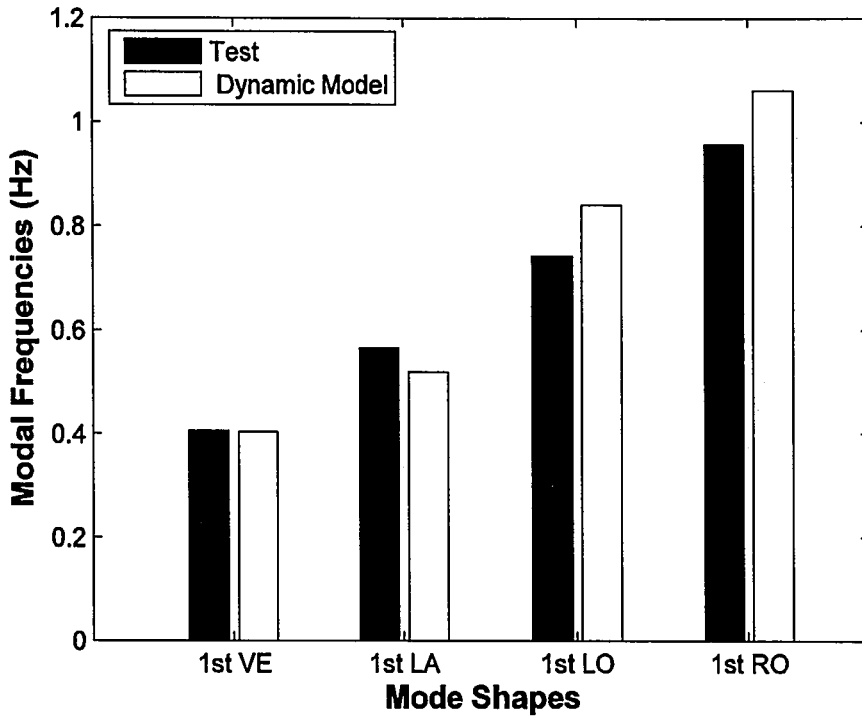(b) 1st lateral mode (Mode 2 Period 1.932 s) (**Figure 4.5** continued)

104
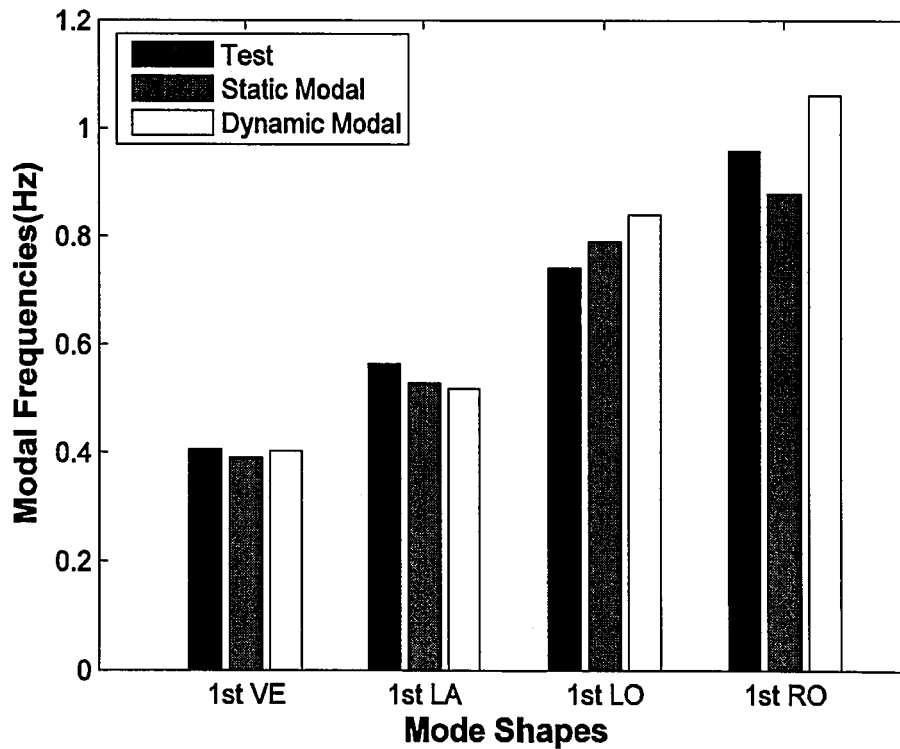
(c) 1st longitudinal mode (Mode 5 Period 1.190 s)

(c) 1st longitudinal mode (Mode 5 Period 1.190 s)

(d) 1st torsional mode (Mode 8 Period 0.942 s)

Figure 4.5 First four dominant mode shapes from FEM

Figure 4.6 Modal frequencies comparison-1

(VE=vertical mode, LA=lateral mode, LO=longitudinal mode, RO=rotational mode)

Figure 4.7 Modal frequencies comparison-2

(VE=vertical mode, LA=lateral mode, LO=longitudinal mode, RO=rotational mode)

106

Chapter 5

Seismic Response Analysis

In this chapter, the seismic condition of the ZBS Bridge is first presented, followed by a description of the six earthquake ground motion records selected for seismic time history analysis. The results of a nonlinear time history analysis of the ZBS Bridge under maximum considered earthquakes (3% probability of exceedance within 50 years) are discussed lastly.

5.1 Seismic Condition of the ZBS Bridge Site

Earthquake recording in the area of the ZBS bridge site can be found in the local written history as early as 288 A.D. In the 1970s, a regional seismic instrumentation network was established in the local area, which is able to monitor earthquakes with magnitude greater than M2.5

When evaluating the seismological activity of the bridge site, a study region with a 150-kM radius centered around the bridge site generally needs to be considered (Zhejiang Provincial Engineering Seismology Research Institute 2005). This study region – part of the Lower Yangtze River - South Yellow Sea seismic fault zone has relatively weak seismic activities. Historical record reveals a total of twenty-nine earthquakes with magnitude over M4.7 in the study region and the maximum-recorded earthquake is a M6.1 offshore earthquake in 1996 with its epicenter located

107

outside the estuary of Yangtze River. The earliest reported earthquake occurred in February 288 in an area that is approximately 100 km west of the bridge site. However, earthquake-induced damages were not reported until 872.

Within a distance of 20 km from the bridge site, no earthquake with a magnitude over M2.0 has even been recorded since the 1970s. However, between 1993 and 1994, two earthquakes with magnitudes of M3.9 and M4.7 respectively occurred near the Jiaokou reservoir located about 40 km away from the bridge site. The closest historical earthquake to the bridge site was the Zhenhai Earthquake with an estimated magnitude of M5.5 that occurred in 1523, as shown in Figure 5.1. For this M5.5 earthquake, the maximum seismic intensity level near epicenter was reported to be VII according to the local written history. The epicenter of this historical earthquake is less than 6 km from the bridge site. In 1971, a M4.8 earthquake occurred in Daqushan Island, located about 80 km from the bridge site. Within a distance of 280 km, the largest modern earthquake is the one with a magnitude of M6.1 which occurred in November 1996 outside the estuary of Yangtze River.

There are two nearby earthquake faults that my impact the bridge site. The closest fault is the north-east running Ningbo-Changtiaozui fault (indicated as F5 in Figure 5.2) and the other fault is the north-north-east directional Baotong-Xiaogang fault (F6) which is a sub-fault of the Zhenhai-Wenzhou fault. The Ningbo-Changtiaozui fault runs through the ZBS Bridge at its south side approach span. Within a distance of 30 km, other major active faults with a length over 10 km include: Ningbo-Yuyao fault (F7), Chailou-Xinlu Reservoir fault (F3), and Changshadai-Jintang fault (F4). Although relatively weak rupture activities were associated with these adjacent faults

in the recent 100 years, it is likely that M6.0 earthquakes with shallow hypocenter (average depth to hypocenter estimated to be 12 km) based on the tectonic history and seismological survey.

As for near-field earthquakes, there are three recorded earthquakes with a magnitude over M4.0. Near-field earthquake refers to that with an epicenter distance less than 25 km from the site under consideration. The largest one is the aforementioned M5.5 Zhenhai earthquake that occurred on August 24, 1523. Based on the historical earthquake information and seismological survey, the bridge site has relatively active near-field earthquakes, where >M5.5 earthquakes are likely to occur in the future. The maximum seismic intensity level produced by future earthquakes is estimated to be VII in the bridge site.

5.2 Earthquake Ground Motion

The ZBS Bridge is located in a moderate seismic area. Earthquakes with a magnitude M6 are likely to occur. According to the Chinese seismic design code (China Ministry of Construction, 2001), the design seismic intensity level for this area is designated as Degree VI. It is worth noting that in 2002, the design seismic design intensity level in the local area of the ZBS bridge site was adjusted from Degree VI to VII. Since its construction was completed in 2001, the ZBS Bridge was designed for a seismic intensity level lower than that specified in the current seismic design code. In order to assure the safety of the ZBS Bridge under earthquakes loading, a time history analysis is thus necessary to provide an important basis for the estimated seismic response of the ZBS Bridge, especially after the engineering

accident in 1998 and subsequent retrofit actions taken on the bridge.

For time history analysis of the ZBS cable-stayed bridge, earthquake ground motion records (i.e., accelerogram) need to be used as input excitation at the bridge pier base. To scale the selected earthquake ground motion records according to the design spectrum, parameters for the local earthquake response spectrum were determined using the Chinese seismic design code (China Ministry of Construction, 2001). These parameters are listed in Table 5.1. The peak ground acceleration (PGA) for the maximum considered earthquake (i.e., rare earthquake with a probability of exceedance of 2% to 3% in 50 years) at the ZBS bridge site is 0.225g. This earthquake thus has a return period around 2000 years.

Five real earthquake ground motion records selected from the Pacific Earthquake Engineering Research (PEER) Center strong motion database (http://peer.berkeley.edu/smcat/) were used for the nonlinear time history analysis of the ZBS bridge seismic response. Additionally, one earthquake ground motion record from the Chinese earthquake records database was also used in this study. The ground motion records are selected on the following basis: earthquake magnitude ranging between 6.5 to 7.0; PGA of the major horizontal component accelerogram around 0.15 g. ideally, to perform a comprehensive seismic response analysis, earthquake records with various spectral shapes (i.e., frequency content) that are consistent with the earthquake faulting mechanism and local site conditions are desired. The details of these six earthquake records including location of station, magnitude, epicenter distance, etc. can be found in Table 5.2. Each record contains three components – two horizontal and one vertical, in order to perform the 3-dimensional time history

110

analysis of the ZBS Bridge. Figure 5.3 shows the original (i.e., unscaled) accelerograms of these six earthquake records. Figure 5.4 plots the pseudo-acceleration response spectra for the six earthquake ground motion records. 5% damping ratio was used in calculating the pseudo-acceleration response spectra.

In the current Chinese seismic design code, the maximum considered earthquake (MCE) with a probability of exceedance 2-3% in 50 years is the largest earthquake considered to be economically practical for design purposes. The design spectrum corresponding to the MCE earthquake for the ZBS bridge site based on the Chinese seismic design code (Chinese Ministry of Construction, 2001) is plotted in Figure 5.4 along with the response spectra of the major horizontal component of the six unscaled earthquake records. In this study, the major horizontal component of the original earthquake records are scaled in order to match the MCE design spectrum using an approach similar to that of Sommerville et al (1997) to target spectra. The shapes of the response spectra of individual time histories were not modified in the scaling procedure. Instead, a single scaling factor was found which minimizes the squared error between the target spectrum and the response spectrum of the major horizontal component of the time history. The scale factor that minimizes the weighted sum of the squared error between the target values and the major horizontal component was calculated. The weights used were 1.0 for all periods of 1.0, 1.5, 2.0, 2.5, and 3.0 seconds, respectively. The scale factor was then applied to the major horizontal components of the time history. The other two components of each earthquake record are scaled according to the recommended ratio 1:0.85:0.65 (i.e., PGA of horizontal 1: PGA of horizontal 2: PGA of vertical = 1:0.85:0.65) by the Chinese seismic design

code commentary (2001). These scaling factors are listed in Table 5.3.

Figure 5.5 plots the scaled pseudo-acceleration spectrum as well as the target spectrum corresponding to the MCE level earthquake at the bridge site. These scaled accelerograms were then used in the time history analysis.

5.3 Finite Element Model and Time History Analysis

As mentioned in the previous chapter, *SAP2000 v.10.0.1* was used in this study for nonlinear time-history analysis of the seismic response of the ZBS Bridge. Cable-stayed bridges have an inherently nonlinear behavior. Although two numerical integration methods are available in SAP2000 - Direct-integration method and Modal method, the Direct-integration method was employed in the nonlinear time history analysis because of its capability to perform nonlinear direct-integration time-history analysis.

Nonlinearity can be broadly divided in geometrical and material nonlinearities. In this study, only two types of geometric nonlinearity (P-delta effects and nonlinearity due to cable sag) are considered; material nonlinearity was not considered since the ZBS Bridge is still within its elastic range under the specified earthquake intensity level. The geometrical nonlinearity can be attributed to: (1) changes in cable geometry due to sagging effects; (2) interaction between axial forces and bending moments in the towers and the deck; and (3) changes of bridge geometry due to its deflections. The nonlinear cable behavior is treated utilizing the Ernest's formula, as described in Chapter 3. The nonlinear behavior of the tower and deck elements due to axial force-bending moment interaction is accounted for by calculating an updated

bending and axial stiffness of the elements. The overall change in the bridge geometry as third source of nonlinearity can be accounted for through updating the bridge geometry by adding the incremental nodal displacements to the previous nodal coordinates before recomputing the stiffness of the bridge in the deformed shape.

In *SAP2000*, a variety of numerical solution algorithms are available for performing the nonlinear direct-integration time-history analysis. The "Hilber-Hughes-Taylor alpha" (HHT) method is utilized in this study to conduct the nonlinear time history analysis of the ZBS bridge. The HHT method is an implicit integration method (Bathe, 1982). A single key parameter in the HHT method is α, which may take any value between 0 and -1/3. In this study, the value of this parameter α is set to be -1/3. The six earthquake motion records are input respectively as base excitation to the ZBS Bridge in the *SAP2000* model. The time interval employed for this numerical simulation study is 0.01 second. The viscous damping ratio for each modes is 0.02. In the nonlinear time history analysis, gravity load from the self-weight of the ZBS Bridge is also combined with the seismic excitation for the consideration of simulating geometrical nonlinearity effect.

5.4 Results and Discussion

Before discussion of the simulation results, it should be noted that the x, y, z axis mentioned in this chapter refers to the global coordinate system as defined in the previous chapter, i.e., x axis coincides with the bridge longitudinal axis, y axis is in the transverse horizontal direction of the bridge, and z axis points up in the vertical direction. The internal forces of the selected bridge sections such as bending moments

113

as well as the displacement and acceleration responses of the ZBS Bridge at selected locations are presented in this reference frame.

5.4.1 Cable Forces

The maximum responses of the tension force in the selected stay cables on the ZBS Bridge under the selected earthquakes are presented in Figure 5.6 . Also, the numerical values of the maximum cable force responses along with the cable force values corresponding to the gravity only load case are given in Table 5.4. It is clearly observed that,

i) Under the selected seismic base excitation, all five selected stay cables are subjected to tension force greater than that corresponding to the gravity only load case. Seismic loading thus has the adverse effect of increasing the risk of damage to stay cables.

ii) The mean value of the maximum cable force response under the selected six earthquakes ranges from 1.02 to 1.25 times the corresponding value of the gravity only load case. The maximum values of cable force response fall between the range of 103% to 133% times the corresponding response values of the gravity only load case. The maximum cable force responses under the selected earthquakes are still below 40% of the yield strength of the corresponding cable. Since the cable force under service load is typically one third of its load capacity, it is judged that under the selected earthquakes, the bridge stay cables most likely would operate safely if satisfactory anchoring condition is maintained.

iii) For Cable C12, its response under various earthquake ground motions has the most diverse distribution among the five stay cables considered. The reason for this phenomenon may be attributed to the fact that cable C12 is located near the mid point of the main span of the ZBS Bridge while other cables are situated at the pier or close to pier, which provides some restraints from excessive movement.

5.4.2 Bridge Tower

The seismic responses of the bridge tower at selected sections (tower base) including their bending moments and axial forces are summarized in Table 5.5. The location of the selected sections is illustrated in Figure 5.7. Figure 5.8 presents the maximum tower responses under six earthquakes along with those values from the gravity only load case. Also, the corresponding strain at extreme fiber of the concrete section under these maximum internal forces acting on the selected sections is calculated and listed in Table 5.5. The most critical strain values are conservatively estimated by calculating the absolute value of strain at extreme fibers (i.e., corner of the section) by combining the maximum moments in either direction and maximum axial compressive force in the section. It can be seen from Table 5.5 that,

i) The average value of the calculated maximum strain in the section is 1054 $\mu\varepsilon$, and the maximum value is 1376 $\mu\varepsilon$, which is well below the failure strain (approximately equal to 0.002 mm/mm) when the concrete is about to crush in compression. The tower is thus viewed as safe in terms of maximum concrete strain under specified seismic loading.

ii) The ratio of mean value R_{eq} over R_g is around 7 and 1.2 for the bending moment in x-x direction and axial force respectively, but is larger (15) for the bending moment in y-y direction. The bending moments in y-y direction under seismic loading and its effect on section needs to be carefully examined in order to ensure the tower section can provide the demanded strength.

5.4.3 Bridge Deck

Table 5.6 lists the seismic responses of the bridge deck at four selected sections as well as their corresponding response under the gravity only load case. The maximum strain at extreme fibers of the section is again conservatively calculated using the above-mentioned approach as in the previous subsection.

Figure 5.9 shows the maximum bending moments and axial forces at selected deck sections under earthquake loading while the corresponding static responses are indicated by dashed lines. It can be concluded that,

i) The responses of Section D03, the section at Pier 22, are the largest among the four selected sections. The maximum strain reaches 1047 $\mu\varepsilon$, which is below the failure strain (approximately equal to 0.002 mm/mm) when the concrete is about to crush in compression.

ii) For other sections, the section load capacity is not exceeded when considering the fact that the strain at extreme fibers of the sections is far smaller than the crush strain of concrete.

5.4.4 Selected Displacement and Acceleration Response Time Histories

Five locations on the ZBS Bridge – D00 (point on deck spine at Pier 20), D02 (point on deck spine at Cable C15), D04 (point on deck spine at Pier 24), D05 (point on deck spine at Pier 25) and T01 (upstream side tower top), were selected to present the displacement and acceleration time histories of the bridge under the selected earthquakes. Figure 5.10 and Figure 5.11 give an example of the displacement response under earthquakes KOB and NIN respectively. Also, Figure 5.12 and Figure 5.13 show acceleration response under earthquake KOB and NIN respectively at selected points. The peak displacement and acceleration responses of the bridge at the selected points under six earthquake are listed in Table 5.7. Based on the simulation results, it is concluded that,

i) By comparing the bridge deck responses at D00, D02 and D04 points, the vertical displacement response of the bridge at D02 is larger than that at D00 or D04. This can be explained by the fact that point D00 and D04 is located at Piers, while D02 is at the mid span of the bridge main span.

ii) At the tower top point T01, the displacement responses are mostly in the x and y directions and very little in the z direction. The drift ratio of the maximum tower top displacement over the tower height is about 0.14% and 0.20% for the displacement responses in the x direction and y direction, respectively. Generally, a structural element with such small level of drift ratio would remain in its elastic range. Therefore, considering the drift response of the tower, the bridge tower appears to operate safely under the earthquakes considered.

iii) For the deck, the ratio of the maximum displacement at mid span over the main span length is about 0.39% in the y direction and 0.14% in the z direction, which is below 1/250 of the half main span length. This level of deformation should be still within allowable range for the bridge deck structure.

iv) Excessive displacements were observed at Pier 20, Pier 24 and Pier 25 under the 1979 Imperial Valley earthquake (i.e., record IM2). In this earthquake, the deck moves by 0.70 m, 0.86 m and 1.00 m at Pier 20, Pier 24 and Pier 25 respectively, which is well over the allowed movement of the bridge bearing (Model GPZ6000SX pot bearing with a diameter of 920 mm). Potential deseating problem for the bridge deck might occur under this earthquake.

5.5 Conclusion

Based on the nonlinear time history analysis of the ZBS cable-stayed bridge under the selected six earthquake ground motions, it can be concluded that,

i) The ZBS Bridge is located in a moderate seismic area with potential for a M6.0 earthquake. Two reasons motivate the current seismic response analysis: the ZBS bridge had a severe engineering accident during construction and conducting time history analysis is necessary to examine the seismic resistance of the retrofitted bridge structure; the design seismic intensity level at the bridge site was increased by one degree from Degree VI to VII and the peak ground acceleration corresponding to the design

seismic intensity level was also increased, thus necessitating a comprehensive seismic analysis.

ii) The finite element model established in SAP2000 for dynamic analysis, as validated in the previous chapter, can be successfully used to simulate the 3-dimensional nonlinear time history responses of the ZBS Bridge under the specified earthquake excitation at pier bases.

iii) Based on the finite element simulation results including cable forces, maximum concrete strain at the critical sections of the bridge tower and deck, displacement and acceleration responses at selected locations on the bridge, it appears that the main structure elements of the ZBS bridge are still within its elastic range while potential deseating problem for bridge deck might occur under the selected earthquake ground motions, which are scaled to the MCE target spectrum for the bridge site. The MCE target spectrum with a PGA value equal to 0.225 g corresponds to a probability of exceedance of 2 ~ 3% in 50 years for the local site.

Table 5.1 Earthquake response spectrum parameters for the ZBS Bridge site (China Ministry of Construction 2001)

	Item	Value
1	Site categorization	III (top soft soil layer with shear wave velocity $\upsilon_{se} < 140$ m/s, layer thickness $= 14 \sim 33$ m)
2	Design earthquake group	First group
3	Maximum value of horizontal earthquake influence factor α_{max} (for rare earthquake[*])	0.50 g
4	Peak ground motion ($= 0.45\ \alpha_{max}$)	0.225 g
5	Site characteristics period	0.45 sec

Note: * rare earthquake refers to an earthquake with a probability of exceedance equal to 2% ~ 3% in 50 years (equivalent to the maximum considered earthquake (MCE) in NEHRP code).

Table 5.2 Details of the selected earthquake records

Name	Date	Record code	Record Station (component code)	Epicenter Dist. (km)	Magnitude	Duration (s)	Data Points	PGA (g)
Imperial Valley	1940/05/19	IM1	117 El Centro Array #9, (I-ELC-UP, I-ELC180, I-ELC270)	12.99	7.0	40	4000	0.313
Imperial Valley	1979/10/15	IM2	5056 El Centro Array #1, (H-E01-UP, H-E01140, H-E01230)	35.18	6.5	39	7807	0.139
Kobe	1995/01/16	KOB	0 HIK, (HIK-UP, HIK000, HIK090)	135.63	6.9	78	3900	0.148
Loma Prieta	1989/10/18	LOM	57383 Gilroy Array#6, (G06-UP, G06000, G06090)	35.47	6.9	40	7991	0.170
Ninghe	1976/11/25	NIN	02001 Tianjin Hospital, (Ninghe-EW, Ninghe-SN, Ninghe-UP)	65.00	6.9	19	1919	0.149
San Fernando	1971/02/09	SAN	125 Lake Hughes, (L01DWN, L01021, L01111)	-	6.6	30	3000	0.145

Note: PGA = peak ground acceleration

Table 5.3 Scaling factor for the major horizontal component of selected earthquake records

EQ Record	MCE Scale Factor	PGA after scaling (g)
IM1	0.601	0.188
IM2	2.093	0.291
KOB	1.769	0.262
LOM	1.349	0.229
NIN	0.640	0.095
SAN	0.819	0.119
	Average value =	0.197

Table 5.4 Comparison of maximum cable force response under earthquake (Unit: kN)

Cable No.		C25		C12		C0		C12'		C25'	
		U	D	U	D	U	D	U	D	U	D
IM1		6217	6168	4192	4176	4486	4477	3526	3504	6288	6356
IM2		6151	6090	4047	4064	4532	4536	3493	3618	6410	6468
KOB		6590	6618	4423	4364	4430	4428	3535	3770	6388	6374
LOM		6561	6466	4530	4502	4476	4464	3446	3497	6319	6309
NIN		6229	6253	4482	4531	4460	4465	3369	3376	6154	6180
SAN		6050	6091	3993	4055	4423	4425	3360	3392	6206	6158
F_{eq}	mean	6300	6281	4278	4282	4468	4466	3455	3526	6294	6308
	max	6590	6618	4530	4531	4532	4536	3535	3770	6410	6468
F_g		5682	5682	3412	3412	4387	4379	3140	3140	5948	5948
F_y		16900	16900	12017	12017	14332	14332	12017	12017	19339	19339
F_{eq} mean/ F_g		1.11	1.11	1.25	1.25	1.02	1.02	1.10	1.12	1.06	1.06
F_{eq} max/ F_g		1.16	1.16	1.33	1.33	1.03	1.04	1.13	1.20	1.08	1.09
F_{eq} mean/ F_y		0.37	0.37	0.36	0.36	0.31	0.31	0.29	0.29	0.33	0.33
F_{eq} max/ F_y		0.39	0.39	0.38	0.38	0.32	0.32	0.29	0.31	0.33	0.33

Note: U = upstream side cable

D = downstream side cable

F_{eq} = response from time history analysis

F_g = response from gravity only load case

F_y = yield force of stay cables

Table 5.5 Maximum tower response at sections C01 (upstream) and C02 (downstream) under earthquakes

		Maximum M_{xx} (kN·m)		Maximum M_{yy} (kN·m)		Maximum P (kN)		ε ($\mu\varepsilon$)	
		upstream	downstream	upstream	downstream	Upstream	downstream	upstream	downstream
IM1		3.883E+05	5.287E+05	7.990E+05	8.886E+05	2.491E+05	2.518E+05	878	1039
IM2		6.286E+05	8.240E+05	7.536E+05	1.049E+06	2.701E+05	2.751E+05	1068	1376
KOB		3.312E+05	4.807E+05	1.145E+06	1.324E+06	2.414E+05	2.358E+05	994	1200
LOM		3.829E+05	4.691E+05	9.593E+05	1.038E+06	2.415E+05	2.505E+05	947	1062
NIN		3.185E+05	4.465E+05	9.323E+05	8.860E+05	2.394E+05	2.481E+05	879	968
SAN		4.657E+05	2.324E+05	6.546E+05	6.634E+05	2.211E+05	2.389E+05	853	677
R_{eq}	mean	4.192E+05	4.969E+05	8.740E+05	9.748E+05	2.438E+05	2.500E+05	936	1054
	max	6.286E+05	8.240E+05	1.145E+06	1.324E+06	2.701E+05	2.751E+05	1068	1376
R_g		6.367E+04	6.368E+04	6.427E+04	6.418E+04	2.079E+05	2.079E+05	226	226
R_{eq} mean/ R_g		6.58	7.80	13.60	15.19	1.17	1.20	4.14	4.66
R_{eq} max/ R_g		9.87	12.94	17.82	20.63	1.30	1.32	4.73	6.09

Note: M_{xx}, M_{yy} = bending moment of the section about x-x, and y-y axes respectively, in unit of kN-m
P = axial compressive force in unit of kN
ε = concrete strain at extreme fiber of the section, calculated from M_{xx}, M_{yy}, P
R_{eq} = response from time history analysis
R_g = response from gravity loading only case
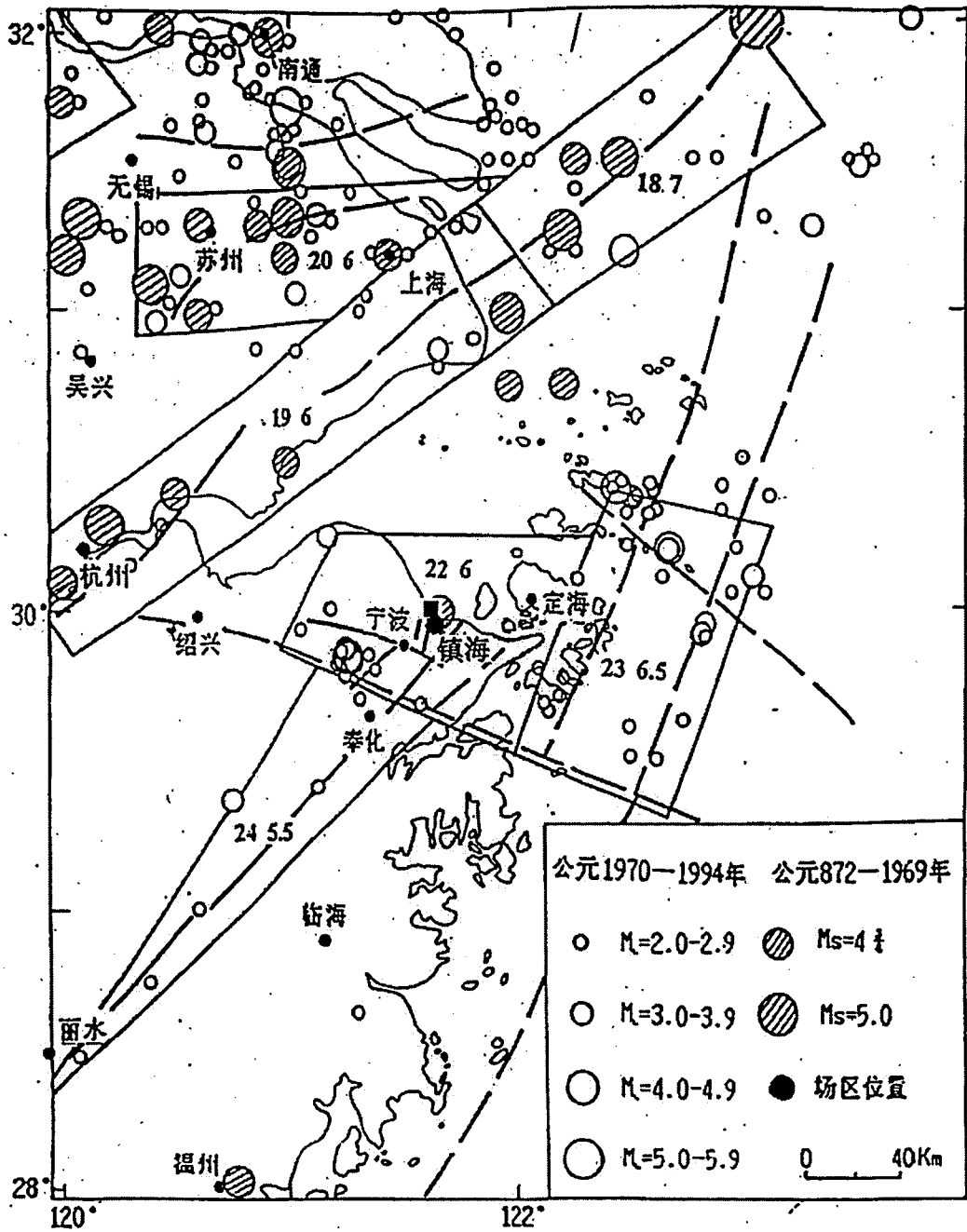R_g mean = mean value of response from gravity loading only case
R_g max = max value of response from gravity loading only case
The tower section considered is located immediately below the lower traverse beam of the bridge tower

123

Table 5.6 Maximum deck response at selected sections under earthquakes

Location		D01				D02			
		M_{yy} max	M_{zz} max	P max	ε ($\mu\varepsilon$)	M_{yy} max	M_{zz} max	P max	ε ($\mu\varepsilon$)
IM1		8.450E+05	2.418E+05	7.893E+03	688	6.728E+04	3.673E+05	1.140E+05	802
IM2		8.555E+05	2.892E+05	6.164E+03	706	5.251E+04	1.008E+06	1.071E+05	922
KOB		9.432E+05	5.778E+05	1.010E+04	841	8.825E+04	3.713E+05	1.233E+05	952
LOM		9.018E+05	2.994E+05	7.776E+03	744	8.472E+04	3.845E+05	1.135E+05	912
NIN		8.515E+05	1.802E+05	7.546E+03	678	6.763E+04	2.827E+05	1.134E+05	773
SAN		8.328E+05	1.528E+05	5.944E+03	657	5.347E+04	1.884E+05	1.054E+05	636
R_{eq}	8.716E+05	8.716E+05	2.902E+05	7.570E+03	719	6.898E+04	4.337E+05	1.128E+05	833
	9.432E+05	9.432E+05	5.778E+05	1.010E+04	841	8.825E+04	1.008E+06	1.233E+05	952
R_g		1.131E+00	7.092E+05	1.119E+03	167	7.507E+03	1.000E+01	8.758E+04	251
R_{eq} mean/R_g		-	0.41	6.77	4.31	9.19	-	1.29	3.32
R_{eq} max/R_g		-	0.81	9.03	5.05	11.76	-	1.41	3.79
Location		D03				D04			
		M_y max	M_z max	P max	ε ($\mu\varepsilon$)	M_y max	M_z max	P max	ε ($\mu\varepsilon$)
IM1		8.786E+04	3.763E+05	1.843E+05	854	9.364E+04	1.569E+05	3.495E+04	401
IM2		7.736E+04	1.467E+06	1.733E+05	1022	1.067E+05	2.265E+05	1.128E+04	423
KOB		1.181E+05	5.489E+05	1.912E+05	1047	1.283E+05	3.111E+05	3.794E+04	567
LOM		1.011E+05	4.034E+05	1.838E+05	917	9.923E+04	1.528E+05	3.518E+04	416
NIN		9.299E+04	2.548E+05	1.827E+05	836	9.300E+04	1.062E+05	3.465E+04	379
SAN		7.128E+04	2.071E+05	1.714E+05	708	9.633E+04	1.703E+05	8.095E+03	365
R_{eq}	mean	9.145E+04	5.429E+05	1.811E+05	912	1.029E+05	1.873E+05	2.702E+04	425
	max	1.181E+05	1.467E+06	1.912E+05	1022	1.283E+05	3.111E+05	3.794E+04	567
R_g		3.903E+04	5.729E+01	1.457E+05	458	8.053E+04	1.936E-01	2.710E+04	288
R_{eq} mean/R_g		2.34	-	1.24	1.96	1.28	-	1.00	1.47
R_{eq} max/R_g		3.03	-	1.31	2.28	1.59	-	1.40	1.97

Note (Table 5.6 continued):

    D01 = deck section above Pier 21

    D02 = deck section at Cable C15

    D03 = deck section at Pier 22

    D04 = deck section at Pier 24

    M_{yy}, M_{zz} = bending moment of the section about y-y, z-z axes respectively, in unit of kN-m

    P = axial compressive force of the deck section, in unit of kN

    R_{eq} = response from time history analysis

    R_g = response from gravity only load case

    R_g mean = mean value of response from gravity only load case

    R_g max = max value of response from gravity only load case

Table 5.7 Maximum displacement and acceleration responses at selected points

EQ	Locations	Displacement (m)					Acceleration (m/s^2)				
		T01	D00	D02	D04	D05	T01	D00	D02	D04	D05
IM1	x direction	0.16	0.09	0.09	0.10	0.10	2.80	1.41	1.18	1.17	1.18
	y direction	0.20	0.15	0.06	0.12	0.16	2.72	2.80	1.52	0.58	2.84
	z direction	0.03	0.02	0.34	0.02	0.02	1.99	1.58	3.14	0.84	1.58
IM2	x direction	0.17	0.08	0.08	0.09	0.09	2.85	1.24	1.14	1.11	1.11
	y direction	0.30	0.70	0.13	0.86	1.00	4.40	3.01	1.85	1.71	4.03
	z direction	0.03	0.02	0.33	0.02	0.02	2.38	2.13	2.61	1.31	1.91
KOB	x direction	0.21	0.13	0.12	0.12	0.14	3.52	1.86	1.63	1.97	1.99
	y direction	0.09	0.11	0.05	0.15	0.14	3.90	6.30	3.10	0.63	5.46
	z direction	0.03	0.02	0.36	0.02	0.02	2.58	2.32	4.51	2.77	2.57
LOM	x direction	0.16	0.10	0.09	0.11	0.12	3.80	1.71	1.62	1.64	1.65
	y direction	0.18	0.19	0.07	0.06	0.20	2.22	3.20	1.44	0.58	2.70
	z direction	0.03	0.02	0.37	0.02	0.02	2.85	2.06	3.37	0.98	1.85
NIN	x direction	0.14	0.10	0.09	0.11	0.11	1.78	1.33	1.29	1.19	1.19
	y direction	0.15	0.09	0.06	0.06	0.10	2.37	1.76	0.96	0.39	1.75
	z direction	0.03	0.02	0.37	0.02	0.02	1.18	0.71	3.41	0.51	0.77
SAN	x direction	0.14	0.08	0.07	0.09	0.09	1.53	0.97	0.92	0.97	0.98
	y direction	0.10	0.04	0.04	0.04	0.05	1.57	1.52	0.81	0.44	2.91
	z direction	0.03	0.02	0.27	0.02	0.02	1.10	1.05	2.47	0.72	0.95

Note: T01 = point at upstream side tower top   D00 = point at Pier 20 along the deck spine line
        D02 = point at Cable 15 along the deck spine line   D04 = point at Pier 24 along the deck spine line
        D05 = point at Pier 25 along the deck spine line

126

公元1970—1994年　公元872—1969年

○　M=2.0-2.9　　◎　Ms=4 ½

○　M=3.0-3.9　　◉　Ms=5.0

○　M=4.0-4.9　　●　场区位置

○　M=5.0-5.9　　0 ___ 40Km

22　6　潜在震源区（编号22，震级上限为6级）

Figure 5.1 Distribution of historical earthquakes in the study region of the ZBS Bridge (Geophysics Research Institute 1996)

127
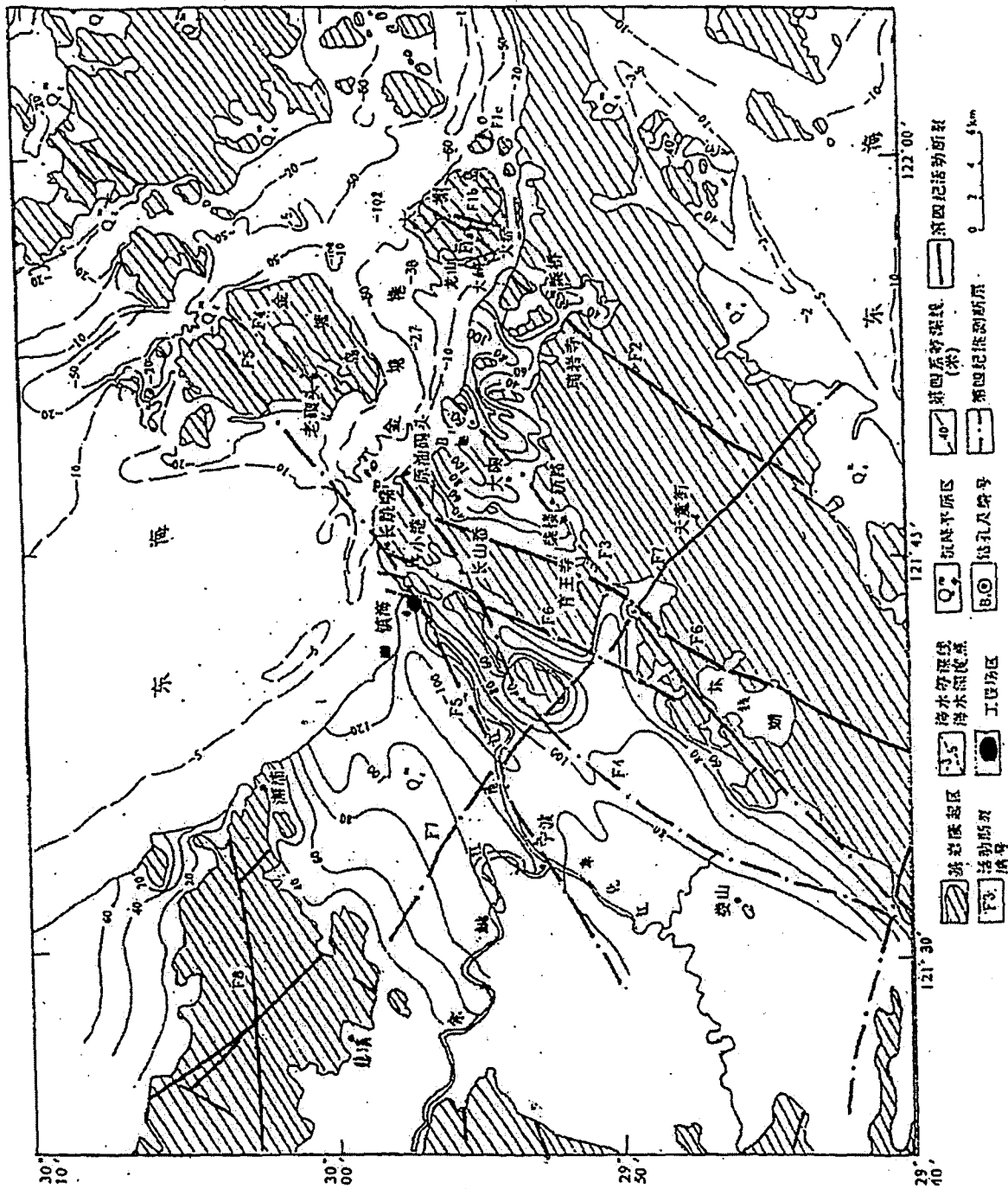
Figure 5.2 Distribution of major active earthquake faults near the bridge site
(Geophysics Research Institute 1996)

128
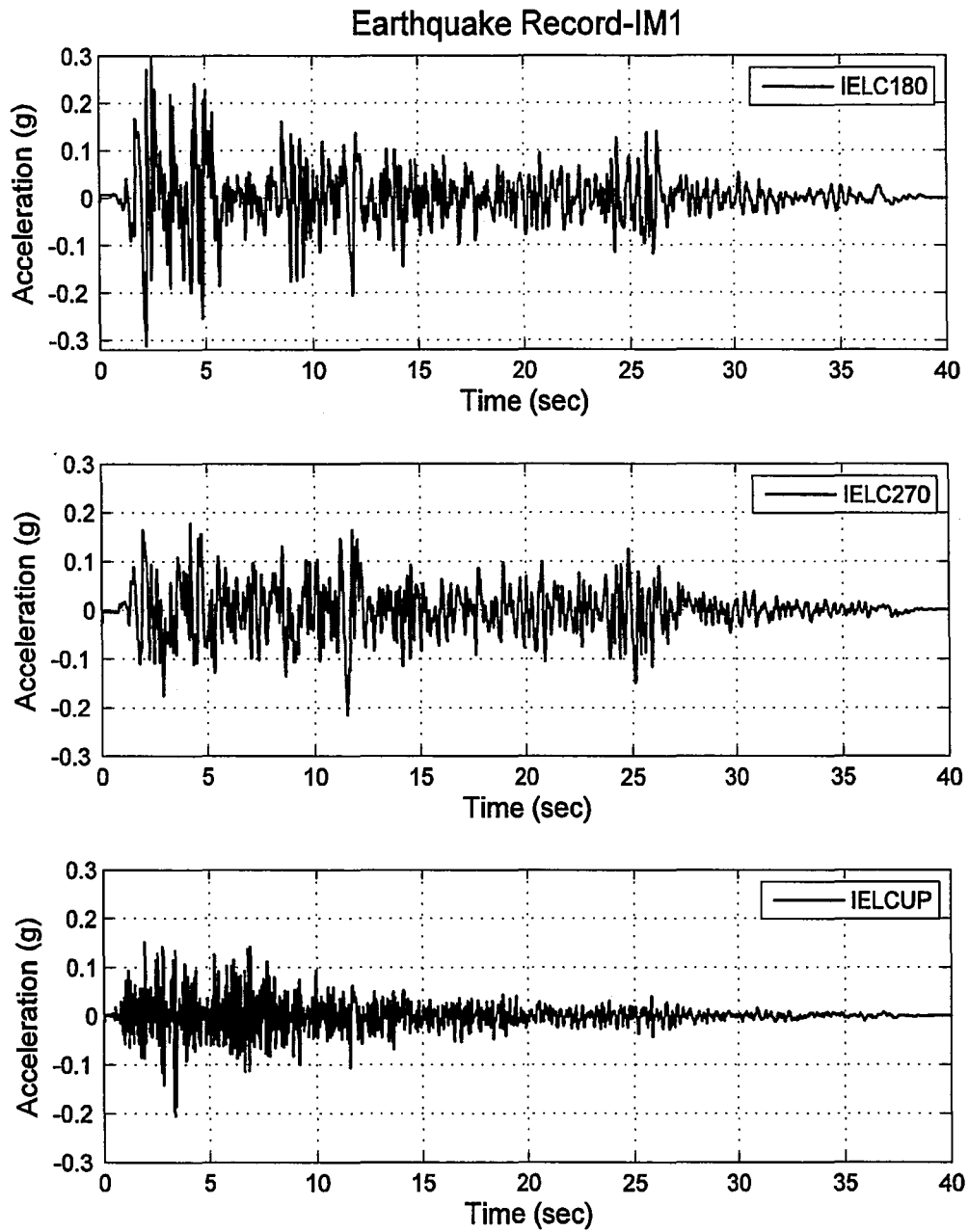
Figure 5.3 (a) Three components of the IM1 earthquake record
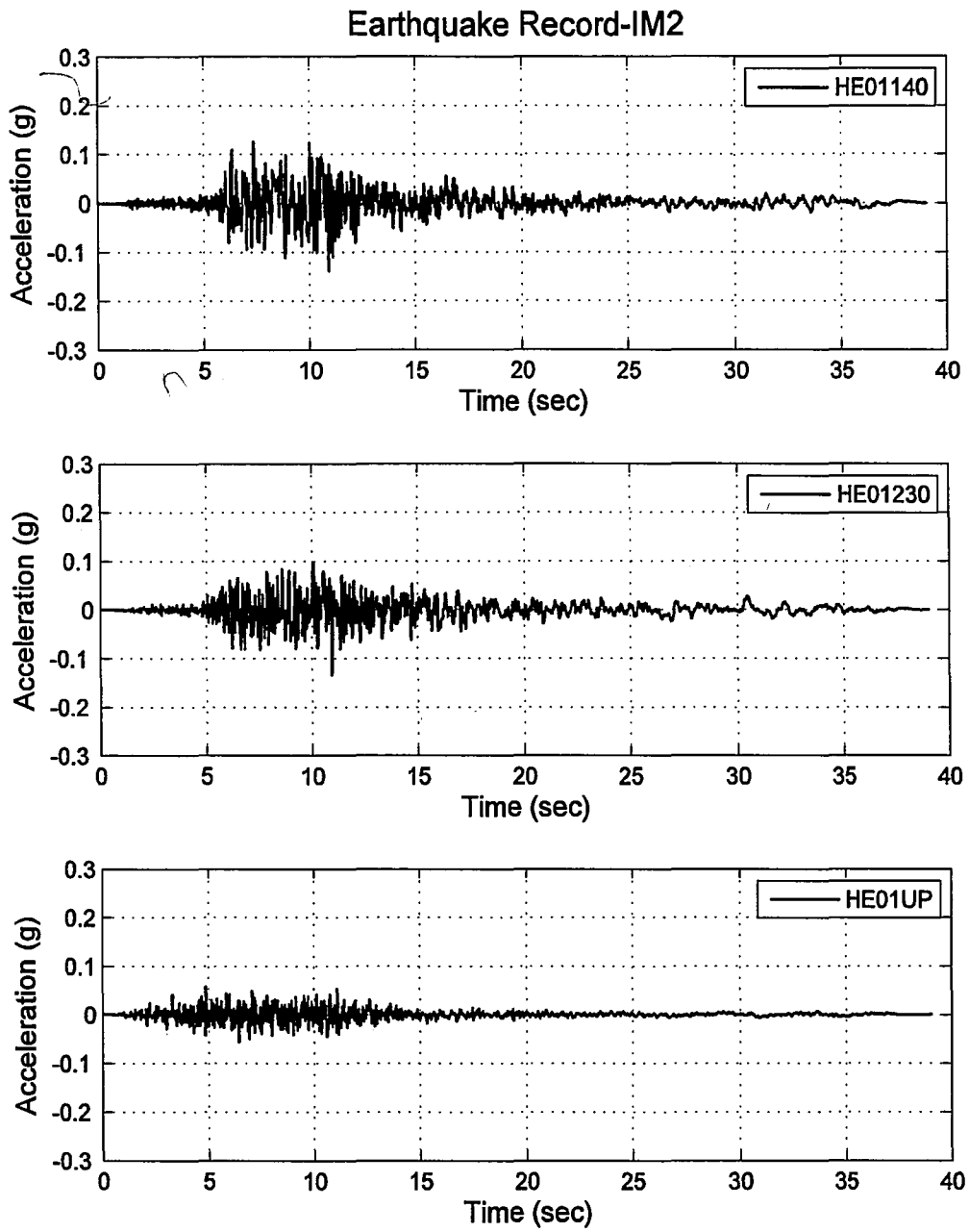
Figure 5.3 (b) Three components of the IM2 earthquake record
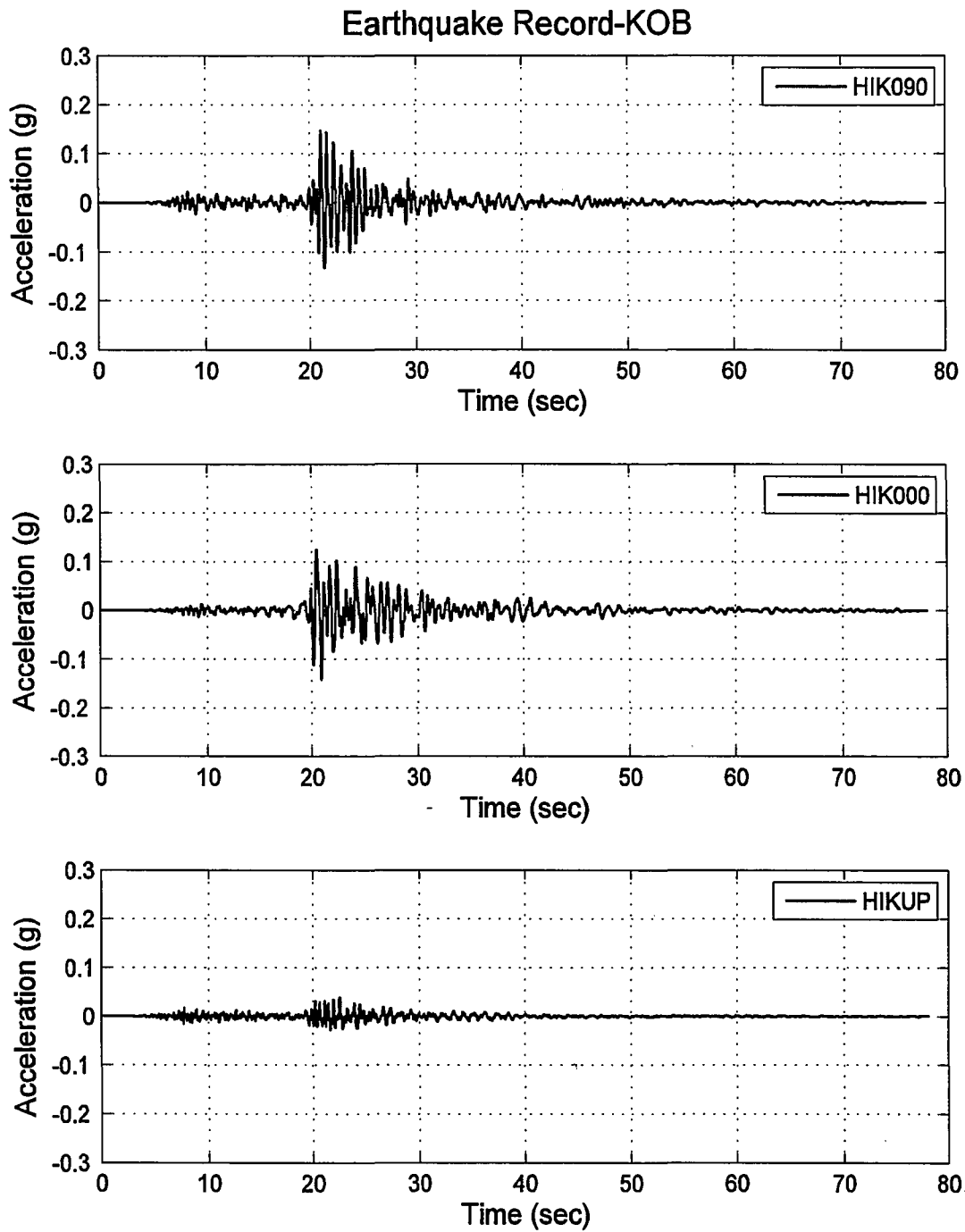
Figure 5.3 (c) Three components of the KOB earthquake record

131
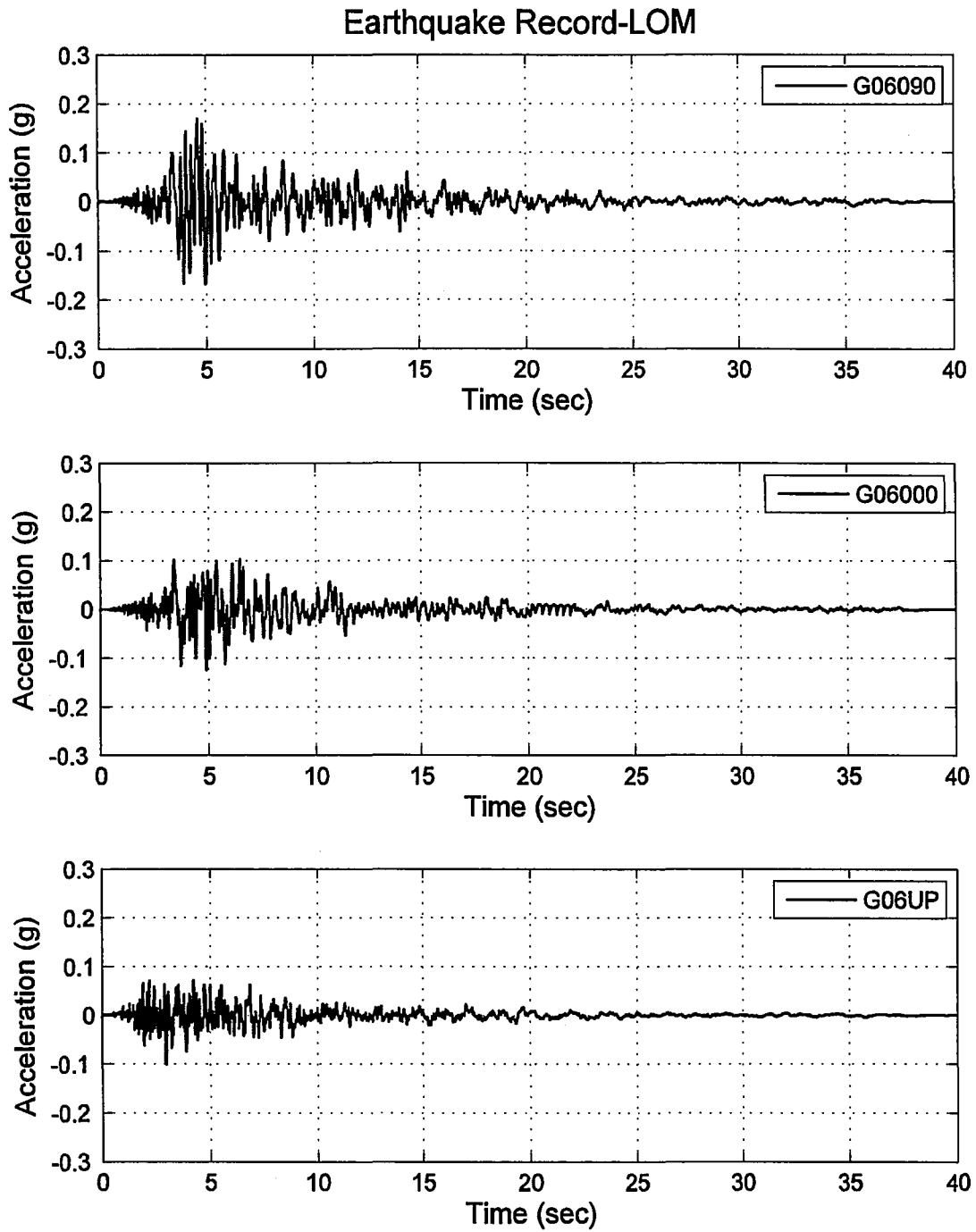
Figure 5.3 (d) Three components of the LOM earthquake record
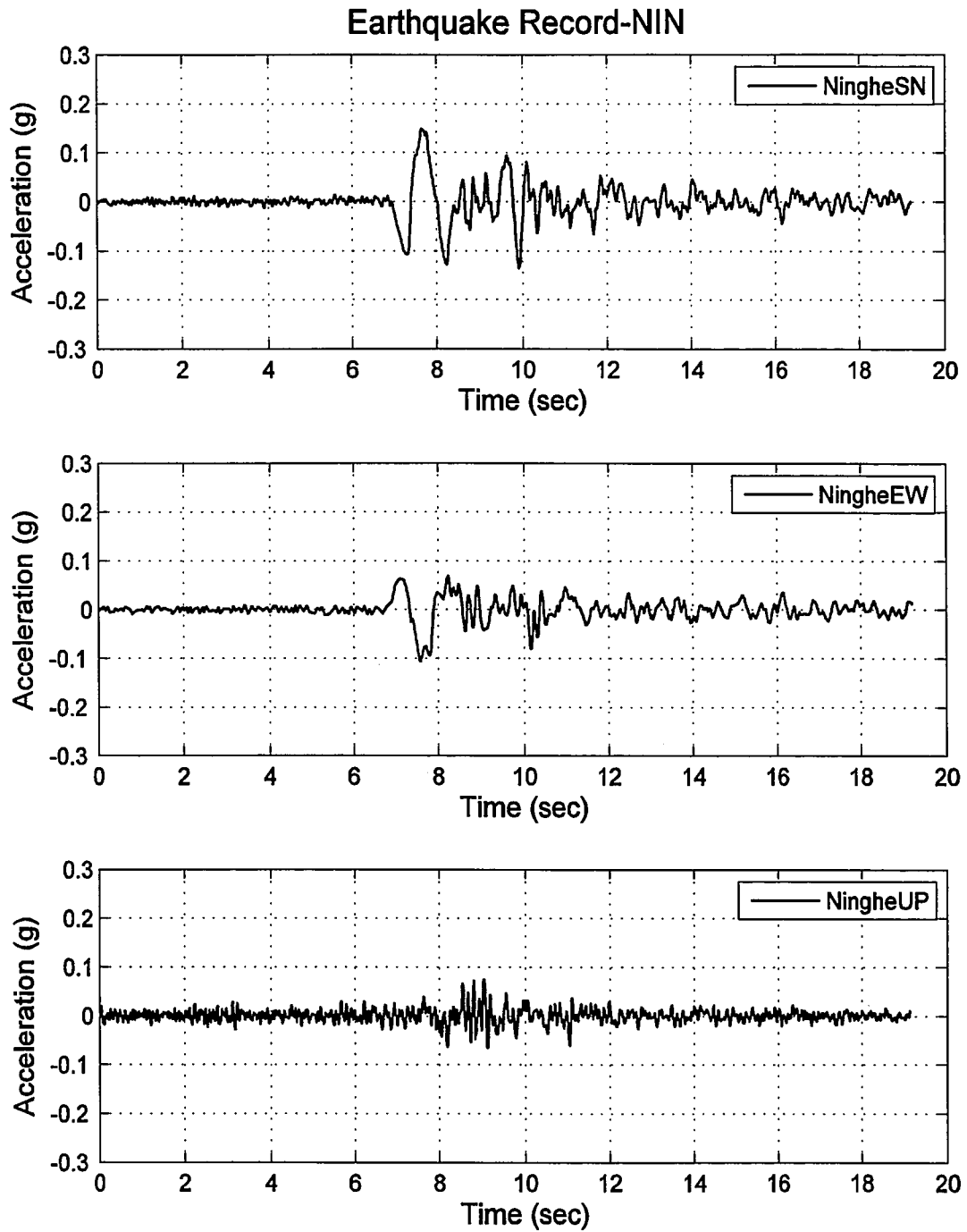
Figure 5.3 (e) Three components of the NIN earthquake record

133
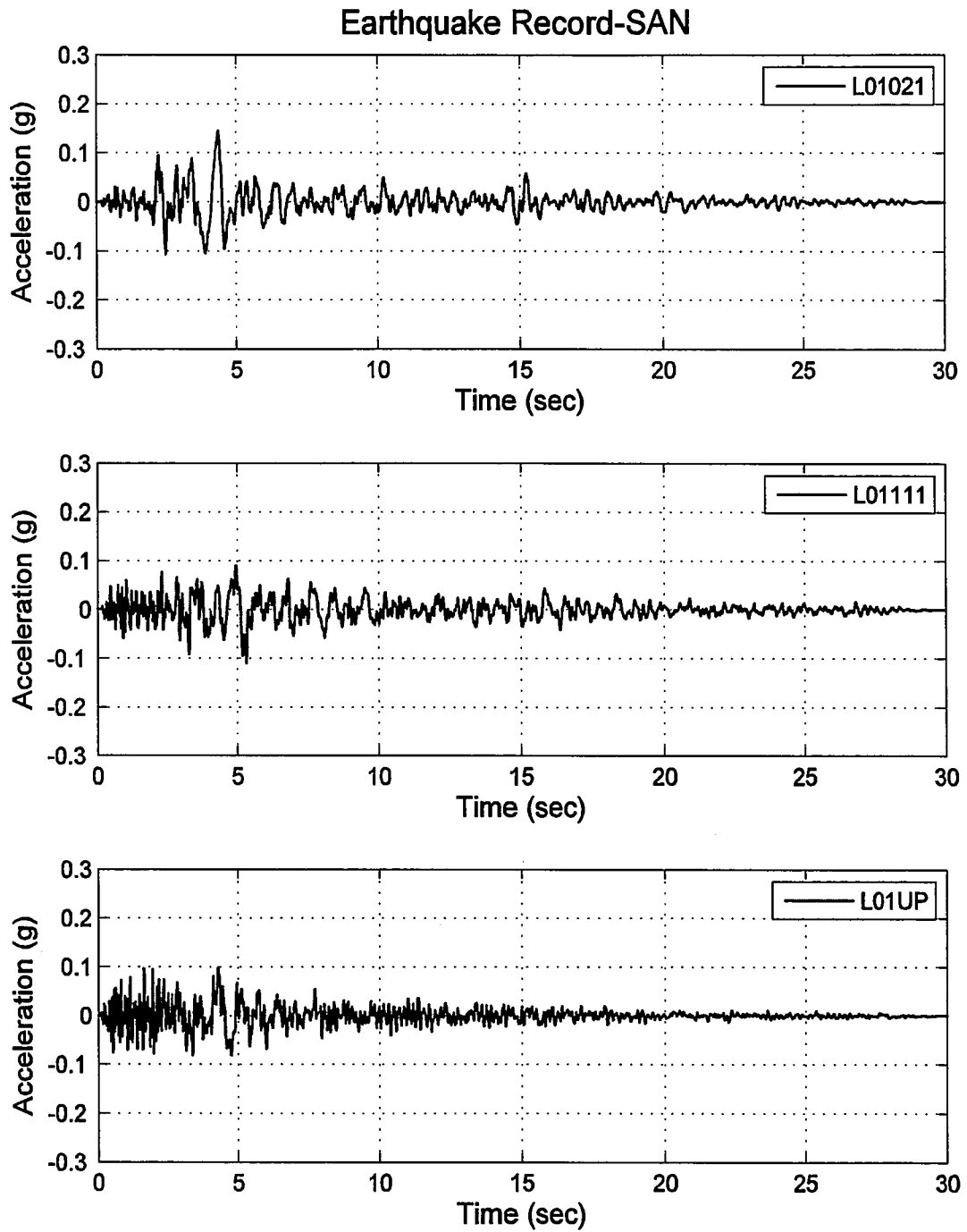
Figure 5.3 (f) Three components of the SAN earthquake record

Figure 5.3 Original earthquake records
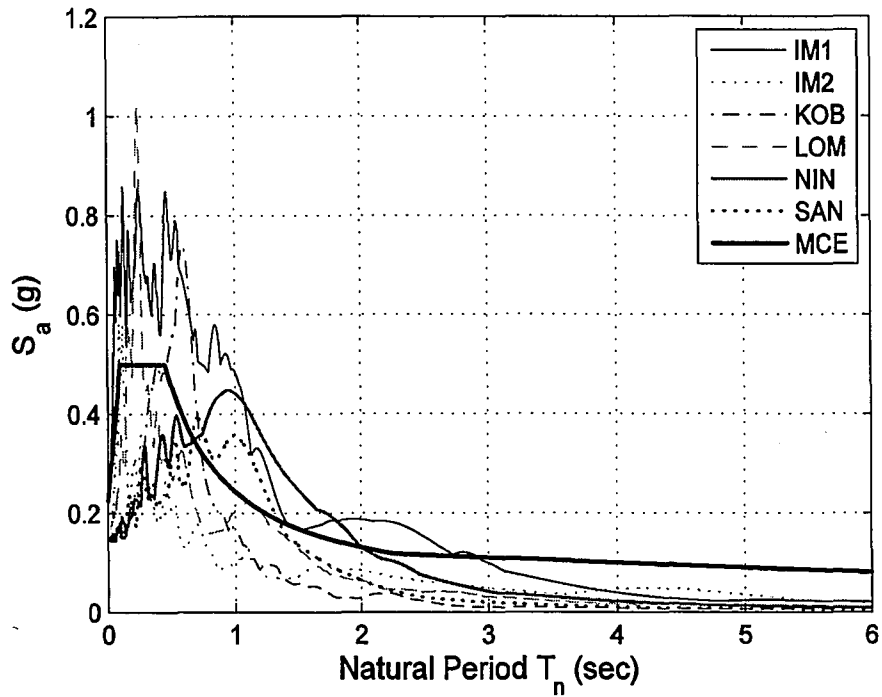
Figure 5.4 Pseudo-acceleration response spectrum and target MCE spectrum
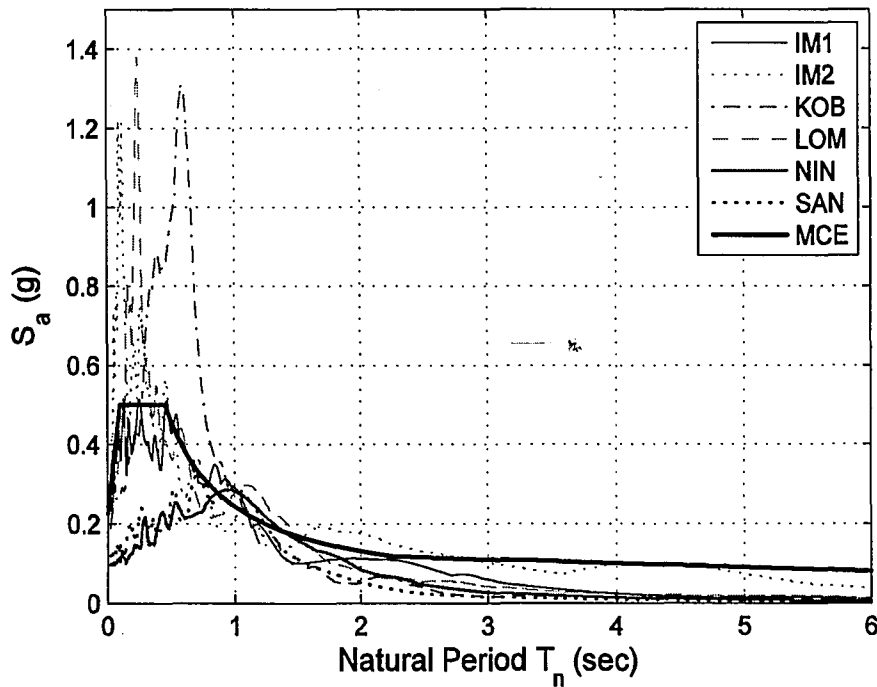
Figure 5.5 Response spectra of scaled earthquake records and target MCE spectrum
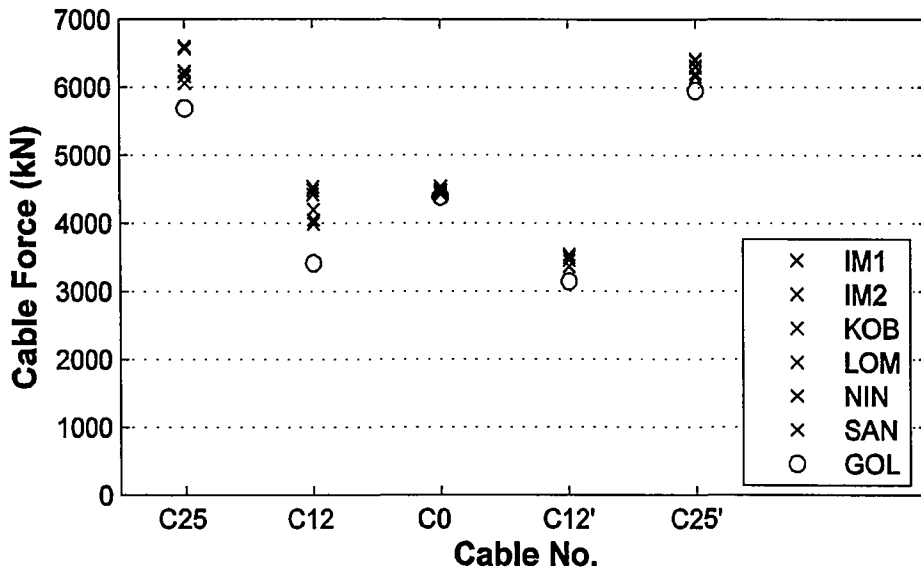
(a) Upstream side cables
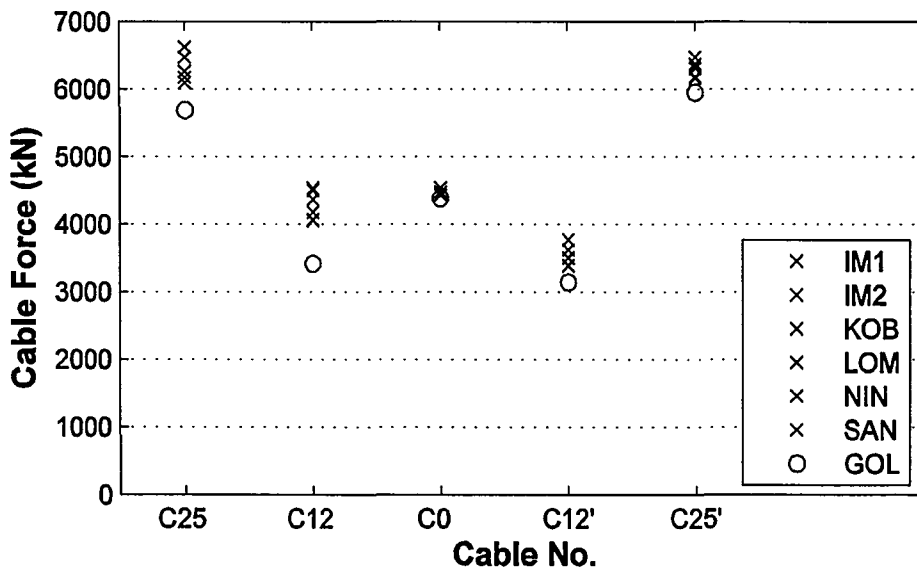
(b) Downstream side cables

Figure 5.6 Maximum force response in selected stay cables (GOL = gravity only load case)
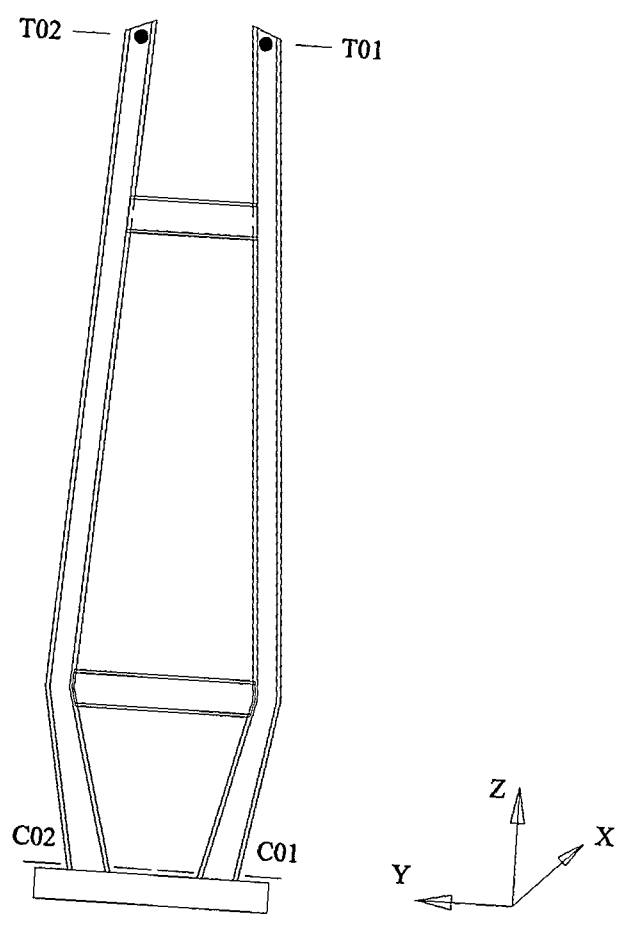
Figure 5.7 Locations of selected cross-sections in tower
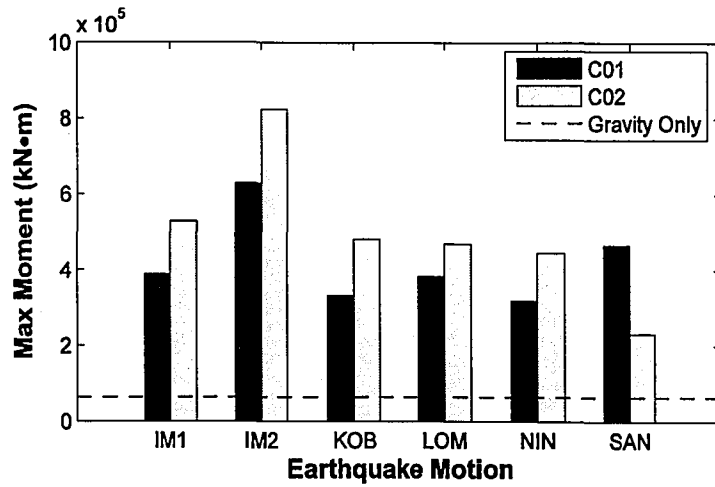
(a) Bending moment M_{xx}
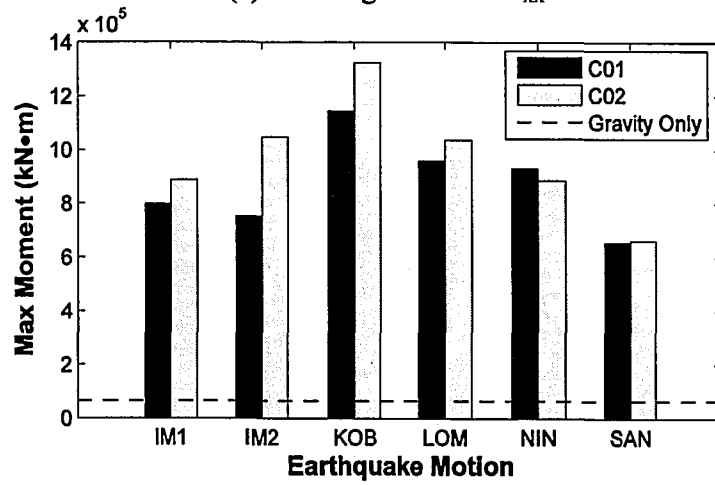
(b) Bending moment M_{yy}
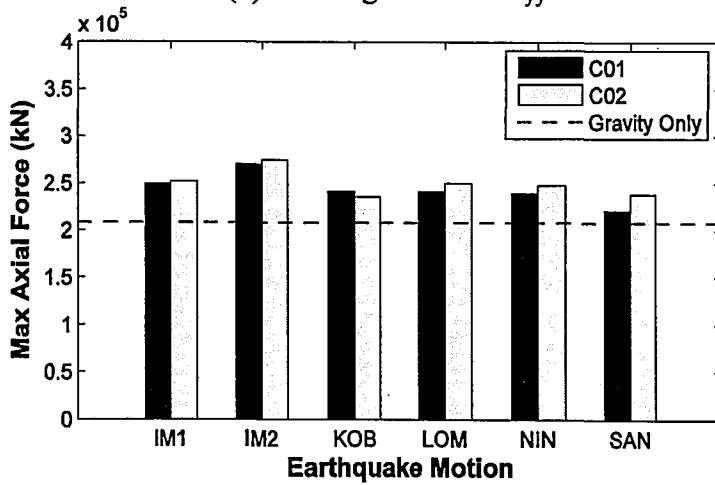
(c) Axial Force

Figure 5.8 Maximum bending moment and axial force in selected tower sections

138
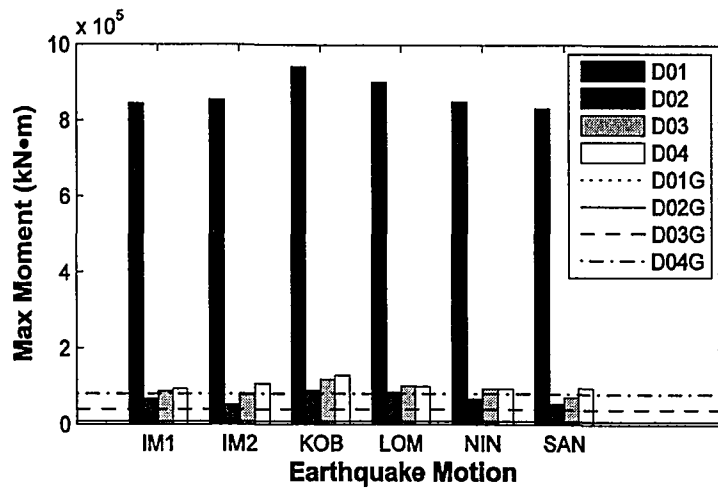
(a) Bending moment Myy
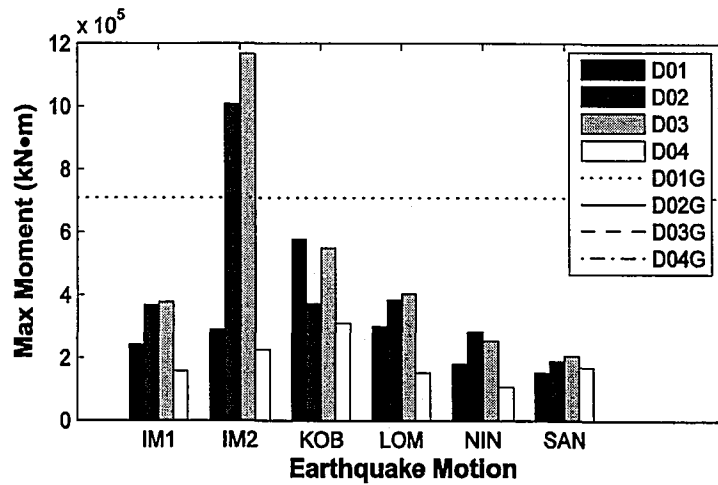
(b) Bending moment Mzz
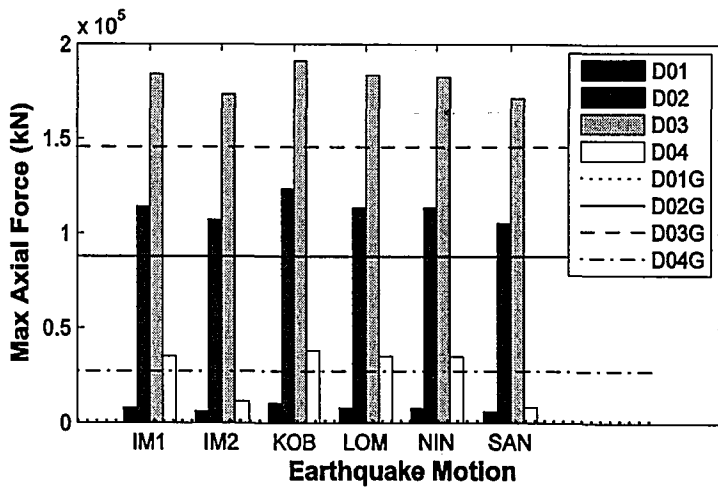
(b) Axial Force

Figure 5.9 Maximum bending moment and axial force response in selected bridge deck sections (G = gravity only load case)
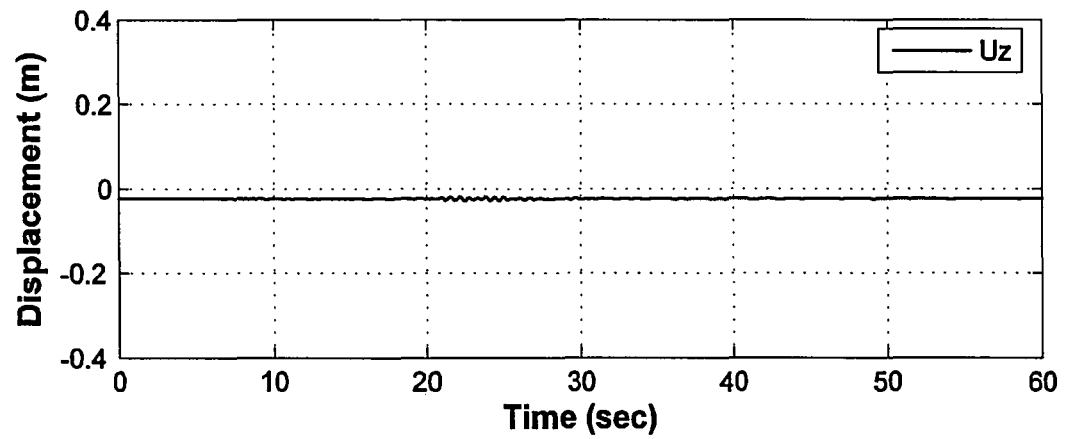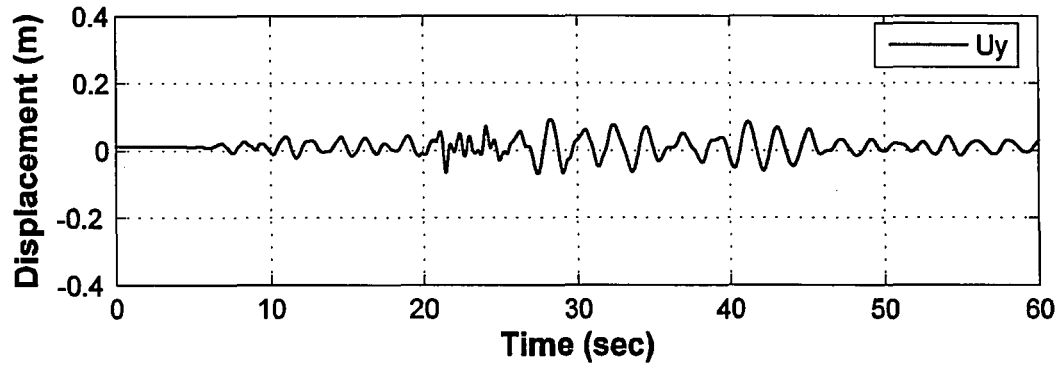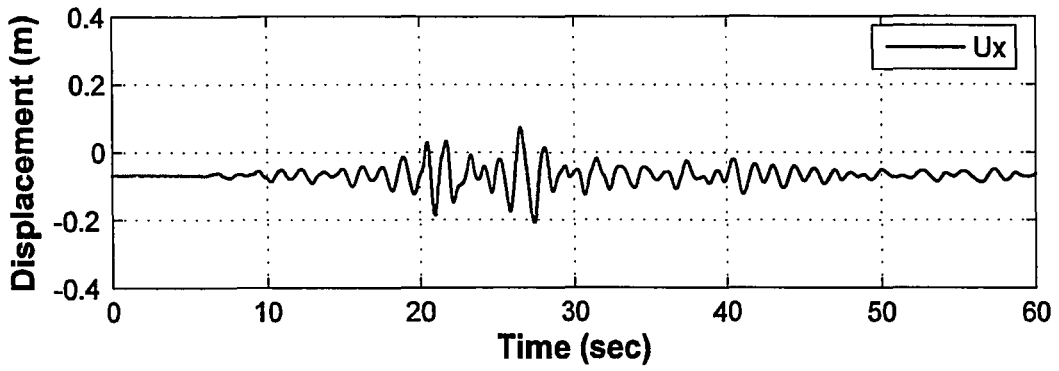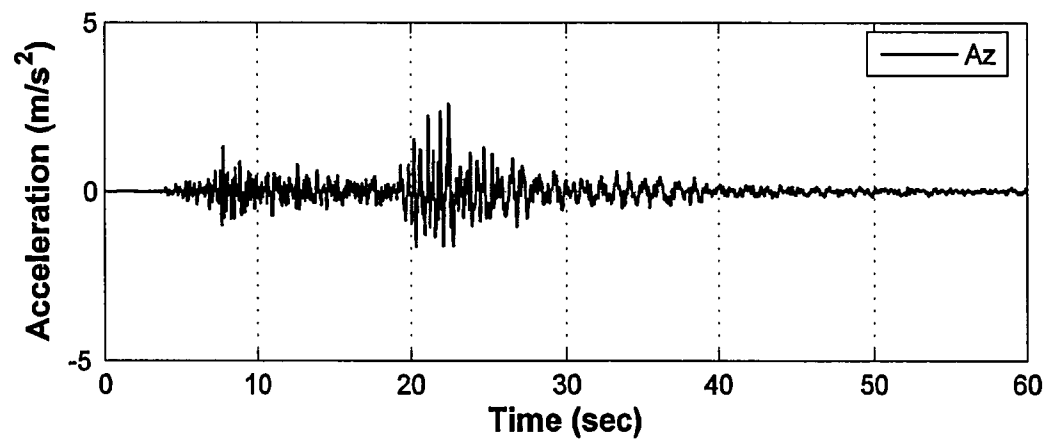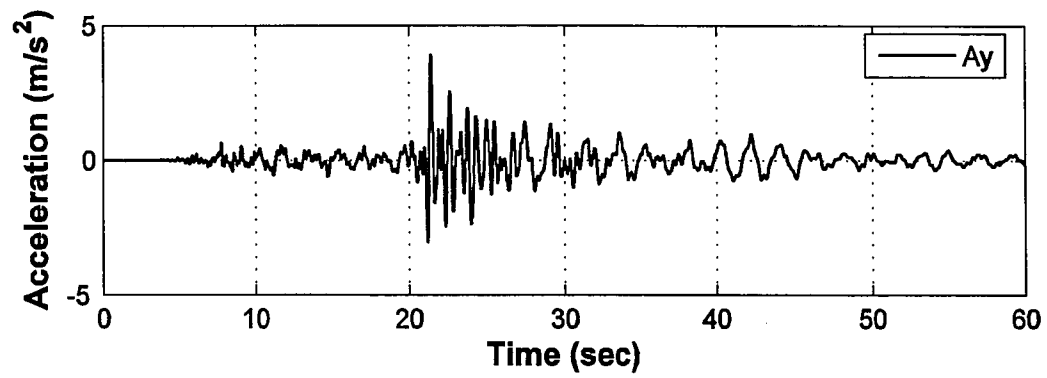
Figure 5.10 (a) Displacement time history (three components: x, y, x) of tower top T01 under earthquake KOB
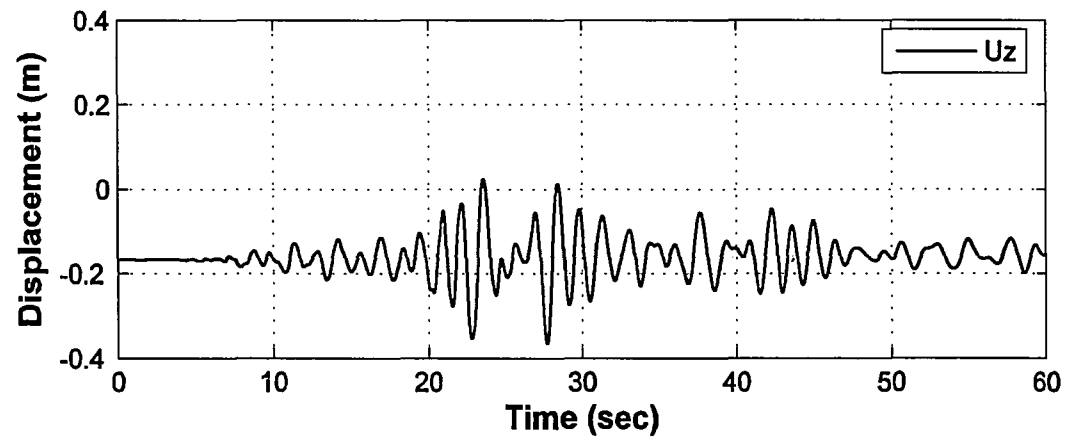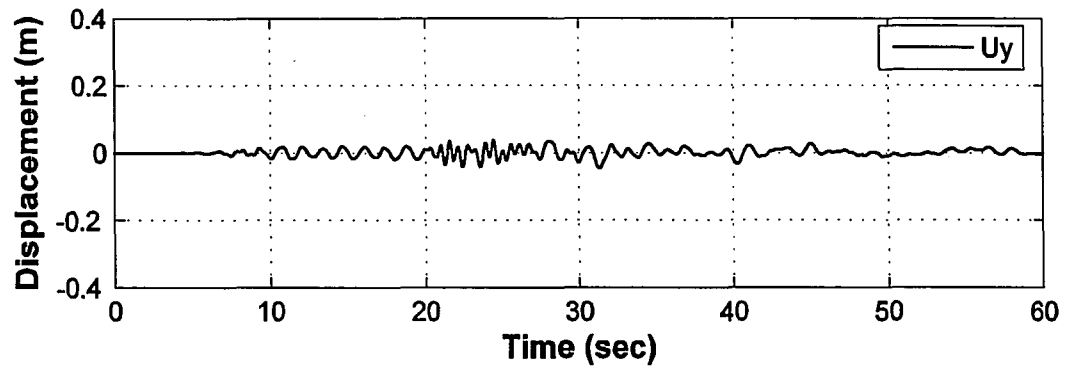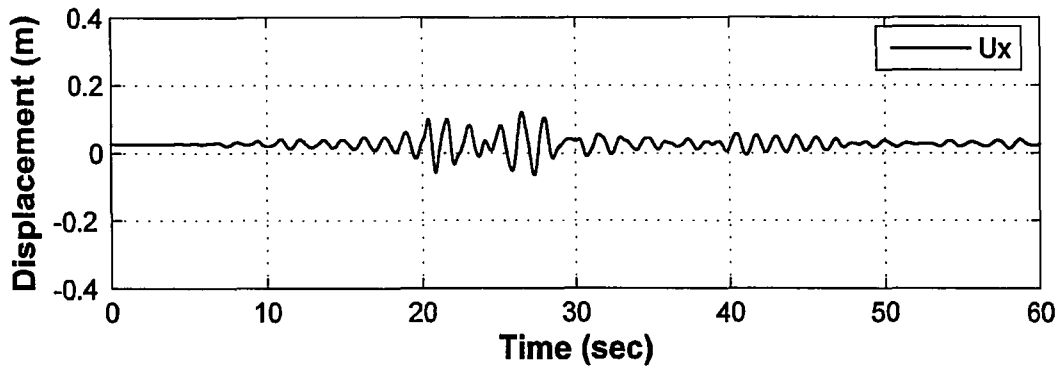
Figure 5.10 (b) Displacement time history (three components: x, y, x) of bridge deck point D02 under earthquake KOB

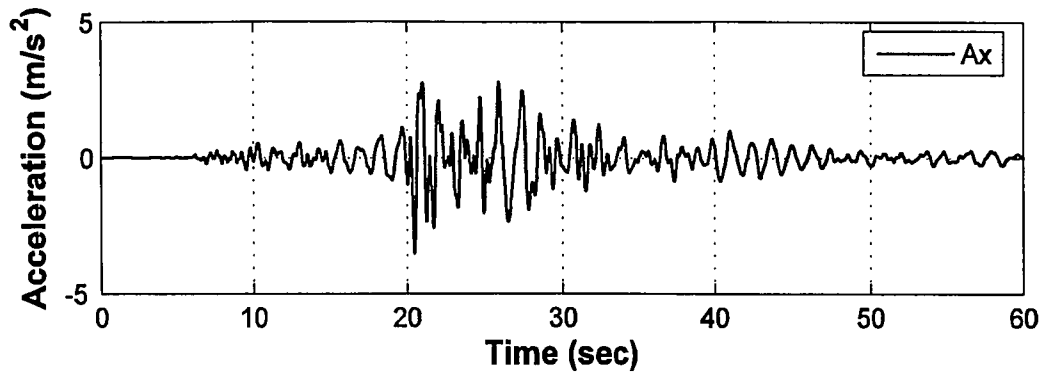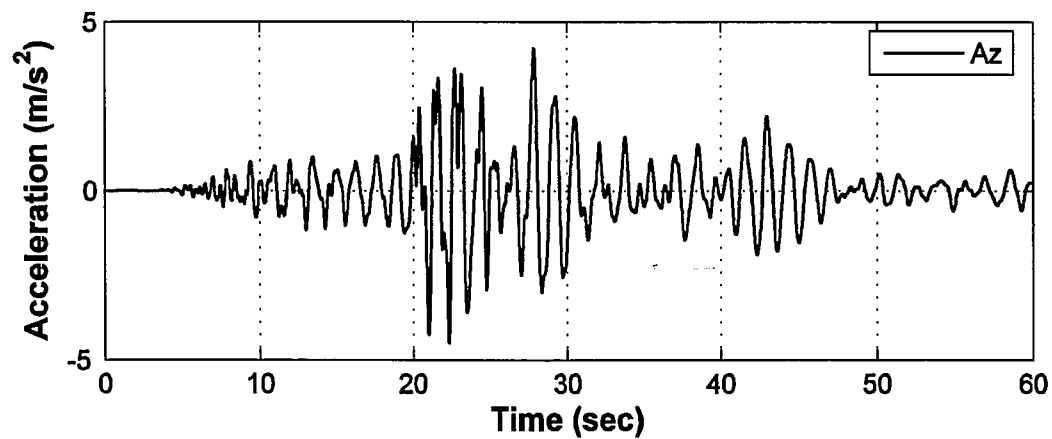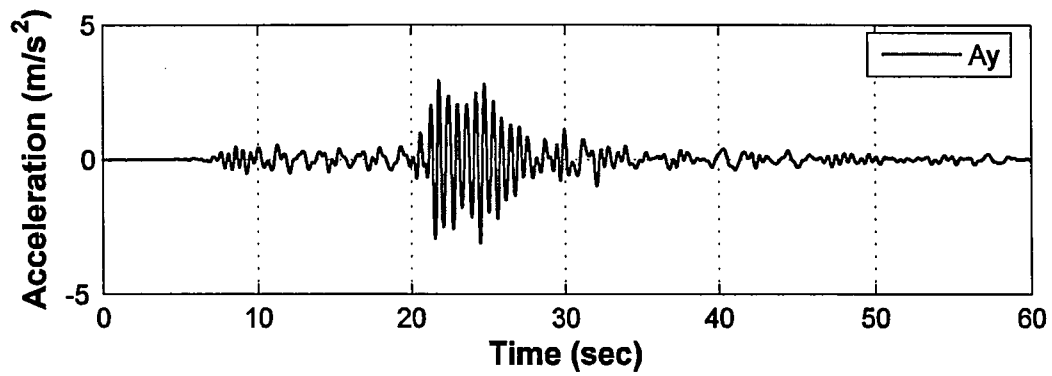**Figure 5.10** Displacement time history at selected locations under earthquake KOB
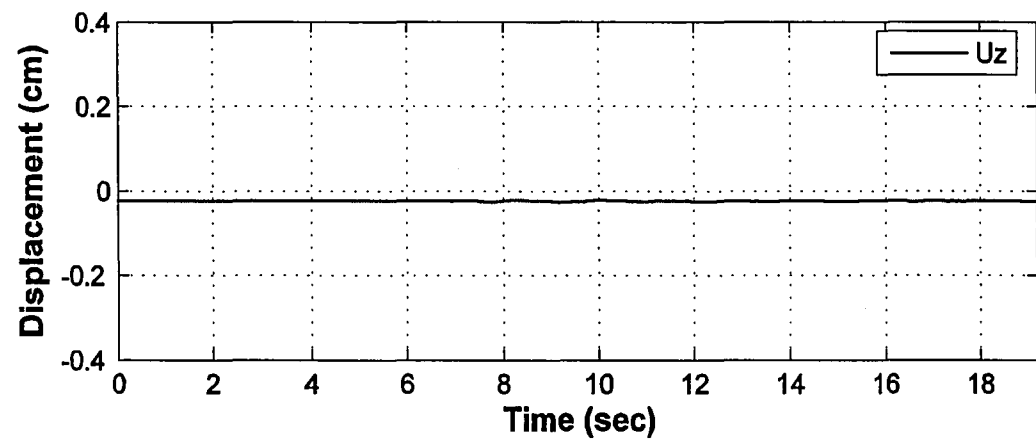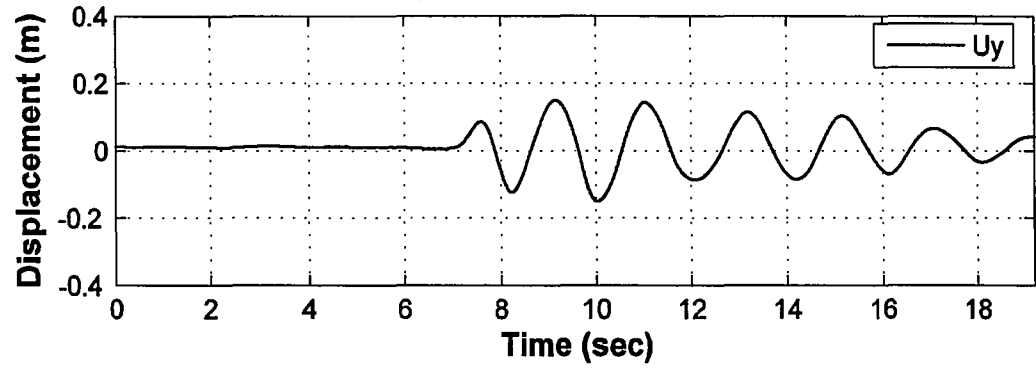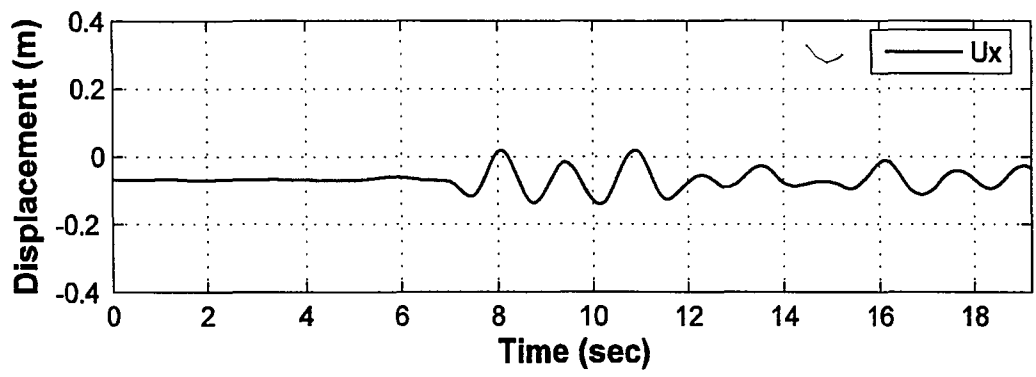
Figure 5.11 (a) Displacement time history (three components: x, y, x) of tower top T01 under earthquake NIN
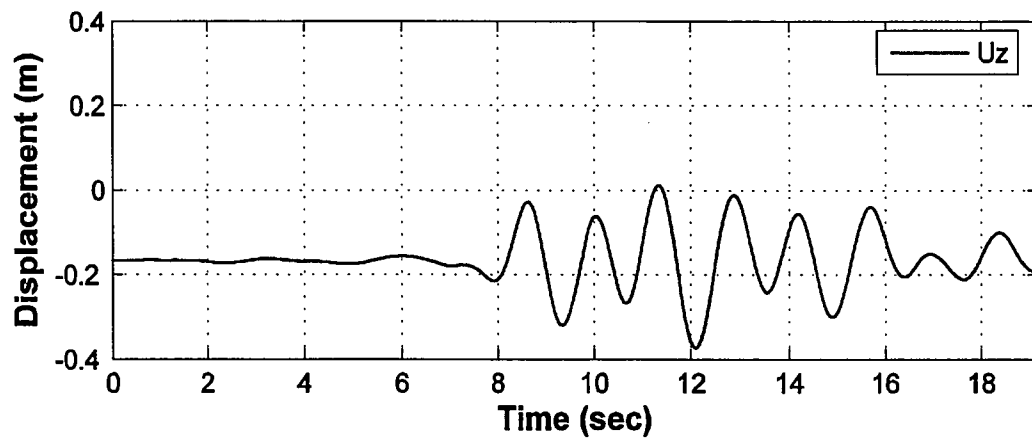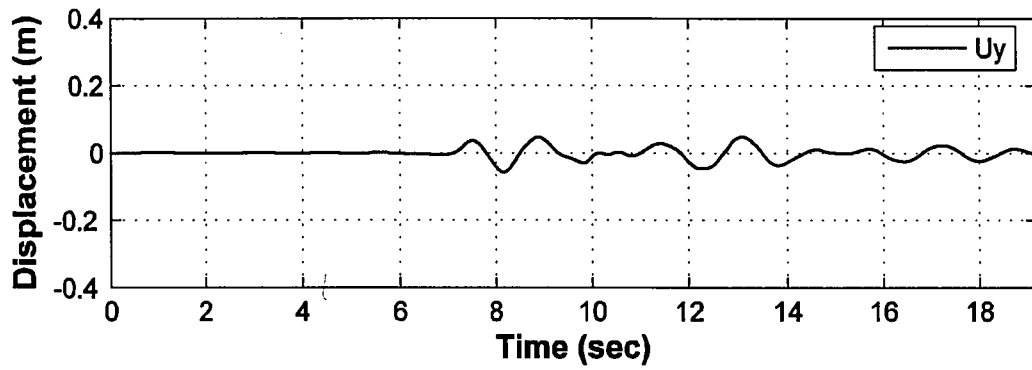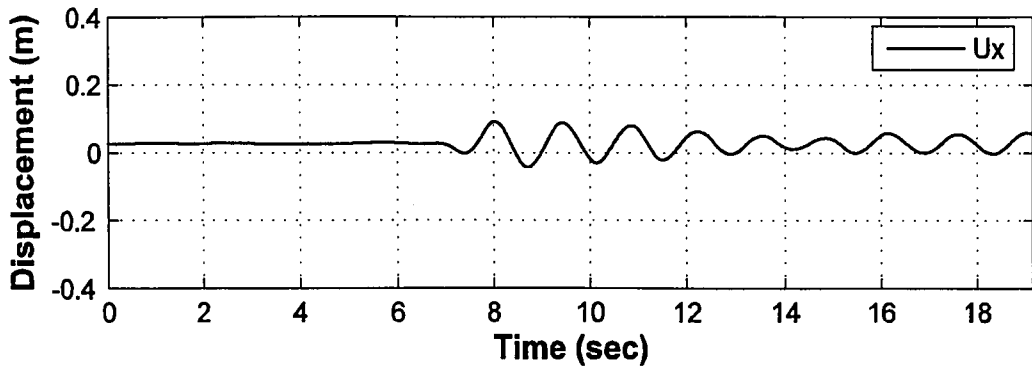
Figure 5.11 (b) Displacement time history (three components: x, y, x) of bridge deck point D02 under earthquake NIN

Figure 5.11 Displacement time history at selected locations under earthquake NIN

143

Figure 5.12 (a) Acceleration time history (three components: x, y, x) of tower top T01 under earthquake KOB
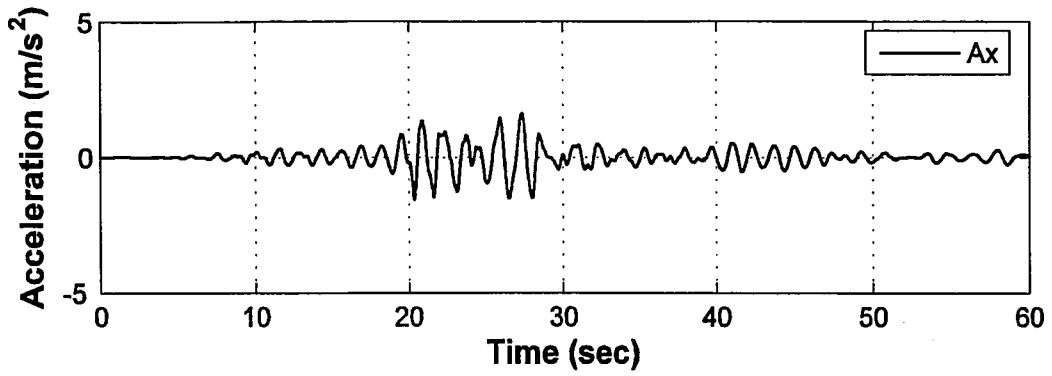
Figure 5.12 (b) Acceleration time history (three components: x, y, x) of bridge deck point D02 under earthquake KOB

Figure 5.12 Acceleration time history at selected locations under earthquake KOB
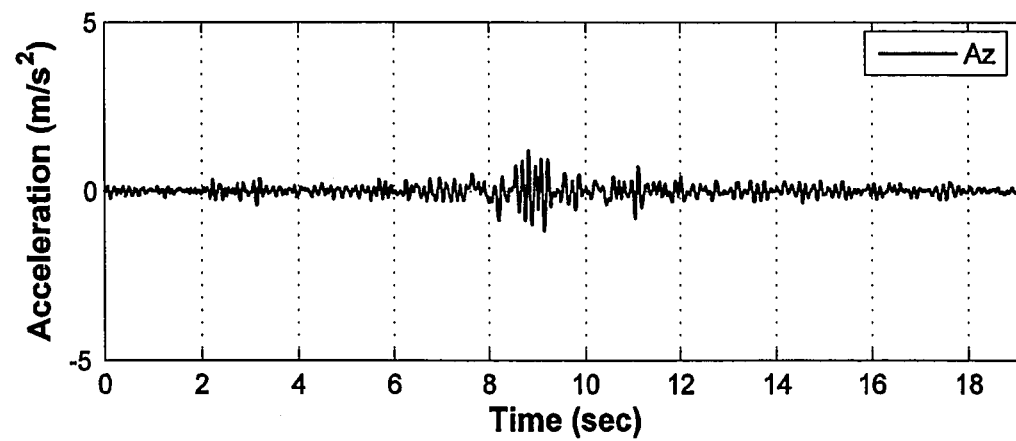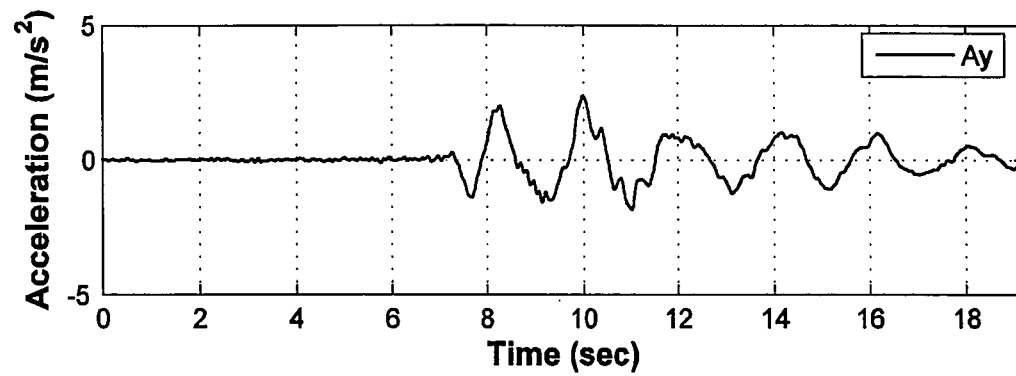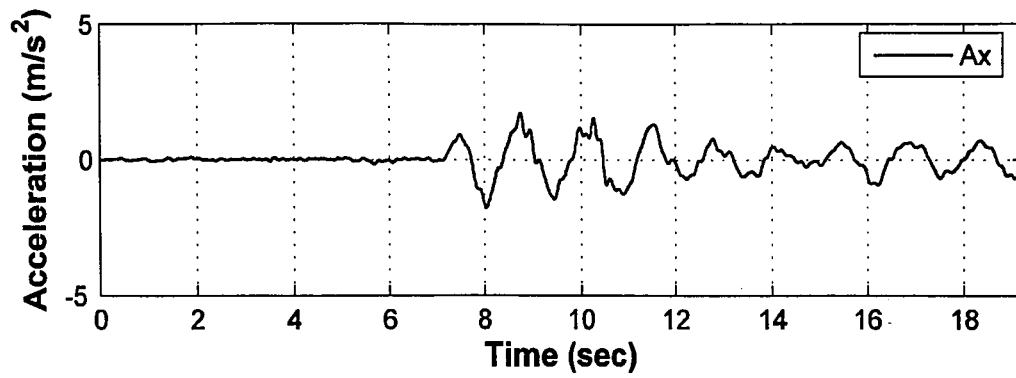
145

Figure 5.13 (a) Acceleration time history (three components: x, y, x) of tower top T01 under earthquake NIN
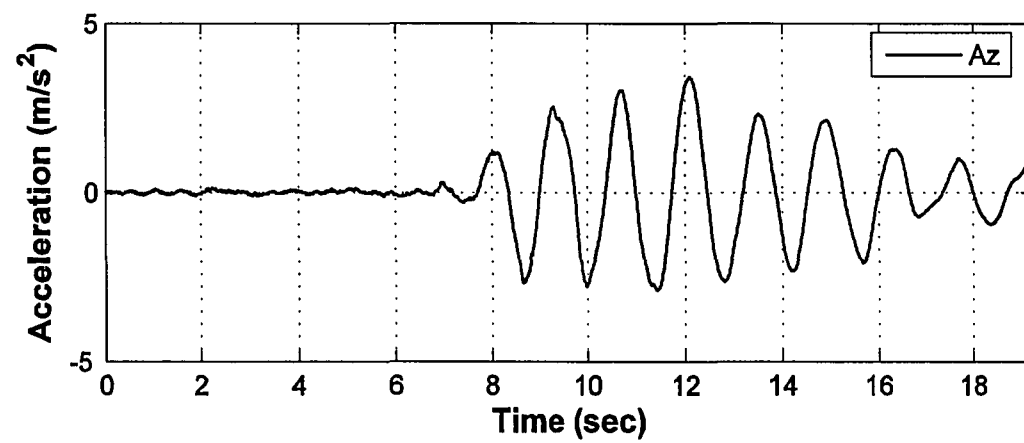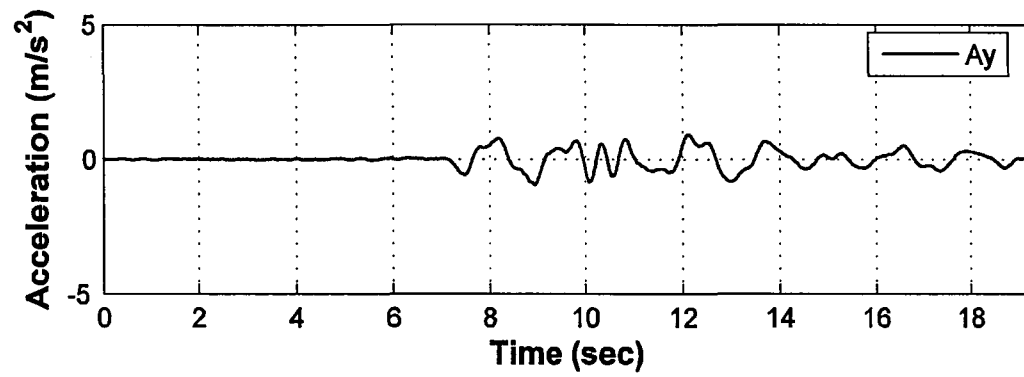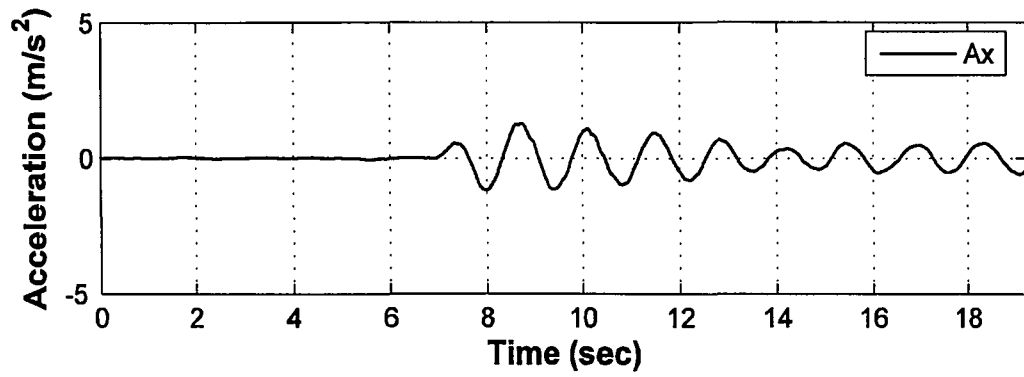
146

Figure 5.13 (b) Acceleration time history (three components: x, y, x) of bridge deck point D02 under earthquake NIN

Figure 5.13 Acceleration time history at selected locations under earthquake NIN

147

Chapter 6

Summary and Future Work

In this chapter, based on the research work presented in the previous chapters, key findings from this research are summarized, which are followed with a discussion of future research work.

6.1 Summary

1) The current research on the static and seismic response of the ZBS Bridge is important to its safety and durability for the following reasons: (a) the severe engineering accident that happened in 1998 during the construction of the ZBS bridge raises questions on the bridge's real load capacity and operating condition, which supposedly is different from the original design after retrofit actions. (b) In 2002, the seismic design intensity level in the local area of the ZBS bridge site was adjusted from Degree VI to VII. Since its construction was completed in 2001, the ZBS Bridge was designed for a seismic intensity level lower than that specified in the current seismic design code. It is necessary to check the safety of ZBS Bridge under the increased earthquakes loading.

2) The finite element models developed in SAP2000 give modal frequency results that are in good agreement with those derived from the ambient test

148

data. The errors are below 15% for the first four dominant modes in the two finite element models considered in this study.

3) Two finite element models were established – one is based on the use of shell elements for bridge girders (referred to as shell element model) and the other uses beam elements for bridge girders (referred to as beam element model). While the shell element model can be used for static load analysis such as effect of thermal differentials on bridge, the shell element model is much more computational demanding than the beam element model. The beam element model is computationally very efficient while being able to fairly well capture the dynamic response behavior of the ZBS Bridge.

4) For the thermal differential loading case considered, the prediction from the finite element model is consistent with the field survey data of deck displacement, tower displacement and strain at selected deck sections.

5) In seismic response analysis, a total of six ground motion records (each with three components – two horizontal and one vertical) scaled to the target response spectrum (corresponding to earthquakes with 2% probability of exceedance in 50 years) are considered as base excitation to the ZBS Bridge. The nonlinear time history analysis of the ZBS Bridge under these earthquakes response indicates that the main elements of the ZBS Bridge will work within its elastic range while potential deseating problem for bridge deck might occur under the selected earthquake ground motions.

6.2 Future Work

1) The existing seismic response data from cable stayed bridges in the United States is quite limited. To better understand the seismic response behavior of the cable stayed bridges, more analytical and experimental research work in this aspect need to be done.

2) For soft soil site (e.g., reclaimed land site), it is an interesting topic to study the soil-structure interaction behavior of cable-stayed bridge during seismic analysis. However, in the ZBS Bridge case, soil-structure interaction was not considered because of the fact that the piles comprised of deep rock-socketed frictional end-bearing bored piles of different diameters were used. The deepest rock-socketed piles were embedded into bed rock by 30 m. Therefore, fixed base was assumed at all pier bases in this study.

3) Since the earthquake intensity level was increased from Degree VI to VII after the ZBS Bridge was constructed and the bridge site is close to several potential faults with one fault crossing right underneath its approach spans, it is desirable to further investigate the seismic response behavior of the ZBS Bridge under earthquakes with seismic intensity level VIII. Energy dissipation devices, e.g. dampers, can be applied to the bridge if the bridge is found to have excessive displacements under these earthquakes and effect of such structural control devices can be evaluated.

4) The local area is susceptible to typhoon in summer. Loading conditions such as overload truck and typhoon can be considered in future research.

REFERENCE LIST

C. C. Chang, T. Y. P. Chang, and Q. W. Zhang (2001). "Ambient vibration of long-span cable-stayed bridge," Journal of Bridge Engineering, 6(1): 46-53.

Celebi, M. (2006). "Real-time seismic monitoring of the new Cape Girardeau Bridge and preliminary analyses of recorded data: an overview," *Earthquake Spectra*, 22(3): 609-630.

China Ministry of Construction. (2001) "Code for seismic design of buildings," GB 50011-2001, P.R. China National Standard (in Chinese) Earthquake Level (for regions with seismic intensity level VII)

China Ministry of Construction. (2002) "Code for design of concrete structures," Chinese Standard GB 50010-2002, P.R. China.

Ernst, H.J. (1965). "Der E-Modul von Seilen unter Berucksichtigung des Durchhanges," Der Bauingenieur, 40(2) (in German).

Geophysics Research Institute of China Earthquake Administration, Ningbo Municipal Earthquake Office. (1996). "Seismic Safety Assessment Report on Ningbo ABS Site," Report # 96D0018, October 1996.

H. Tabatabai. (2005) "Inspection and Maintenance of Bridge Stay Cable Systems," NCHRP Synthesis 353, Transportation Research Board, Washington D.C, USA

K.L. Bathe. (1982). *Finite element procedures in engineering analysis*, Prentice-Hall, Inc., New Jersey, USA 1982

Institute of Bridge Science Research of China Railway Ministry, Administration Office for Ningbo Zhao-Bao-Shan Bridge, China, (2002). *Maintenance and Management Manual for Ningbo Zhao-Bao-Shan Grand Bridge*, Ningbo, China.

M.S. Troitsky. (1988) *Cable-stayed Bridges: theory and design* (Second Edition), Concordia University, Montreal, Canada 1988.

Computers and Structures, Inc (CSI) (2005). User's manual for SAP2000 version 10.0.1, Berkeley, California, USA.

Zhejiang Provincial Engineering Seismology Research Institute (2005). *Seismic Safety Assessment of Shuanshan Port Facility Site at Zhenhai Refinery*, Hangzhou, China.

S. J. Dyke, J. M. Caicedo, G. Turan, L. A. Bergman, and S. Hague (2003). "Phase I benchmark control problem for seismic response of cable-stayed bridges," Journal of Structural Engineering, 129(7): 857-872.

Sommerville, P., et al. (1997). "Development of ground motion time histories for Phase 2 of the FEAM/SAC steel project," SAC Background document SAC/BD-91/04, SAC joint venture, Sacramento, California, USA.

Wesolowsky, M.J. and Wilson, J.C. (2003). "Seismic isolation of cable-stayed bridges for near-field ground motions," Earthquake Engineering and Structural Dynamics, 32: 2107–2126.

Wilson, J.C., W. Gravelle, "Modeling of a cable-stayed bridge for dynamic analysis," Earthquake Engineering and Structural Dynamics, 20: 707-721.

Woodward-Clyde Consultants, (1994). Geotechnical Seismic Evaluation: Proposed New Mississippi River Bridge (A-5076) Cape Girardeau, MO, USA, Woodward-Clyde Consultants Report 93C8036-500.

VITA

Boer Li was born in Shanghai, China on January 6th, 1982. She is the only daughter of Hong Shao and Dr. Yongsheng Li. She graduated in Jun, 2004 with a B.S. Degree of Civil Engineering from Shanghai Jiao Tong University, Shanghai, China. In 2005, she was honored with a research assistantship from Lehigh University, Bethlehem, PA and from then on she continues her study in the States.

END OF TITLE